DISCLAIMER

This report was prepared as an account of work sponsored by an agency of the United States Government. Neither the United States Government nor any agency thereof, nor any of their employees, makes any warranty, express or implied, or assumes any legal liability or responsibility for the accuracy, completeness, or usefulness of any information, apparatus, product, or process disclosed, or represents that its use would not infringe privately owned rights. Reference herein to any specific commercial product, process, or service by trade name, trademark, manufacturer, or otherwise does not necessarily constitute or imply its endorsement, recommendation, or favoring by the United States Government or any agency thereof. The views and opinions of authors expressed herein do not necessarily state or reflect those of the United States Government or any agency thereof. Reference herein to any social initiative (including but not limited to Diversity, Equity, and Inclusion (DEI); Community Benefits Plans (CBP); Justice 40; etc.) is made by the Author independent of any current requirement by the United States Government and does not constitute or imply endorsement, recommendation, or support by the United States Government or any agency thereof.

SRMC-CWDA-2024-00052
Revision 0

Conceptual Model Testing Related to SDU 6 Drainwell Observations

February 2025

Prepared by: Savannah River Mission Completion LLC
Closure and Waste Disposal Authority
Aiken, SC 29808

Prepared for U.S. Department of Energy Under Contract No. 89303322DEM000068

Approvals

Author:

GREGORY FLACH (Affiliate) Digitally signed by GREGORY FLACH (Affiliate)
Date: 2025.02.24 12:04:25 -05'00'

Gregory P. Flach
Closure & Disposal Assessment
Savannah River Mission Completion LLC

Date

Technical Review per S4-ENG.51:

RICHARD HENRY (Affiliate) Digitally signed by RICHARD HENRY (Affiliate)
Date: 2025.02.24 12:56:18 -05'00'

Richard L. Henry, PhD
Closure & Disposal Assessment
Savannah River Mission Completion LLC

Date

Management Review:

Date: 2025.02.25 11:00:39 -05'00'

Aaron V. Staub
Closure & Disposal Assessment, Manager
Savannah River Mission Completion LLC

Date

Revision History

Rev.	Issued	Summary of Changes
0	February 2025	Initial issue.

Table of Contents

List of Figures

List of Tables

Acronyms/Abbreviations

C-S-H	Calcium-Silicate-Hydrate
DLM	Dynamic Leaching Method
DW	Drain Well
GWB	The Geochemist's Workbench®
MCC	Moisture Characteristic Curve
PA	Performance Assessment
PUREX	Plutonium Uranium Reduction EXtraction
REV	Representative Elementary Volume
SDF	Saltstone Disposal Facility
SDU	Saltstone Disposal Unit
SPF	Saltstone Production Facility
SREL	Savannah River Ecology Laboratory
SRNL	Savannah River National Laboratory
SRR	Savannah River Remediation LLC
SRS	Savannah River Site
SWPF	Salt Waste Processing Facility
vGM	van Genuchten-Mualem
w/cm	Water to cementitious materials ratio
WRC	Water Retention Curve
WSRC	Washington Savannah River Company

1.0 Introduction

From its inception in the early 1950s through the end of the Cold War in the early 1990s, the Savannah River Site (SRS) produced nuclear materials for national defense in five reactors. Additionally, irradiated reactor fuel and target tubes were dissolved in nitric acid to recover plutonium and uranium using the PUREX (Plutonium Uranium Reduction EXtraction) process. Liquid waste from these chemical separations processes was then stored onsite in 51 underground tanks. Eight waste storage tanks have been operationally closed (i.e. cleaned and grouted) and the remaining tanks hold a mixture of liquids, insoluble solids, and precipitated salts (SRMC-LWP-2022-00001), the latter generated by evaporating water from the liquid waste. Waste is currently being retrieved from tanks and separated into 1) high-radioactivity, low-volume, and 2) low-radioactivity, high-volume components, principally through the Salt Waste Processing Facility (SWPF) (SRMC-LWP-2023-00001). The former waste stream is vitrified in the Defense Waste Processing Facility (DWPF), stored onsite, and destined for offsite disposal in a deep geologic repository. The latter stream is mixed with dry cementitious materials in the Saltstone Production Facility (SPF) and the wet slurry placed in onsite Saltstone Disposal Units (SDUs) within the Saltstone Disposal Facility (SDF), where it hardens into a cement waste form termed *saltstone*. A low-infiltration surface cover system will be placed over the SDF at closure, where SDUs will then be in the subsurface post-closure (SRR-CWDA-2019-00001).

The saltstone dry feed composition may be 45% slag cement / 45% fly ash / 10% portland cement, or more recently 60% slag cement / 40% fly ash (SRR-CWDA-2019-00003, SRMC-STI-2022-00601). The water to cementitious materials mass ratio (w/cm) is approximately 0.6 (SRR-CWDA-2020-00040, SRR-CWDA-2020-00066, SRR-CWDA-2019-00003). Once cured, the saltstone pore solution has a pH around 12.4 and an ionic strength around 5.1 moles per liter (mol/L) with sodium nitrate being the dominant dissolved salt (SRR-CWDA-2018-00004 Table 3, pH calculated). The SDF Performance Assessment (PA, SRR-CWDA-2019-00001) compliance modeling case assumes a saturated hydraulic conductivity of 5.0E-10 centimeters per second (cm/s) for saltstone (SRR-CWDA-2018-00004), consistent with a cementitious material and laboratory measurements. Similarly, SDF PA compliance case modeling assumes a high air-entry pressure for saltstone, around 4.0E+4 centimeters (cm), which is characteristic of a cementitious material and reflects experimental data. Air-entry pressure is the gas pressure required to overcome liquid capillary suction and displace water with air. Barring significant degradation, saltstone is predicted to be fully saturated at equilibrium due to high total suction, composed of capillary and osmotic suctions (SRNL-STI-2018-00077). Capillary and osmotic suction refer to water attraction to solid surfaces and dissolved salts, respectively. Total suction is the difference between gas and liquid phase pressures in a porous medium.

The SDF comprises 15 existing and planned SDUs, in chronological order labeled SDU 1, 4, 2A, 2B, 3A, 3B, 5A, 5B, and 6 through 12 (SRR-CWDA-2019-00001, Figures 3.1-4 and 3.2-1). The focus of this study is SDU 6, a 375-ft diameter by 43-ft high disposal unit with a disposal capacity up to 35 million gallons (Figure 1-1). Unlike the other SDUs, SDU 6 has a 1.5% radial floor slope (Figure 1-2). Free liquid is routinely generated during saltstone disposal due to pre- and post-placement flushing of SPF equipment (mixer, hoppers, and transfer lines between SPF and SDF), and bleed from uncured grout (SRMC-CWDA-2024-00045). Such water is periodically drained from SDU 6 and returned to SPF for subsequent grout processing (SRR-CWDA-2023-00032).

Free liquid present after initial grout curing is thus termed *drainwater*. Grout placement to date has occurred through a center port in SDU 6. Although saltstone is a self-consolidating and self-leveling cementitious material by design, the 187.5-ft travel distance to the outer wall naturally leads to slight radial mounding. Azimuthal variability in grout height is also observed due to preferential finger-like lobe deposition.

Drainwater removal via flow through grout to drainwells was not considered feasible given the practical impermeability of saltstone (K_{sat} = 5.E-10 cm/s) with respect to operational timescales of hours to days. Thus, SDU 6 designers included eight 30-in diameter fully-penetrating drainwells distributed across the disposal unit footprint (Figure 1-3), so that drainwater above the grout surface could be pumped from the system wherever present. Pumping from multiple wells was presumed necessary to handle non-uniform variations in the grout surface over time. Considering that saltstone is predicted to be 100% saturated, or at least moving toward that equilibrium state, drainwell pumping was intended to remove only standing liquid above the top of the grout and/or within drainwells.

Unexpectedly, facility operators have been able to remove drainwater from SDU 6 by pumping solely from Drainwell 1. Furthermore, the water level in Drainwell 1 was observed to rebound within a couple hours, allowing the well to be drawn down multiple times during a day shift. And, water levels in all wells equilibrated to the same elevation within a couple days. Strong correlation between drainwell water levels was observed even when the nominal water level was clearly below the grout surface everywhere, precluding hydraulic communication between wells via drainwater flow across the grout surface. Moreover, after the equilibrium water level fell below the top of the grout, the volume of drainwater removed exceeded that estimated within the eight well bores for the observed drawdown, implying liquid was extracted from saltstone.

For example, Figure 1-4 illustrates SDU 6 drainwell behavior during December 2022, a period when no grout pours occurred to complicate data interpretation. To account for a 1.5% radial floor slope and variations in sump design between the inner and outer drainwells, all water levels in Figure 1-4 are referenced to the elevation of the outer well sumps, such that any elevation differences reflect hydraulic disequilibrium. The grout level during this period was approximately 10.5 ft (SRMC-CWDA-2024-00045 Section 9.3). Figure 1-4 illustrates recovery of Drainwell 1 within hours, hydraulic equilibration of all drainwell water levels within a day or so, and greater correlation for drainwells in closer proximity to Drainwell 1. The latter refers to drainwells at moderate distance from Drainwell 1 exhibiting muted drawdown and recovery transients, whereas water levels in more distant drainwells decrease more smoothly.

The unexpected SDU 6 field observations when water levels are below the grout level raise the following questions:

- What causes Drainwell 1 to recover within a few hours?
- What causes hydraulic equilibrium between all drainwells within a few days?
- When the liquid level is below the top of the grout, what is the source of drainwater in excess of free-standing water within well bores?

SRMC-CWDA-2024-00045 considers several mechanisms that could increase hydraulic connectivity between drainwells, with the most credible deemed:

- Flow through a higher conductivity grout sublayer adjoining the SDU 6 floor
- Flow along a gap between the grout and the SDU 6 floor liner
- Flow along cold joints between grout pours.

SRMC-CWDA-2024-00045 concludes “it is impossible to definitively assert the validity of one mechanism over another” without further analysis and data collection.

Motivated by SRMC-CWDA-2024-00045, this study compares SDU 6 drainwell data to multiple conceptual models using analytic methods, spreadsheet analysis, and numerical modeling. SRMC-CWDA-2024-00045 provides detailed information on relevant SDU 6 design features and the various drainwell observations in question and is recommended reading as this report assumes familiarity with its content. The conceptual model testing discussion herein also assumes familiarity with numerous porous-media concepts, properties, thermodynamic states, and behaviors. These subjects are reviewed in Section 2.0 for the benefit of readers who are not intimately familiar with these subjects, and to clearly define the concepts, terms, and symbols used in the later discussion. Section 3.0 summarizes the material properties of saltstone as currently understood from laboratory testing. Section 4.0 presents SDU 6 data for the two periods adopted for conceptual model testing, December 6-25, 2022 and November 15, 2022 to April 15, 2023. Section 5.0 defines the conceptual model of the 2020 SDF PA and compares it to SDU 6 drainwell observations. Section 6.0 investigates several alternative conceptual models. Section 7.0 summarizes conclusions drawn on the likelihood of the various conceptual models.

Figure 1-1: Exterior and interior photographs of SDU 6.

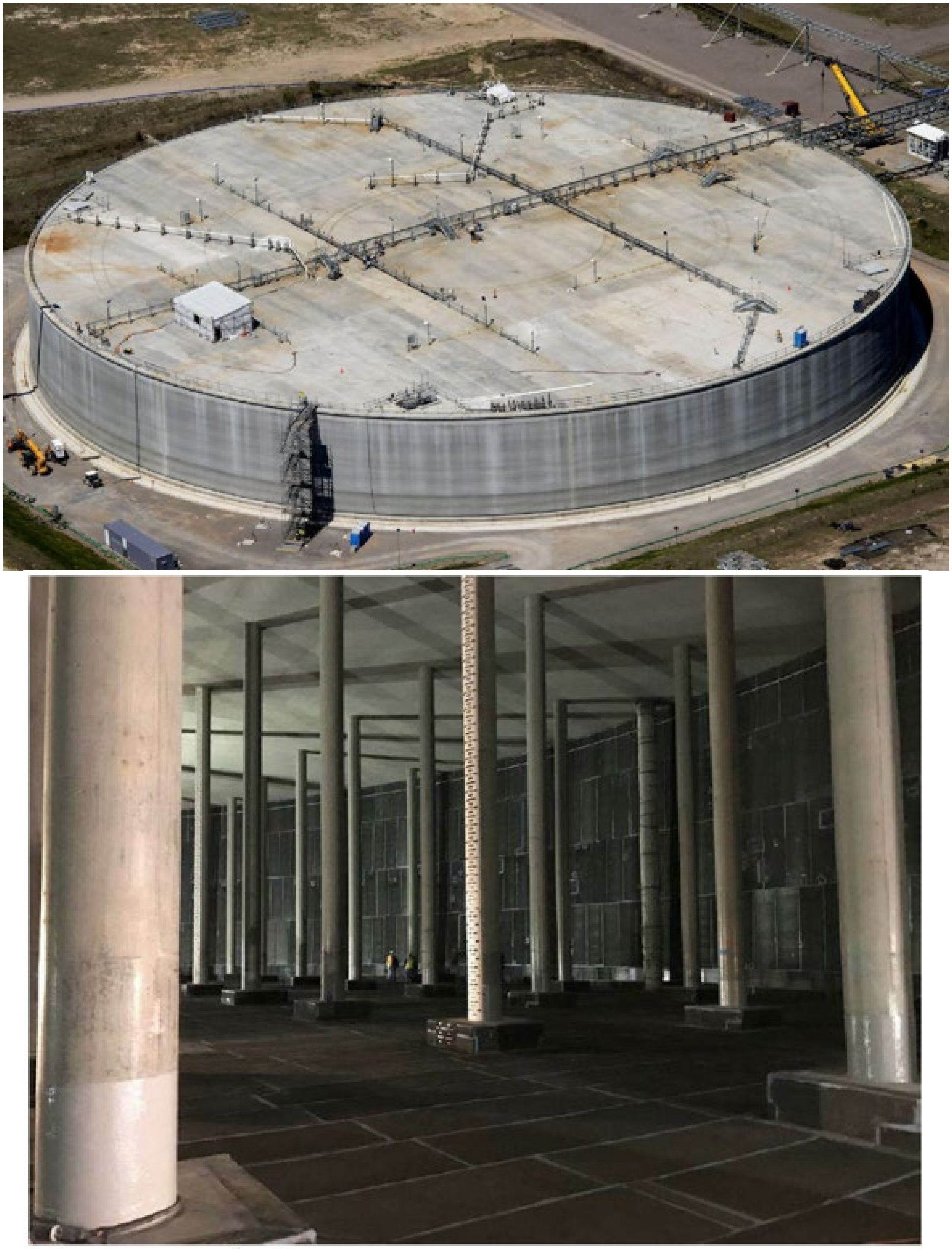

Figure 1-2: Conceptual design of SDU 6 post-closure.

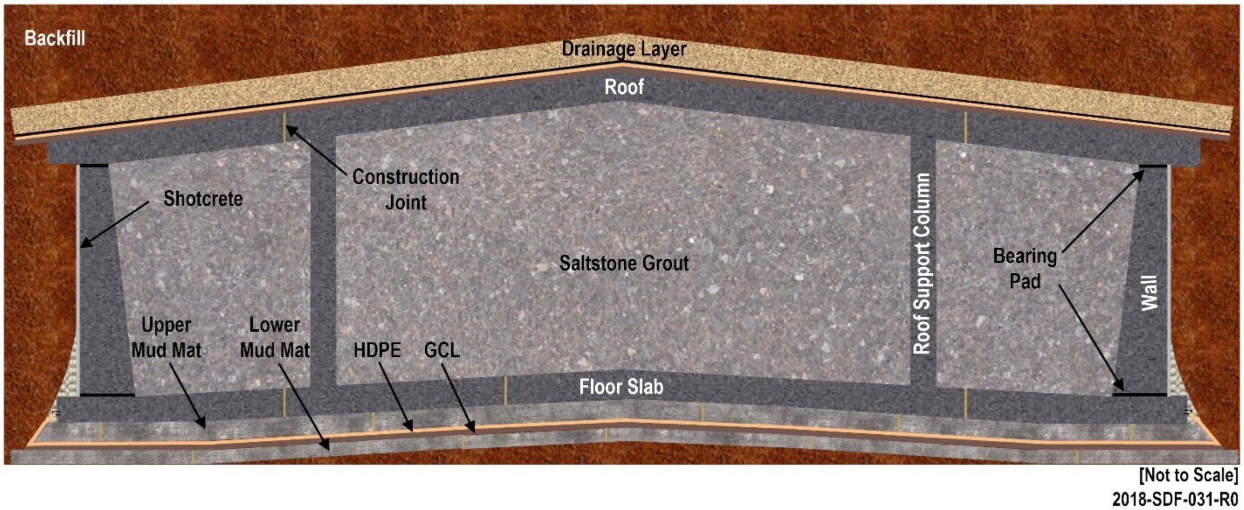

[Source: SRR-CWDA-2019-00001]

Figure 1-3: Approximate drainwell locations in SDU 6.

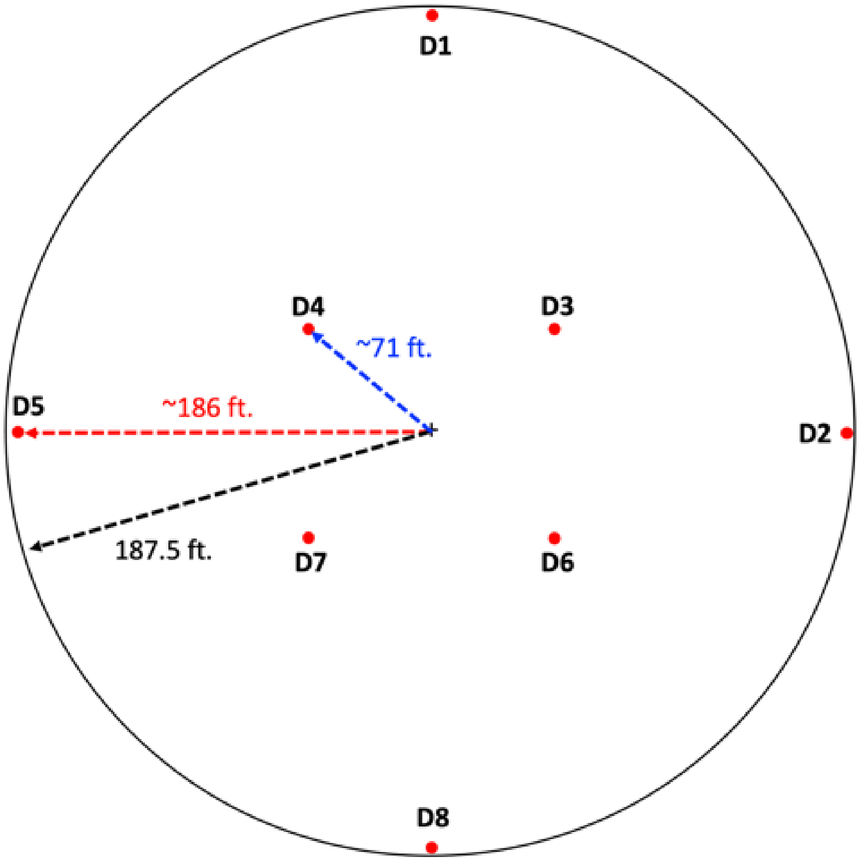

[Source: SRMC-CWDA-2024-00045]

Figure 1-4: SDU 6 drainwell drawdowns, December 6-25, 2022.

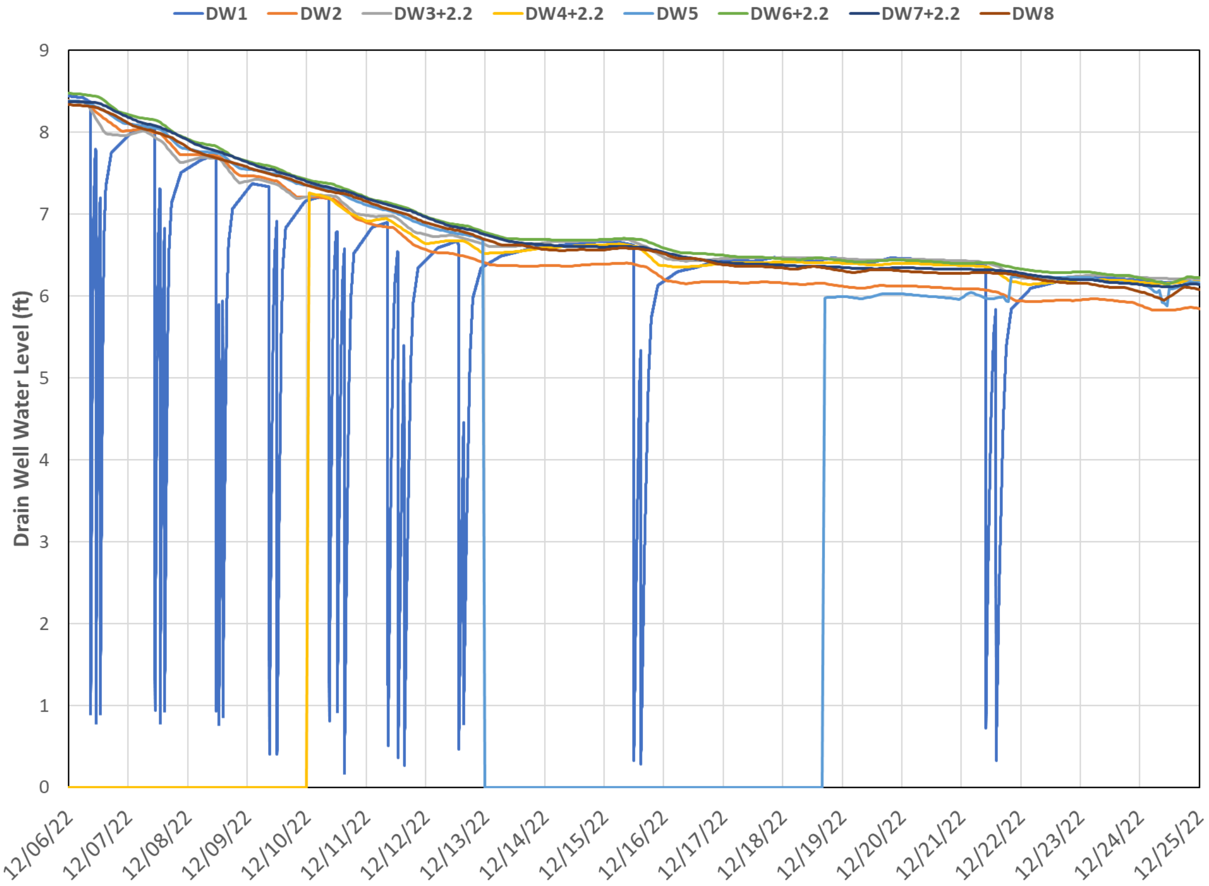

Note to figure: All water levels referenced to the sump elevation for outer drainwells (Drainwells 1, 2, 5, 8) by adding 2.2 ft to inner drainwell water levels referenced to their sumps (Drainwells 3, 4, 6, and 7).

2.0 Porous-Medium Properties, States, and Behaviors

This section reviews the porous-medium concepts, material properties, thermodynamic states, and behaviors relevant to the conceptual model evaluations in Section 6.0, and clarifies the terms and symbols used therein. Recommended general references include de Marsily (1986), Freeze and Cherry (1979), and the online resources of *The Groundwater Project* (https://gw-project.org/). de Marsily (1986) and Freeze and Cherry (1979) are available free of cost from *The Groundwater Project* website under *Preserved Books*.

In the context of the current study, a *porous medium* is a material composed of a solid matrix with interstitial void space, termed *pores*, and filled with fluid (liquid and/or gas). While strictly speaking a point within a porous medium is occupied solely by either a solid or fluid phase, typical engineering practice is to consider a spatial resolution that is coarser than the *representative elementary volume* (REV), defined to be the smallest volume over which a measurement can be made that will yield a value representative of the whole. Then a porous medium can be viewed as a material with composite or blended properties. Said another way, the porous materials encountered in this study will be analyzed at spatial scales significantly larger than pore scale.

2.1 Volumetric properties and states

Within the REV construct, *porosity* (n) is defined as the ratio of void volume (V_v) to total volume (V)

$$n \equiv \frac{V_v}{V} \tag{1}$$

with units [L^3 void / L^3] or [-] (unitless) depending on analyst preference. At the pore scale, porosity can be viewed as the statistical probability of encountering void space. *Water saturation* (S) is defined as the ratio of water (including dissolved solids) volume (V_w) to void volume

$$S \equiv \frac{V_w}{V_v} \tag{2}$$

a state variable with units [L^3 water / L^3 void] or [-] (unitless) depending on preference. *Water content* (θ) is defined as water volume divided by total volume

$$\theta \equiv \frac{V_w}{V} \tag{3}$$

with units [L^3 water / L^3] or [-] (unitless). With these definitions

$$\theta = Sn \tag{4}$$

and knowledge of any two parameters among porosity, water saturation, and water content implies knowledge of the remaining parameter.

2.2 Flow properties and rates

Flow through a porous medium is commonly characterized by *Darcy velocity* (U), defined as volumetric flowrate (Q) divided by total cross-sectional area of the medium (A; not just the area occupied by fluid)

$$U \equiv \frac{Q}{A} \tag{5}$$

with units [L/T]. Alternatively, *pore velocity* (v) [L/T] may be defined as volumetric flowrate divided by the area occupied by water (A_w)

$$v \equiv \frac{Q}{A_w} \tag{6}$$

Assuming $A_w/A = V_w/V$, pore velocity is related to Darcy velocity through the expression

$$v = \left(\frac{Q}{A}\right)\left(\frac{A}{A_w}\right) = U\left(\frac{V}{V_w}\right) = \frac{U}{\theta} = \frac{U}{Sn} \tag{7}$$

Pore velocity is the speed at which a fluid particle travels through the pores of the medium, whereas Darcy velocity is volumetric flux through a REV of the medium. In three-dimensions the (x, y, z) components of Darcy and pore velocity are usually denoted (U, V, W) and (u, v, w), respectively, where V in this context is not to be confused with volume.

The usual driving forces for porous medium flow are gravity and pressure gradient. For water with constant properties, gravity and pressure gradient are commonly combined into a hydraulic head gradient, where the state variable *hydraulic head* (h) [L] is defined as

$$h \equiv \frac{P}{\rho g} + z \tag{8}$$

Here P [M/LT^2] may be either the absolute or gage pressure (because only the gradient of pressure drives flow), ρg = specific weight of water [M/L^{2}T^2], and z = elevation [L]. $P/\rho g$ is referred to as *pressure head*, p [L], such that

$$h \equiv p + z \tag{9}$$

Above the water table pressure head may be negative due to capillary and osmotic forces, in which case a positive-valued *suction head* or *tension head,* ψ, can be defined as $-p$ for convenience. By definition, pressure at the *water table* is zero.

Darcy's law relates porous medium flow to hydraulic head gradient (dh/dx) [-]. For water with constant properties, Darcy's law under saturated conditions takes the one-dimensional form

$$U = -K_{sat}\frac{dh}{dx} \tag{10}$$

where K_{sat} is *saturated hydraulic conductivity* [L/T]. In this context K_{sat} is a scalar whereas in three-dimensions K_{sat} becomes a tensor. K_{sat} is defined by a mixture of material and fluid properties as

$$K_{sat} \equiv \frac{\kappa \rho g}{\mu} \tag{11}$$

where κ = intrinsic permeability [L^2], ρ = fluid density [M/L^3], g = gravitational acceleration [L/T^2], and μ = viscosity [M/LT]. Equations (10) and (11) thus define *intrinsic permeability*, a material property.

For variably-saturated conditions, Darcy's law is written more generally as

$$U = -k_r(S) K_{sat} \frac{dh}{dx} \tag{12}$$

where k_r is *relative permeability* [-], a function of saturation or alternatively water content (θ). Consistent with Equation (10), k_r = 1 when S = 1. Relative permeability monotonically decreases with decreasing saturation starting from a saturated condition. Unsaturated hydraulic conductivity is defined by

$$K(S) \equiv k_r(S) K_{sat} \tag{13}$$

In multiple dimensions, K is a tensor and dh/dx is replaced by ∇h in Darcy's law.

2.3 Total, capillary, and osmotic suction heads

As noted in the previous section, the thermodynamic state of an unsaturated porous medium is conveniently defined in terms of a positive-valued suction (tension) head. Per Richards (1965) as cited by Fredlund and Rahardjo (1993), *total suction head* (ψ) for an isothermal material comprises two components, *capillary* or *matric suction* (ψ_c) and *osmotic suction* (π)

$$\psi = \psi_c + \pi \tag{14}$$

See also Dao et al. (2008). Capillary suction is caused by surface tension between a wetting solid and interstitial water within a fine-scale pore structure. Osmotic suction is caused by dissolved solids in pore water, such as salts in the case of saltstone. Thus, hydraulic head can be divided into capillary, osmotic, and gravitational driving forces

$$h = -\psi + z = -\psi_c - \pi + z \tag{15}$$

Again, the gradient of hydraulic head drives flow per Darcy's law, Equation (10) and (12).

2.4 Capillary suction and saturation

Saturation and capillary suction head are related through an empirical relationship termed the *water retention curve* (WRC), commonly defined using the van Genuchten (1980) functional form

$$S_e \equiv \frac{\theta - \theta_r}{\theta_s - \theta_r} = \frac{S - S_r}{1 - S_r} = \left[\frac{1}{1 + (\alpha\psi_c)^n}\right]^m \tag{16}$$

where S_e = effective saturation [-], θ_s = saturated water content, θ_r = residual water content, S_r = residual saturation, ψ_c = capillary suction head [L], α = a scaling parameter [L^{-1}], and n = a shape parameter [-] (not to be confused with porosity in this context). For the Mualem (1976) formulation

$$m \equiv 1 - \frac{1}{n} \tag{17}$$

and Equations (16) and (17) are termed the *van Genuchten-Mualem* (vGM) model. Water retention curves exhibit hysteresis, a mismatch between the WRCs for a medium undergoing drying versus wetting. This indicates that the amounts of water present in the medium during desorption is not the same as the amount of water adsorbed during wetting at the same applied pressure (suction). This study concerns decreasing saturation associated with SDU 6 drainage so the *drying* curve is the WRC of interest. The empirical data-fitting parameters are θ_s and θ_r (for water content calculation) or S_r (for saturation calculation), α, and n. In principal θ_s should be identical to porosity but is often treated as a purely empirical parameter and allowed to deviate.

As an illustrative example for further discussion, Table 2-1 provides vGM parameters and other physical properties for SRS sandy sediment (<25% Mud), abbreviated *Sand* going forward (SRNL-STI-2019-00355 Table 5-20).

Table 2-1: Hydraulic properties of SRS sandy sediment (Sand).

Hydraulic Parameter	Sand
Horizontal hydraulic conductivity, K_h (cm/s)	5.0E-04
Vertical hydraulic conductivity, K_v (cm/s)	2.8E-04
Total porosity, n	0.383
van Genuchten-Mualem parameters:	
θ_s	0.383
θ_r	0.082137
$S_r = \theta_r/\theta_s$	0.2145
α (1/cm)	0.199006
n	1.241769
$m = 1 - 1/n$	0.194697

Figure 2-1 plots the water retention curve for the Sand material using both logarithmic and linear scales for suction head.

The capillary suction head at which desaturation effectively begins is termed the *air-entry pressure head*, ψ_a. Below the air-entry pressure the porous medium is 100% saturated, even though the pressure head is negative. Above the air-entry pressure, air has entered the pore space and displaced water. As a practical working definition, air-entry pressure is often defined as the *inverse* of the vGM α parameter. Based on Figure 2-1(a), the air-entry pressure for Sand could be defined as ψ_a = 0.5 cm. Alternatively, the inverse of the vGM n parameter from Table 2-1 yields ψ_a = 5 cm. Saturation asymptotically approaches the vGM residual saturation parameter (S_r) as suction head increases. The vGM n parameter controls the rate at which saturation approaches S_r after the air-entry pressure has been exceeded. Specifically, increasing vGM n hastens the approach to residual saturation.

Gravity equilibrium refers to the static condition of no flow within a porous medium. From Darcy's law, this condition occurs when the hydraulic head gradient is zero, which implies constant h. Ignoring potential osmotic effects for now, Equation (15) then reduces to

$$\psi_c = z \tag{18}$$

where the upward z coordinate is referenced to the water table, defined as the elevation where ψ_c = 0). Thus, saturation under gravity equilibrium conditions is defined by replacing ψ_c with z (height above the water table) in Equation (16). In this context, Figure 2-1 also defines the saturation profile of a porous material at gravity equilibrium where suction head is the distance above the water table. Equation (18) can alternatively be written

$$p = -z \tag{19}$$

which means pressure head varies linearly with elevation both below *and above the water table* under gravity equilibrium (hydrostatic) conditions. Below the water table z is negative and thus p is positive; above the water z is positive and thus p is negative.

The gravity equilibrium concept is useful toward understanding how a porous medium will desaturate when exposed to a decreasing water table between initial and final hydrostatic conditions. Equation (19) implies the shape of the hydrostatic saturation profile is invariant in reference to the water table. The new equilibrium profile is defined by aligning the water retention curve ψ_c = 0 point with the new water level. This concept is illustrated in Figure 2-2 for a 100 cm thickness of Sand (Table 2-1). Saturation profiles are shown for water levels of 10, 50, and 90 cm measured from the bottom of the material. The equilibrium saturation profiles for the 10- and 90-cm water tables are 40 cm translations of the 50-cm profile downward and upward, respectively.

The volume of water drained or imbibed between water levels is the area between the corresponding saturation curves times total porosity. Starting from a fully saturated condition, no water is effectively drained until drawdown exceeds the air-entry pressure. At deeper water levels, the drain rate asymptotically approaches

$$\frac{dV}{dh} = \theta_s - \theta_r = n(1 - S_r) \tag{20}$$

In between these end members, integration of the difference between vGM water retention curves is required.

Figure 2-1: Water retention curve for SRS sandy sediment (Sand): (a) logarithmic, and (b) linear scale.

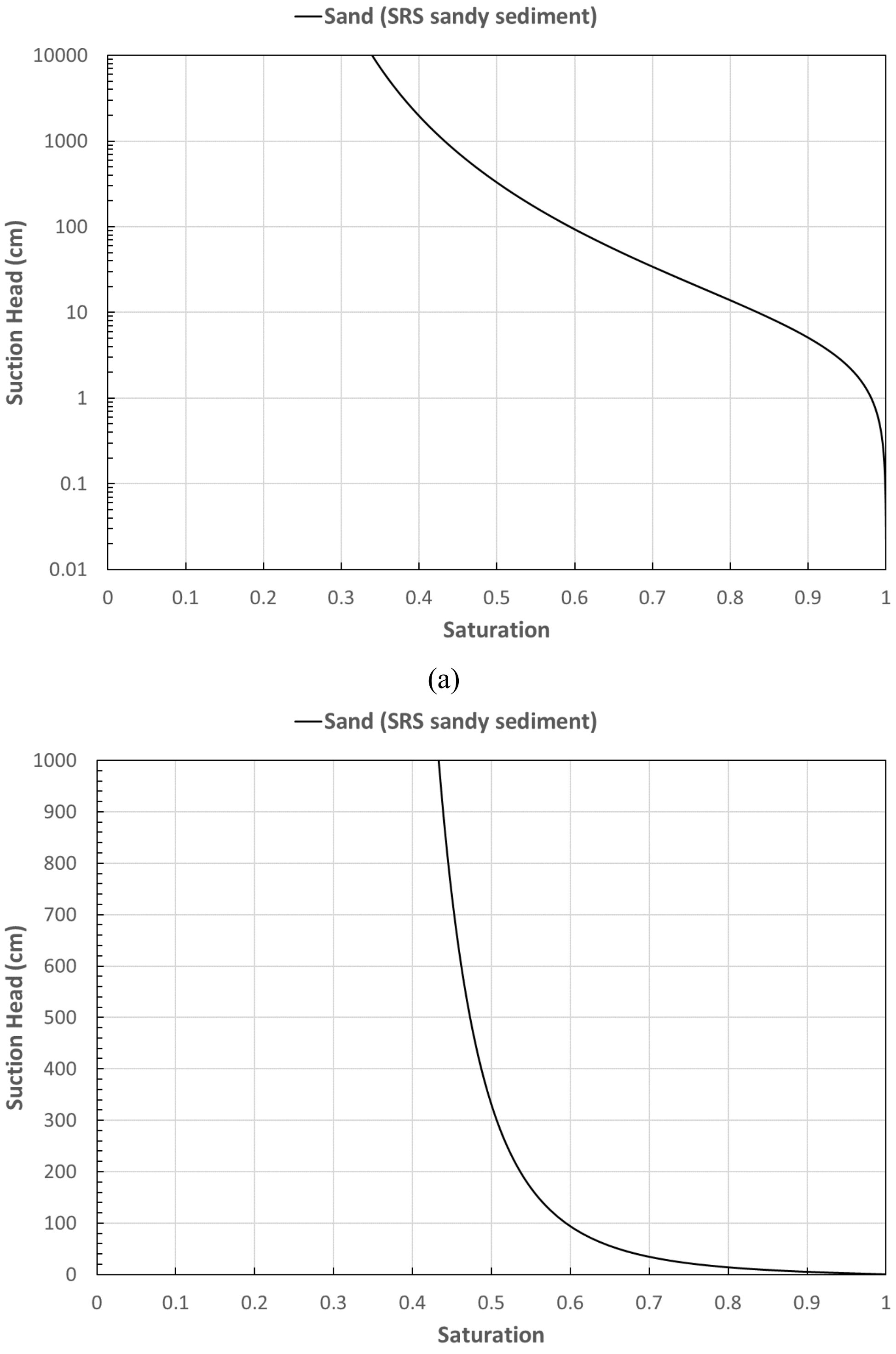

(a)

(b)

Figure 2-2: Gravity equilibrium saturation profiles or SRS sandy sediment (Sand) for various water table elevations.

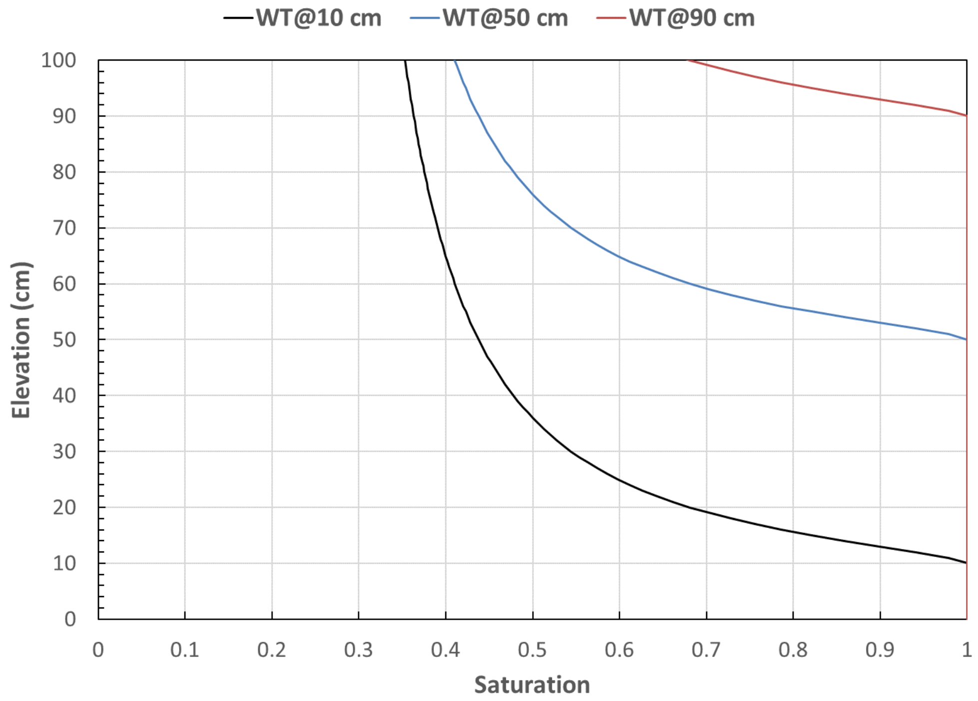

2.5 Osmotic suction and solute concentration

Osmotic effects are commonly ignored in porous-media analysis on the basis that solute concentrations are low, such that osmotic suction is small compared to matric suction, and/or solute concentrations and osmotic suctions are relatively constant, such that osmotic gradients are small. In either case, osmotic suction then has a minor effect on flow compared to matric suction and/or gravity. However, the high concentration of dissolved salts in saltstone grout makes osmotic suction an important consideration.

Osmotic suction (π, [L]) can be related to solute concentration using the Morse equation given by

$$\rho g \pi = iMRT \tag{21}$$

where ρg = specific weight of water [M/L^{2}T^2], i = van’t Hoff factor [-], M = molarity of the solution [N/L^3], R = universal (molar) gas constant [ML^2/NΘT^2], and T = absolute temperature [Θ]. Equation (21) assumes a dilute solution but can be used with increasing approximation for more concentrated solutions. The dimensionless *van’t Hoff factor* depends on solution chemistry and is less than or greater than 1.0 depending on whether solute particles associate or dissociate in solution, respectively. In this study solution molarity is defined using ion concentrations and the van’t Hoff factor assumed to be 1.0.

2.6 Total suction and relative humidity

A porous medium in thermodynamic equilibrium with a humid air space satisfies the Kelvin relationship

$$\psi = \psi_c + \pi = -\frac{RT}{gM_w} ln\left(\frac{P_v}{P_0}\right) = -\frac{RT}{gM_w} ln(RH) \tag{22}$$

where ψ = total suction head [L], ψ_c = capillary or matric suction head [L], π = osmotic suction head [L], g = gravitational acceleration [L/T^2], R = universal (molar) gas constant [ML^2/NΘT^2], T = absolute temperature [Θ], P_v = water vapor pressure [M/LT^2], P_0 = vapor pressure at saturation [M/LT^2], M_w = molar mass of water [M/N], and RH = relative humidity [-] (Richards 1965, cited in Fredlund and Rahardjo 1993).

Rearranging terms in Equation (22) and substituting the righthand side of Equation (21) for osmotic suction yields the following expression for capillary suction head, which controls porous-medium water saturation:

$$\psi_c = \frac{RT}{gM_w} ln\left(\frac{1}{RH}\right) - \frac{iMRT}{\rho g} \tag{23}$$

Saturation increases as capillary suction head decreases. Equation (23) indicates higher relative humidity (RH) and higher solute concentration (M) drive equilibrium saturation toward higher values, until 100% saturation is achieved.

2.7 Relative permeability and unsaturated hydraulic conductivity

Relative permeability, initially defined in Section 2.2, is related to saturation through an empirical *relative permeability curve*. The Mualem (1976) relative permeability function based on the van Genuchten (1980) saturation function is given by

$$k_r = \sqrt{S_e}\left[1 - \left(1 - S_e^{1/m}\right)^m\right]^2 \tag{24}$$

and adopted for this study. The water retention and relative permeability curves are collectively termed the *moisture characteristic curves* (MCCs) of a porous medium.

Figure 2-3 shows the relative permeability curve for SRS sandy sediment (Sand) based on the vGM parameters from Table 2-1. Unsaturated hydraulic conductivity can be directly related to capillary suction head by combining saturated hydraulic conductivity, the relative permeability curve, and the water retention curve as

$$K(\psi_c) = k_r[S(\psi_c)]K_{sat} \tag{25}$$

The result for SRS sandy sediment (Sand) is shown in Figure 2-4. K_{sat} controls hydraulic conductivity at suctions below the air-entry pressure. The vGM α parameter controls the air-entry pressure head (ψ_a), the suction head at which hydraulic conductivity begins to decrease from its saturated value. The vGM n parameter controls the downward slope of K beyond the air-entry pressure head.

Figure 2-3: Relative permeability curve for SRS sandy sediment (Sand).

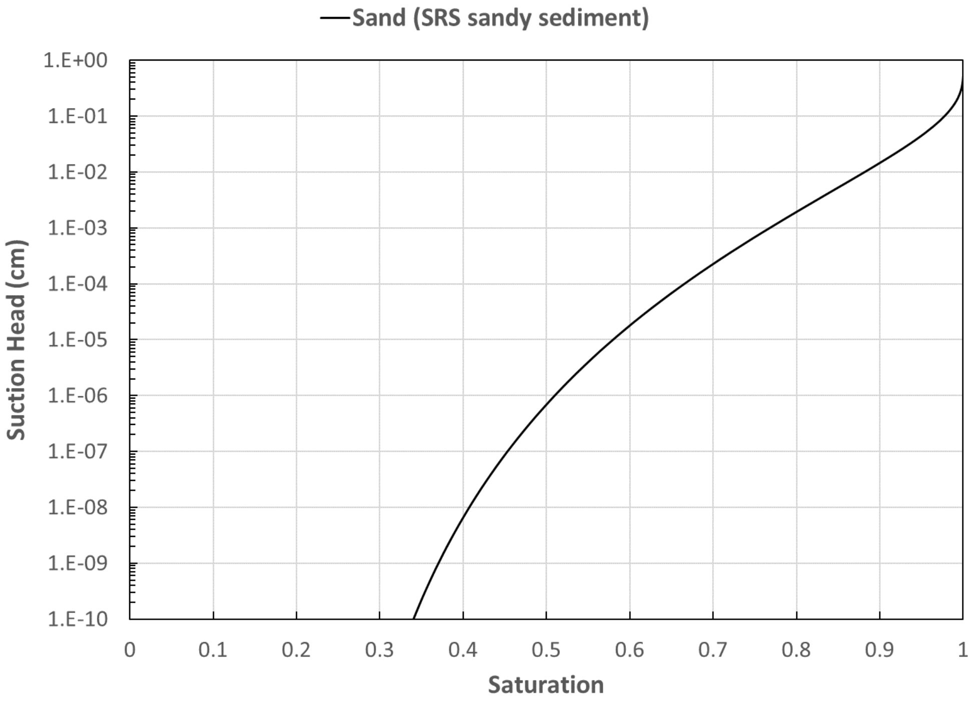

Figure 2-4: Unsaturated hydraulic conductivity for SRS sandy sediment (Sand).

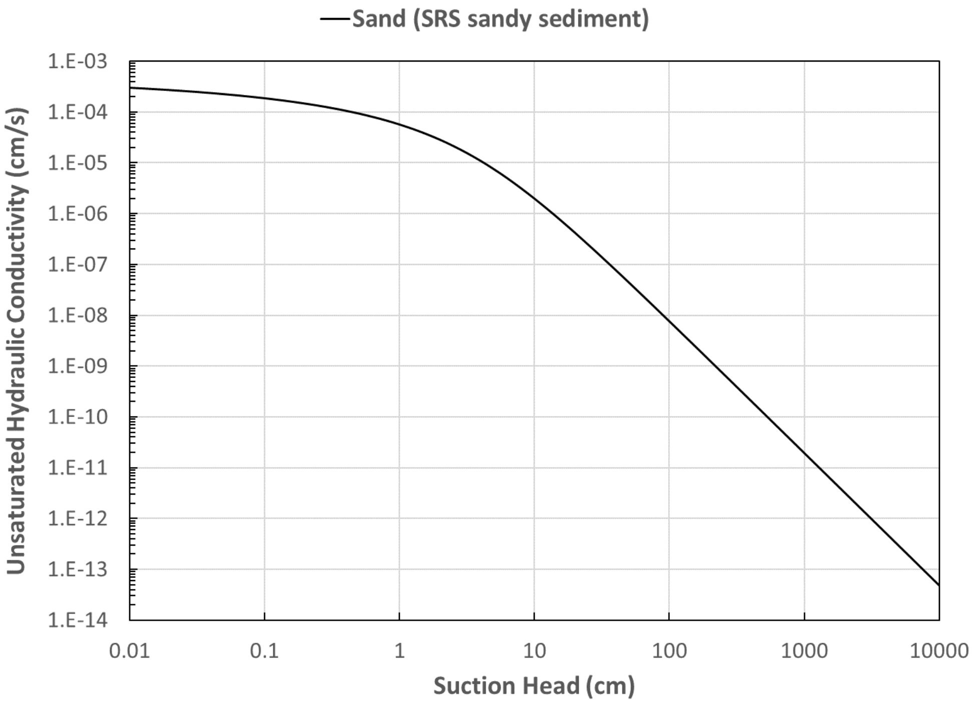

2.8 Leverett scaling

Leverett (1941) proposed that similar porous materials satisfy a dimensionless *J-function* defined by

$$J(S) = \frac{\rho g \psi_c(S)\sqrt{\kappa/n}}{\gamma cos\theta_c} \qquad (26)$$

where ρg = specific weight of water [M/L^{2}T^2] , ψ_c = capillary or matric suction head [L], S = saturation [-], γ = surface tension [M/T^2], $cos\theta_c$ = contact angle [-], κ = intrinsic permeability [L^2], and n = porosity.

Assuming constant fluid and wetting properties, any two materials within the J-function class satisfy the relationship

$$\psi_{c1}(S)\sqrt{\kappa_1/n_1} = \psi_{c2}(S)\sqrt{\kappa_2/n_2} \qquad (27)$$

at saturation S. If materials within the J-function class share a common residual saturation (S_r) and vGM n parameter, then at saturation S the following is also true

$$\left[\frac{1}{1+(\alpha_1\psi_{c1})^n}\right]^m = \left[\frac{1}{1+(\alpha_2\psi_{c2})^n}\right]^m \qquad (28)$$

per Equation (16). Equation (28) reduces to

$$\alpha_1\psi_{c1} = \alpha_2\psi_{c2} \qquad (29)$$

Combining Equations (27) and (29) yields

$$\frac{\alpha_1}{\sqrt{\kappa_1/n_1}} = \frac{\alpha_2}{\sqrt{\kappa_2/n_2}} \qquad (30)$$

Note that κ can be replaced with K because they are proportional quantities for constant fluid properties per Equation (11). Equation (30) can be used to estimate a change in air-entry pressure (inverse of α) corresponding to a change in hydraulic conductivity for related materials. For example, if porosity is fixed then

$$\alpha_1\sqrt{K_2} = \alpha_2\sqrt{K_1} \qquad (31)$$

While an approximation, Equation (31) has proven useful in practice because porosity, residual saturation, and the vGM n parameter are much less variable than the vGM α parameter and K_{sat}, which can vary orders of magnitude. For example, Guarracino (2007) shows that saturated hydraulic conductivity varies as the square of the vGM α parameter for a broad range of soils spanning 12 major textural groups, consistent with Equation (31). Similarly, SRMC-CWDA-2024-00049 Figure 5-4 shows that α varies approximately as $\sqrt{K_{sat}}$ for K_{sat} ranging between 1.0E-12 and 1.0E-02 cm/s, and SRMC-CWDA-2024-00049 Table 8-2 shows that dependence.

2.9 Matrix compressibility

The discussion to this point has implicitly assumed that the porous medium is incompressible, which is not strictly true. In geologic applications, compressibility is typically an important consideration for confined aquifers and unimportant in unconfined aquifers. Matrix compression will be shown important for analyzing saltstone behavior in SDU 6. Compression of a porous material reduces its porosity, which could increase saturation in unsaturated pores or expel water from fully saturated pores.

Consider a horizontal plane through a porous medium. The average *total stress* (σ, [M/LT^2]) at this elevation is the combined weight of solids and fluid above the plane per unit area. Assuming pressure is positive (the plane is below the water table) then some of the total stress is borne by the fluid phase and the remainder by the solid phase. The latter is termed *effective stress* ($\bar{\sigma}$, [M/LT^2]) because changes in this stress effectively cause compression of a porous matrix. A relationship between effective stress and pressure is needed to simulate matrix compressibility during a drawdown event.

The relationship between effective stress and fluid pressure depends on the structure of the solid phase matrix, and the water retention characteristics of the matrix above the water table. Figure 2-5 illustrates four stress configurations for a thickness L [L], two candidates for an initial condition and two for the final condition. The water table is at the top of the domain initially, and then drawn down a distance L for the final condition.

Submerged medium 1 (*Sub1*) is assumed to be granular with point-to-point contact between individual grains, such that the contact area is effectively zero. Submerged medium 2 (*Sub2*) is assumed to have high contact area, such that the contact area divided by total area is equal to $(1-n)$. The critical difference between these end-member configurations is that the *Sub1* solid experiences buoyancy while the *Sub2* solid does not. While *Sub1* and *Sub2* experience the same total stress at the bottom, the effective stress is lower in *Sub1* due to buoyancy (Table 2-2, top row).

The *Dry* and *Wet* configurations are end-members for the final condition. Although a granular structure is depicted in Figure 2-5, the stresses for these conditions are not dependent on the structure of the matrix (solid phase contact area). The *Dry* configuration assumes pores are completely drained above the water table. The *Wet* configuration assumes pores remain fully saturated due to sufficiently high capillary suction. The total and effective stresses within each condition are the same, and between conditions differ by the weight of water per unit area (Table 2-2, left column).

The body of Table 2-2 considers four drawdown scenarios, A-D. The pressure change [M/LT^2] is

$$\Delta P \equiv P_{final} - P_{initial} = 0 - \rho g L = -\rho g L \tag{32}$$

Changes in total and effective stress ($\Delta\sigma$, $\Delta\bar{\sigma}$) are summarized in the table. Also shown is the corresponding relationship between $\Delta\sigma$, $\Delta\bar{\sigma}$, and ΔP. The relationship

$$\Delta\sigma = \Delta\bar{\sigma} + \Delta P \tag{33}$$

is attributed to Terzaghi and

$$\Delta\sigma = \Delta\bar{\sigma} + n\Delta P \tag{34}$$

to Fillunger (Guerriero and Mazzoli 2021, Guerriero 2022). These expressions are a special case of

$$\Delta\sigma = \Delta\bar{\sigma} + (1 - a_c)\Delta P \tag{35}$$

by Skempton where a_c = contact area density ranging from 0 for *Sub1* to $(1 - n)$ for *Sub2* (Guerriero 2022). See also https://books.gw-project.org/land-subsidence-and-its-mitigation/chapter/effective-intergranular-stress-and-soil-parameters/ and https://books.gw-project.org/land-subsidence-and-its-mitigation/chapter/box-1-justification-of-terzaghis-principle/ from *The Groundwater Project*.

Across the four drawdown scenarios A-D shown in Figure 2-5, $\Delta\bar{\sigma}$ ranges from 0 to $-n\Delta P$ to $-(1 - n)\Delta P$ to $-\Delta P$. Scenario C is deemed most representative of the saltstone waste form for two reasons. First, the Terzaghi theory of consolidation has proven accurate for a wide range of materials and is widely accepted. Second, saltstone is expected to remain 100% saturated in SDU 6 due to strong capillary and/or osmotic forces, as discussed further in Section 3.2. With this selection, the differential relationship between effective stress and pressure becomes

$$d\bar{\sigma} = -dP \tag{36}$$

Fortunately, Equation (36) underlies the standard set of equations governing flow in a confined aquifer discussed in the next section. Thus, the latter is directly applicable to the current study without modification.

Figure 2-5: Effective stress conditions.

Candidate initial conditions		Candidate final conditions	
"Sub1" Submerged medium 1	"Sub2" Submerged medium 2	"Dry" 0% saturation	"Wet" 100% saturation
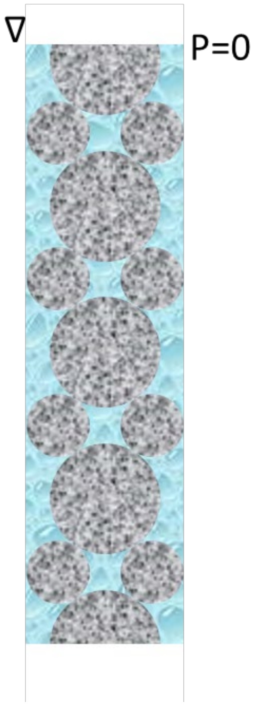			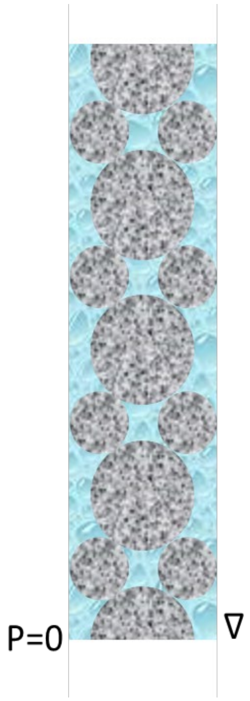

Table 2-2: Total, effective, and differential stresses.

Final Conditions	Initial Conditions	
	Sub1 $\sigma_{sub} = \rho_s gL(1-n) + \rho gLn$ $\overline{\sigma_{sub1}} = (\rho_s - \rho)gL(1-n)$	**Sub2** $\sigma_{sub} = \rho_s gL(1-n) + \rho gLn$ $\overline{\sigma_{sub2}} = \rho_s gL(1-n)$
Dry $\sigma_{dry} = \rho_s gL(1-n)$ $\overline{\sigma_{dry}} = \rho_s gL(1-n)$	**Scenario A** $\Delta\sigma = n\Delta P$ $\Delta\bar{\sigma} = -(1-n)\Delta P$ $\Delta\sigma = \Delta\bar{\sigma} + \Delta P$ (Terzaghi)	**Scenario B** $\Delta\sigma = n\Delta P$ $\Delta\bar{\sigma} = 0$ $\Delta\sigma = \Delta\bar{\sigma} + n\Delta P$ (Fillunger)
Wet $\sigma_{wet} = \rho_s gL(1-n) + \rho gLn$ $\overline{\sigma_{wet}} = \rho_s gL(1-n) + \rho gLn$	**Scenario C** $\Delta\sigma = 0$ $\Delta\bar{\sigma} = -\Delta P$ $\Delta\sigma = \Delta\bar{\sigma} + \Delta P$ (Terzaghi)	**Scenario D** $\Delta\sigma = 0$ $\Delta\bar{\sigma} = -n\Delta P$ $\Delta\sigma = \Delta\bar{\sigma} + n\Delta P$ (Fillunger)

2.10 Conservation equations governing flow

Darcy's law combined with conservation of mass yields a governing equation for variably saturated flow known as Richards equation. In the absence of internal sources or sinks, the form for one-dimensional vertical flow is

$$\frac{\partial Sn}{\partial t} = \frac{\partial}{\partial z}\left[k_r K_{sat} \frac{\partial h}{\partial z}\right] \tag{37}$$

and in three-dimensions

$$\frac{\partial Sn}{\partial t} = \nabla \cdot [k_r K_{sat} \nabla h] \tag{38}$$

where Sn may be replaced by θ (Freeze and Cherry 1979 Eq. 2.79). Saturation and relative permeability are implicitly functions of hydraulic head through the two moisture characteristic curves. Strong non-linearity in the MCCs makes the Richards equation difficult to solve with numerical methods.

Saturated flow in a compressible confined aquifer with no internal sources/sinks is governed by (Freeze and Cherry 1979 Eq. 2.74, de Marsily 1986 Eq. 5.3.9)

$$S_s \frac{\partial h}{\partial t} = \nabla \cdot [K_{sat} \nabla h] \tag{39}$$

where S_s is *specific storage coefficient* [1/L] discussed further in Section 2.12. When hydraulic properties are constant, Equation (39) may be written

$$\frac{\partial h}{\partial t} = D \nabla^2 h \tag{40}$$

where

$$D \equiv K_{sat}/S_s \tag{41}$$

is termed *hydraulic diffusion coefficient* or *hydraulic diffusivity* [L^2/T].

A hydraulic diffusion coefficient may also be defined for unsaturated flow by using the chain rule of differentiation to rewrite the accumulation term of Equations (37), (38) as

$$\frac{\partial \theta}{\partial t} = \frac{\partial \theta}{\partial h}\frac{\partial h}{\partial t} \equiv C \frac{\partial h}{\partial t} \tag{42}$$

where C is called *specific moisture capacity* by Freeze and Cherry (1979) or *drainage porosity* and *specific yield* by de Marsily (1986). The term *specific moisture capacity* is used in this study to avoid confusion with total porosity and alternative meanings of specific yield. Using Equation (42), Richards equation may be alternatively written

$$C\frac{\partial h}{\partial t} = \nabla \cdot [k_r K_{sat} \nabla h] \tag{43}$$

where specific moisture capacity is implicitly a function of pressure head. Let K_{ref} be a reference conductivity, representative of a particular medium and flow condition. Then Equation (43) may be written

$$\frac{\partial h}{\partial t} = \frac{K_{ref}}{C}\nabla \cdot \left[\frac{k_r K_{sat}}{K_{ref}}\nabla h\right] \equiv D\nabla \cdot \left[\frac{k_r K_{sat}}{K_{ref}}\nabla h\right] \tag{44}$$

where $k_r K_{sat}/K_{ref} \cong 1$ and

$$D \equiv K_{ref}/C \tag{45}$$

is an approximate hydraulic diffusivity for unsaturated flow.

2.11 Hydraulic diffusion timescales

Diffusion of a solute c in one-dimension follows Fick's second law

$$\frac{\partial c}{\partial t} = D\frac{\partial^2 c}{\partial x^2} \tag{46}$$

where D is the diffusion coefficient [L^2/T] in Fick's first law. For $c = 0$ initially in a semi-infinite medium and $c = c_0$ subsequently imposed at the boundary $x = 0$, the analytical solution of Equation (46) is

$$c(x,t) = c_0 erfc\left(\frac{x}{\sqrt{4Dt}}\right) \tag{47}$$

The ratio c/c_0 is equal to 0.16 when $x/\sqrt{4Dt} = 1$. If $c = 0.16$ is deemed significant, then the *characteristic time* for significant penetration of c to a depth of L is

$$\tau = \frac{L^2}{4D} \tag{48}$$

The above mathematics apply to analogous entities governed by diffusion, such as temperature in the case of heat conduction. Equations (40) and (44) are diffusion equations in the form of Equation (46). Thus, the time scale characteristic of hydraulic diffusion (penetration of a hydraulic head front) is given by Equation (48) with D interpreted as hydraulic diffusivity.

2.12 Specific storage coefficient

The specific storage coefficient (S_s [1/L]) introduced in connection with Equation (39) is defined as the volume of water per unit total volume drained per unit decrease in hydraulic head (Freeze and Cherry 1979). Specific storage coefficient depends on the compressibilities of the solid, liquid, and bulk structure per the relationship

$$S_s = \rho g(n\beta_\ell - n\beta_s + \alpha_b) \tag{49}$$

where ρg = specific weight of water [M/L^{2}T^2], n = porosity [-], β_ℓ = liquid compressibility [LT^2/M], β_s = solid compressibility [LT^2/M], and α_b = bulk compressibility [LT^2/M] (de Marsily 1986 p. 108). However, the liquid and solid compressibilities are expected to be negligible for saltstone grout (see Section 3.0) reducing Equation (49) to

$$S_s = \rho g \alpha_b \tag{50}$$

Bulk compressibility is the inverse of bulk modulus (B) in structural mechanics

$$\alpha_b = \frac{1}{B} \tag{51}$$

Bulk modulus is a function of Young's modulus (E) and Poisson's ratio (ν):

$$B = \frac{E}{3(1-2\nu)} \tag{52}$$

Thus, specific storage coefficient can be estimated from Young's modulus and Poisson's ratio data.

2.13 PFLOTRAN porosity compressibility

The PFLOTRAN code (https://www.pflotran.org/), chosen for numerical flow simulations, represents compressibility in an alternative manner. PFLOTRAN was found to be more robust numerically than alternative porous-media flow codes and selected for that reason. Using the POROSITY_EXPONENTIAL option, porosity is calculated as a function of pressure as

$$n = n_0 exp[C_0(P - P_0)] \tag{53}$$

where C_0 is a POROSITY_COMPRESSIBILITY constant [LT^2/M] the "0" subscript otherwise denotes a reference (initial) condition. From the definition of specific storage coefficient and assuming full saturation

$$S_s = \frac{1}{V}\frac{dV_w}{dp} = \rho g \frac{dn}{dP} = \rho g \cdot n_0 exp[C_0(P - P_0)] \cdot C_0 = \rho g n C_0 \tag{54}$$

In the above derivation *the total volume of the porous medium is assumed to be constant*, as will be the case in a conventional numerical model with a fixed grid. Thus,

$$C_0 = \frac{S_s}{\rho g n} \tag{55}$$

In terms of bulk compressibility

$$C_0 = \frac{\alpha_b}{n} \tag{56}$$

using Equation (50). Equations (55) and (56) allow one to translate conventional compressibility parameters into PFLOTRAN input.

In principal the total volume of the porous medium changes with pressure, such that $C_0 = (1-n)\,\alpha_b/n$ as stated in the online PFLOTRAN user guide at https://documentation.pflotran.org/user_guide/cards/subsurface/material_property_card.html. However, experimentation with the code confirms that porosity compressibility must be defined according to Equations (55) and (56) to achieve the expected drain volume per unit head decrease. This outcome is believed to be a result of the modeling grid being fixed, such that while porosity changes, total volume in the model simulation does not.

2.14 Fractures

A *fractured-medium* is a material that contains fractures along with fine-scale pores. The hydraulic conductivity of a saturated smooth-wall fracture is

$$K_f = \frac{\rho g b^2}{12\mu} \tag{57}$$

with units [L/T] where ρg = specific weight of water [M/L^2T^2], b = aperture [L], and μ = viscosity [M/LT] (e.g. Wang and Narasimhan 1985). Physical degradation of cementitious materials typically takes the form of cracking, in which case the high conductivity of saturated fractures makes them an important consideration. Fractures function as fast-flow paths when saturated.

Fractures are easily dewatered though, greatly reducing their impact. The threshold for 100% saturation is

$$\psi_c = \frac{2\sigma}{\rho g b} \tag{58}$$

where σ = surface tension [M/T^2] and the other symbols are as defined above. When matric suction exceeds this value, water can no longer bridge the aperture and snaps back to thin films, such that the fracture is practically air-filled. Film flow greatly reduces fracture hydraulic conductivity (e.g. Or and Tuller 2000).

2.15 Effective hydraulic conductivity

Porous materials commonly exhibit some level of physical heterogeneity. In the context of saltstone, heterogeneity could potentially take the form of cracks, cold joints, and/or layers with distinct properties due to batching and process variations. The effective hydraulic conductivity, K_{eff} [L/T], of a heterogeneous region is the scalar conductivity that reproduces total flow for the same gradient. For the simple case of flow parallel to distinct horizontal layers, K_{eff} is given by

$$K_{eff} = \frac{\sum K_i \Delta z_i}{\sum \Delta z_i} \tag{59}$$

where Δz_i is layer thickness [L], and K_i = layer conductivity [L/T].

3.0 Saltstone Waste Form

Table 3-1 summarizes the material properties of saltstone waste and fluid properties used in initial calculations. Properties taken from SRMC-CWDA-2019-00001 and SRR-CWDA-2018-00004 directly supporting the 2020 Saltstone Disposal Facility Performance Assessment. The Young's modulus information from SRNL-STI-2011-00665 and WSRC-TR-2007-00437 does not directly support the PA. Figure 3-1 through Figure 3-3 present the moisture characteristic and unsaturated hydraulic conductivity curves for saltstone based on Table 3-1.

As discussed in SRR-CWDA-2018-00004, the saturated hydraulic conductivity value in Table 3-1 is based on the Dynamic Leaching Method (DLM) described in SREL DOC No. R-16-0003. The permeant was a groundwater simulant, rather than a liquid representative of the initial saltstone pore solution. Therefore, the properties of water listed in the table are used to calculate intrinsic permeability. To be consistent with the κ calculation, other saltstone properties in Table 3-1 are calculated assuming water as the pore fluid.

The air-entry pressure head for saltstone calculated as the inverse of the vGM α parameter is 44,000 cm. The water retention curve shown in Figure 3-1(a) indicates a smaller value around ψ_a = 3000 cm. From a gravity equilibrium perspective, saltstone would have to lie at least 30 meters (100 ft) above the water table to experience an unsaturated state.

The bulk compressibility (α_b) of 3.41E-07 Pa^{-1} confirms the expectation that liquid (~5.E-10 Pa^{-1}) and solid (~2.E-11 Pa^{-1} for quartz and most minerals) compressibilities are negligible, as asserted in Section 2.12 (de Marsily 1986).

Table 3-2 calculates timescales for hydraulic diffusion (penetration of a pressure head transient) for two characteristic dimensions of SDU 6. The 375 ft diameter footprint of SDU 6 is equivalent to a square of side length 332 ft, which is adopted as the characteristic length for one-dimensional horizontal flow calculations. This study focuses on SDU 6 during December 2022 when the grout thickness was approximately 13.1 ft. This dimension is adopted as the characteristic length for horizontal flow. The timescale for horizontal flow is more than 50,000 years, indicating no hydraulic communication between the furthest separated drainwells at operational timescales. The vertical timescale is nearly 100 years, which is much shorter but still far too long to influence SDU 6 operations.

Table 3-1: Material and fluid properties related to saltstone grout.

Parameter	Value	Units	Comments
Gravitational acceleration, g	9.81	m/s^2	
Density of water, ρ	998	kg/m^3	
Specific weight of water, ρg	9790.38	N/m^3	
Viscosity of water, μ	0.001	kg/m-s	
Surface tension of water, σ	0.07275	N/m	
Total porosity, n	0.656	mL void/mL	SRR-CWDA-2018-00004
Solid phase density, ρ_s	2.72	g/mL	SRR-CWDA-2018-00004
Dry bulk density, ρ_b	0.932	g/mL	SRR-CWDA-2018-00004
Saturated hydraulic conductivity, K_{sat}	5.0E-12 5.0E-10	m/s cm/s	Isotropic, SRR-CWDA-2018-00004
Intrinsic permeability, κ	5.11E-19	m^2	Equation (11)
Effective diffusion coefficient, D_e	1.3E-12 1.3E-08	m^2/s cm^2/s	SRR-CWDA-2018-00004
van Genuchten-Mualem θ_s	0.58	mL water/mL	SRMC-CWDA-2019-00001
van Genuchten-Mualem θ_r	0	mL water/mL	SRMC-CWDA-2019-00001
van Genuchten-Mualem $S_r = \theta_r/\theta_s$	0	mL water/mL void	Calculated
van Genuchten-Mualem α	2.254E-05	1/cm	SRMC-CWDA-2019-00001
van Genuchten-Mualem n	1.67131	-	SRMC-CWDA-2019-00001
van Genuchten-Mualem m	0.4017	-	Calculated as $1 - 1/n$
Approximate air-entry pressure head, ψ_a	444 4.44E+04	m cm	Calculated as $1/\alpha$
Young's modulus, E	5.28E+06	Pa	Geometric average of [2.56, 10.9] GPa, the range of values reported in SRNL-STI-2011-00665 and WSRC-TR-2007-00437
Poisson' ratio, ν	0.2	-	Assumed
Bulk modulus of elasticity, B	2.93E+06	Pa	Equation (52)
Bulk compressibility, α_b	3.41E-07	1/Pa	Equation (51)
Specific storage coefficient, S_s	3.34E-03 3.34E-05	1/m 1/cm	Equation (50)
PFLOTRAN porosity compressibility, C_0	5.2E-07	1/Pa	Equation (55) or (56)
Hydraulic diffusion coefficient, D	1.5E-09 1.5E-05	m^2/s cm^2/s	$D \equiv K_{sat}/S_s$

Figure 3-1: Water retention curve for saltstone: (a) logarithmic, and (b) linear scale.

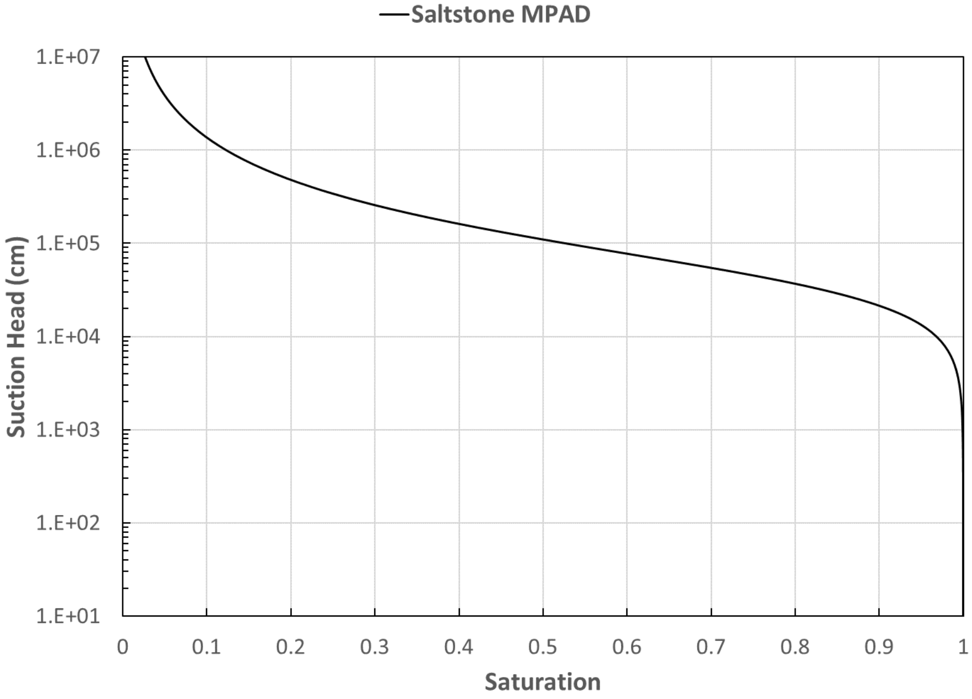

(a)

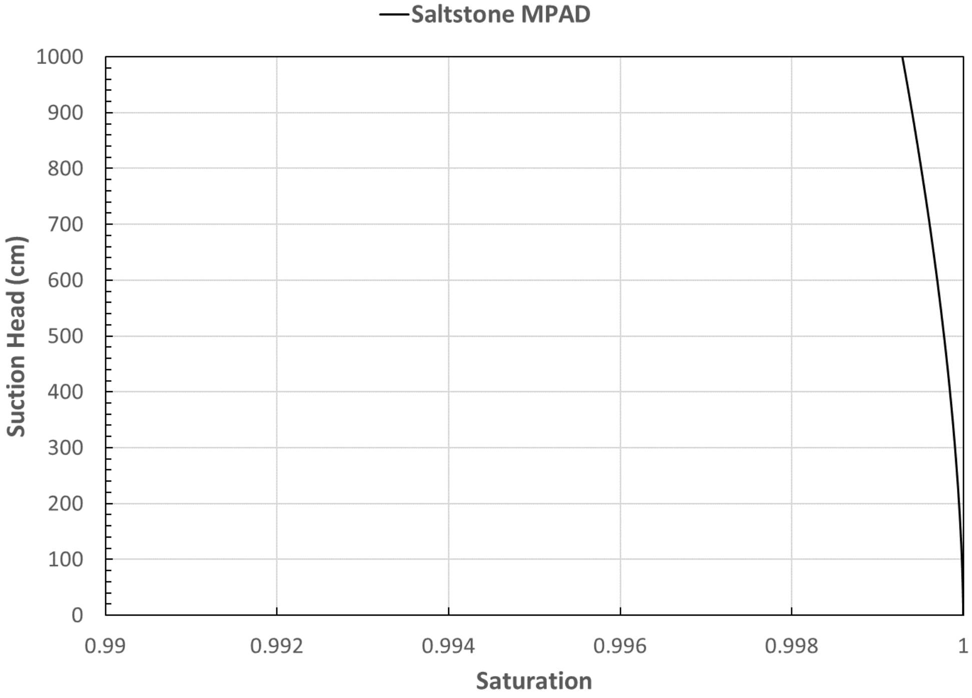

(b)

Figure 3-2: Relative permeability curve for saltstone.

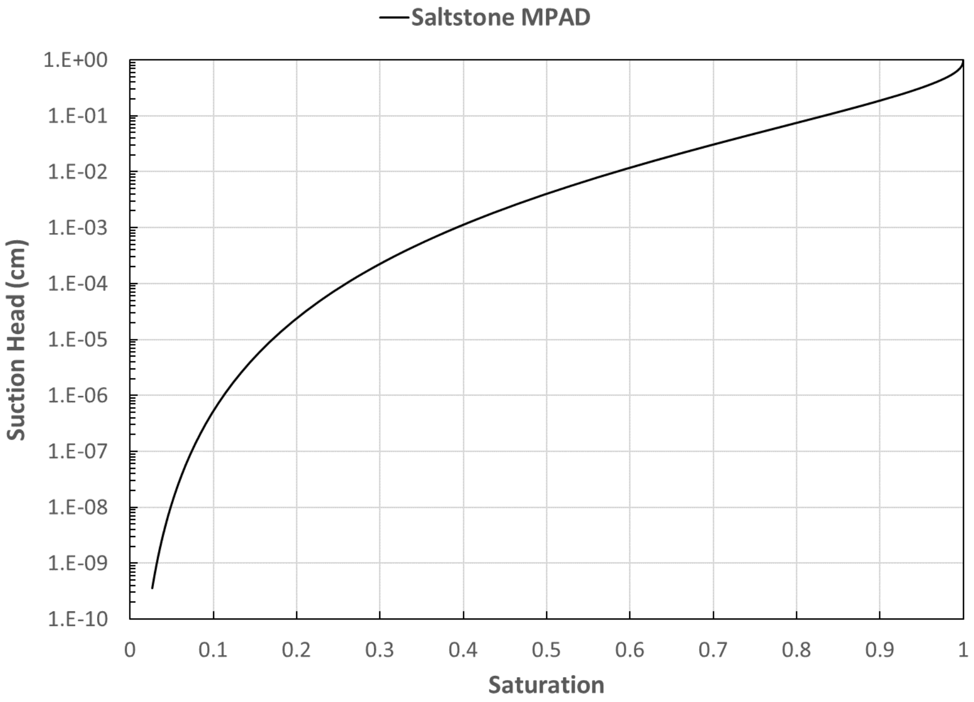

Figure 3-3: Unsaturated hydraulic conductivity for saltstone.

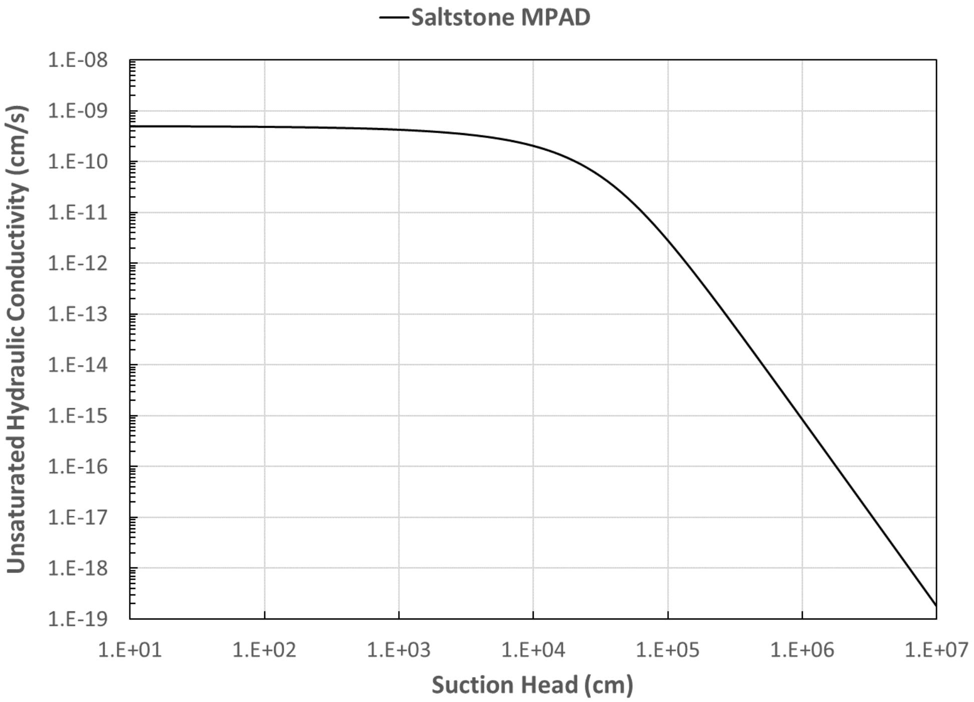

Table 3-2: Hydraulic diffusion timescales under saturated conditions.

Parameter	Horizontal	Vertical	Units	Comments
Hydraulic conductivity, K_{sat}	5.0E-10 5.0E-12	5.0E-10 5.0E-12	cm/s m/s	SDF PA assumption SRR-CWDA-2018-00004 Rev. 1
Specific storage coeff., S_s	3.34E-03	3.34E-03	1/m	Estimated (Table 3-1)
Hydraulic diffusivity, D	1.5E-09	1.5E-09	m^2/s	Equation (41)
Characteristic length, L	332 101	13.1 4.0	ft m	332' square equiv. to 375' circle; 13.1 ft is grout height in Dec 2022
Timescale for hydraulic diffusion, τ	1.7E+12 54190	2.7E+09 84	s yr	Equation (48)

3.1 Initial saturation state

The saturation state of initially cured saltstone has not been characterized to the author's knowledge but can be estimated using equilibrium geochemical modeling. SRR-CWDA-2021-00034 describes equilibrium chemistry thermodynamic databases and models for analyzing SRS waste tank fill grout. Both The Geochemist's Workbench (GWB, https://www.gwb.com/) and PHREEQC (https://www.usgs.gov/software/phreeqc-version-3) were used in that study. The PHREEQC database and model were subsequently extended to saltstone as described in SRR-CWDA-2021-00052.

An important assumption is the fraction of the dry ingredients that react with water in the near term. For tank grout SRR-CWDA-2021-00034 estimated the following hydrations: 100% cement / 70% slag / 20% fly ash. Here the mixing fluid was water and laboratory samples were cured for a short period compared to PA timescales. Over longer curing periods and/or considering high-pH salt solution as the mixing fluid, complete hydration defines the other end of the spectrum: 100% cement / 100% slag / 100% fly ash reactivity. With respect to initial saturation, lower reactivity leads to higher initial saturation. From the purpose of defining a maximum initial saturation, PHREEQC results for 100% cement / 70% slag / 20% fly ash hydration are presented herein.

The C-S-H gel in a cementitious material can be modeled as a suite of minerals with fixed stoichiometry and equilibrium constants using the "EQUILIBRIUM_PHASES" keyword; here each component of the solid solution is treated as an independent pure phase. Alternatively, C-S-H gel can be modeled as a solid solution ("SOLID_SOLUTIONS" keyword) whereby the equilibrium constant for a solid solution component is taken as the ion activity product for the dissolution reaction divided by its mole fraction. Both approaches were considered in SRR-CWDA-2021-00052.

The extended Debye-Hückel activity model associated with the CEMDATA18.1 database is accurate for ionic strengths to about one molal. The pore solutions of grouts prepared with salt solution have simulated ionic strengths that exceed three molal. Therefore, three variations on the mix solution were considered in SRR-CWDA-2021-00052: SDF salt solution, salt solution except the $NaSO_4$ component diluted to achieve about one molal ionic strength in grout pore solutions, and pure water. The simulation assuming a full-strength salt solution as the mixing fluid produced the highest saturation, so results are presented herein for this case.

Table 3-3 shows the ingredients and mix proportions for 45/45/10 saltstone, the formulation placed in SDU 6 during the period of interest. "Inert B" refers to dissolved salts in the mixing fluid. Also shown in the table are the corresponding molar inputs to PHREEQC. The EQUILIBRIUM_PHASES and SOLID_SOLUTIONS simulations produced a similar saturation result, so only the PHREEQC outputs from the latter are presented in Table 3-4. Table 3-5 shows the saturation calculation. The result is a theoretical initial saturation of 80%.

3.2 Equilibrium saturation state

Whatever the saturation state of saltstone when cured in isolation, SDU 6 observations and porous-medium theory suggest the grout will quickly become fully saturated, if not already, when exposed to its surroundings. SPF equipment and process lines between SPF and SDF are flushed with water before and after grout placement, adding to the design mix water. Each process run produces 1000-2000 gallons of free-standing (drain) water comprising some combination of bleed water emanating from the grout prior to setting and process system flush water (SRMC-CWDA-2024-00045). The 45/45/10 saltstone mix placed in SDU 6 through August 2021 produces about 0.7 wt% of the salt solution as bleed (SRR-CWDA-2020-00008). Prior to initial pumping of SDU 6 in April 2022, around 200,000 gallons of drainwater had accumulated at the wall due to the floor and grout slopes (Figure 3-4, SRMC-CWDA-2024-00045). Unsaturated grout in direct contact with free-standing water would imbibe water and saturate quickly due to capillary suction within grout and positive pressure at the interface. Free-standing water and a relatively confined air space keep the humidity high in an SDU. For example, Figure 3-5 shows humidity measurements in SDU 2A from May-June 2013 (SRR-SPT-2013-00044). Humidity appears to average around 97%. Grout in contact with the humid air space would equilibrate to a total suction defined by the Kelvin relationship and osmotic suction would drive capillary suction to a lower value.

Table 3-6 defines a representative pore solution for cured saltstone. The highly concentrated solution creates a large osmotic suction per the Morse equation, roughly 2440 meters as shown in Table 3-7. The fluid properties of water approximate those of the pore solution in the calculation, but this choice does not affect the conclusion of the analysis. For a relative humidity of 97%, total suction is 420 meters. Capillary suction is a negative number per Equation (14) implying saturated instead of unsaturated conditions. Thus 100% saturation is predicted at equilibrium. Table 3-7 includes a parallel calculation assuming the saltstone pore solution is plain water. In this case, equilibrium saturation is 77%. Therefore, consideration of osmotic effects is important for saltstone.

To summarize, saltstone grout in SDU 6 is generally expected to be saturated due to process line flushing, accumulated flush and bleed water forming a standing pool on top of a portion of grout (during the analysis period), and high humidity conditions inside an SDU.

Table 3-3: Saltstone 45/45/10 formulation and PHREEQC inputs for 100% cement / 70% slag / 20% fly ash hydration.

Parameter	**Cement**	**Slag**	**Fly Ash**	**Silica Fume**	**Metakaolin**	**Inert B**	**Dry mix**	**Water**	**w/c (weight) ratio**	**w/dry mix**		**Notes:**		
Mix (lbs/yd3)	157.6	709.4	709.4			350.6	1927	967.3	0.614	0.502		-- C-SPP-F-00055 Rev. 6		
(kg/m3)	94	421	421	0	0	208	1143	573.9				1717		
All ingredients fraction	0.054	0.245	0.245	0.000	0.000	0.121	0.666	0.334						
Dry ingredients fraction	0.082	0.368	0.368	0.000	0.000	0.182	1							
Binders fraction	0.10	0.45	0.45	0.00	0.00		1							
Parameter	**Cement**	**Slag**	**Fly Ash**	**Silica Fume**	**Metakaolin**	**Inert B**		**Binders**	**Dry Mix**		**MW**	mol/	**GWB /**	**PHREEQC**
Proportions	g/100g	g/100g	g/100g	g/100g	g/100g			g/100g	g/100g	g/kg	g/mol	kg dry mix		mol/m3
Reactive ingredients	97.4	98.8	93.0	96.3	98.5									
C (CaO)	64.6	39.0	4.2	0.6	0.2			19.1	15.63	156.3	56	2.792	C (CaO)	3192
S (SiO2)	20.4	36.5	50.9	95.0	53.1			18.1	14.82	148.2	60	2.470	S (SiO2)	2824
A (Al2O3)	5.0	10.5	27.9	0.2	43.6			6.3	5.17	51.7	102	0.506	A (Al2O3)	579.0
F (Fe2O3)	3.5	0.4	8.7	0.1	1.6			1.3	1.04	10.4	160	0.065	F (Fe2O3)	74.34
Sbar (SO3)	2.8	2.3	0.3	0.2	0.0			1.0	0.83	8.3	80	0.104	Sbar (SO3)	118.67
M (MgO)	1.2	10.1	0.9	0.2	0.1			3.4	2.78	27.8	40	0.695	M (MgO)	794.0
Inert A	2.6	1.2	7.0	3.8	1.5	100.0		50.8	41.54	415.4				
Inert B									18.19	181.9				
Water									50.20	502.0	18	27.887	H (H2O)	31882
checks	100	100	100	100	100	100		100	100	1000				
Degree of rxn/hydration	100%	70%	20%						0.614	0.614				
Parameter	**Cement**	**Slag**	**Fly Ash**	**Silica Fume**	**Metakaolin**	**Total**							Fe	148.7
Reducing capacity (μeq/g)		819											FeO (FeII)	148.68
Reducing capacity (eq/m3)	0.0	241.3	0.0	0.0	0.0	241.28							Fe2O3 (FeIII)	0.00
Unreacted dry mix (kg/m3)	0	126.26	336.7	0	0	462.96								

Table 3-4: PHREEQC outputs for 100% cement / 70% slag / 20% fly ash hydration and SOLID_SOLUTION.

Phase	MW (g/mol)	MV (mL/mol)	Moles	Mass (g)	Volume (mL)	Density (g/mL)
5CA	172.205675	57.3	3.750E+02	6.458E+04	2.149E+04	3.01
AlOHmic	78.0055	31.956		0.000E+00	0.000E+00	0.00
Brc	58.328	24.63		0.000E+00	0.000E+00	0.00
C4AH13	560.491	274.47		0.000E+00	0.000E+00	0.00
Cal	100.0911	36.934		0.000E+00	0.000E+00	0.00
Fe-ettringite	1312.878	717.56		0.000E+00	0.000E+00	0.00
Ferrihydrite	106.8677	106.8677	1.490E+02	1.592E+04	1.592E+04	1.00
Gp	172.176	74.69		0.000E+00	0.000E+00	0.00
INFCA	173.200825	59.31	6.140E+01	1.063E+04	3.642E+03	2.92
M4A-OH-LDH	443.371	219.1	1.985E+02	8.801E+04	4.349E+04	2.02
Mag	231.5386	44.524		0.000E+00	0.000E+00	0.00
Maghemite	159.691	29.087		0.000E+00	0.000E+00	0.00
Portlandite	74.096	33.06		0.000E+00	0.000E+00	0.00
Py	119.975	23.94		0.000E+00	0.000E+00	0.00
Qtz	60.0843	22.688		0.000E+00	0.000E+00	0.00
T2C-CNASHss	189.2443	80.6	6.910E+01	1.308E+04	5.569E+03	2.35
T5C-CNASHss	190.245375	79.3	4.640E+01	8.827E+03	3.680E+03	2.40
TobH-CNASHss	191.24645	85	1.050E+00	2.008E+02	8.925E+01	2.25
ettringite	1255.147	707.03	7.876E+00	9.886E+03	5.569E+03	1.78
hemicarbonat10.5	537.45655	261.264		0.000E+00	0.000E+00	0.00
monocarbonate	568.4701	261.958	1.644E+02	9.346E+04	4.307E+04	2.17
INFCN	186.9655	71.07	5.840E+02	1.092E+05	4.150E+04	2.63
INFCNA	188.3093	64.51	1.040E+03	1.958E+05	6.709E+04	2.92
5CNA	183.192	64.51	1.370E+02	2.510E+04	8.838E+03	2.84

Table 3-5: Saturation calculation for 100% cement / 70% slag / 20% fly ash hydration and SOLID_SOLUTION.

PHREEQC hydration -- initial				Mass (g)	Volume (mL)	Density (g/mL)	Volume Fraction	Porosity	Water Content	Saturation	Comments
			Inert:	4.630E+05	1.760E+05	2.63	17.6%				Inert B + unreacted binders
			Minerals:	6.347E+05	2.599E+05	2.44	26.0%				Hydrated minerals
			Water (unreacted):	4.482E+05	4.482E+05	1.00	44.8%	**56.4%**	**44.8%**	**79.5%**	
Water mass	4.48E+02	kg	Air:		1.158E+05		11.6%				
			Total:	1.546E+06	1.000E+06	**1.55**	100.0%				

Figure 3-4: Video still of standing water at the SDU 6 in January 2022.

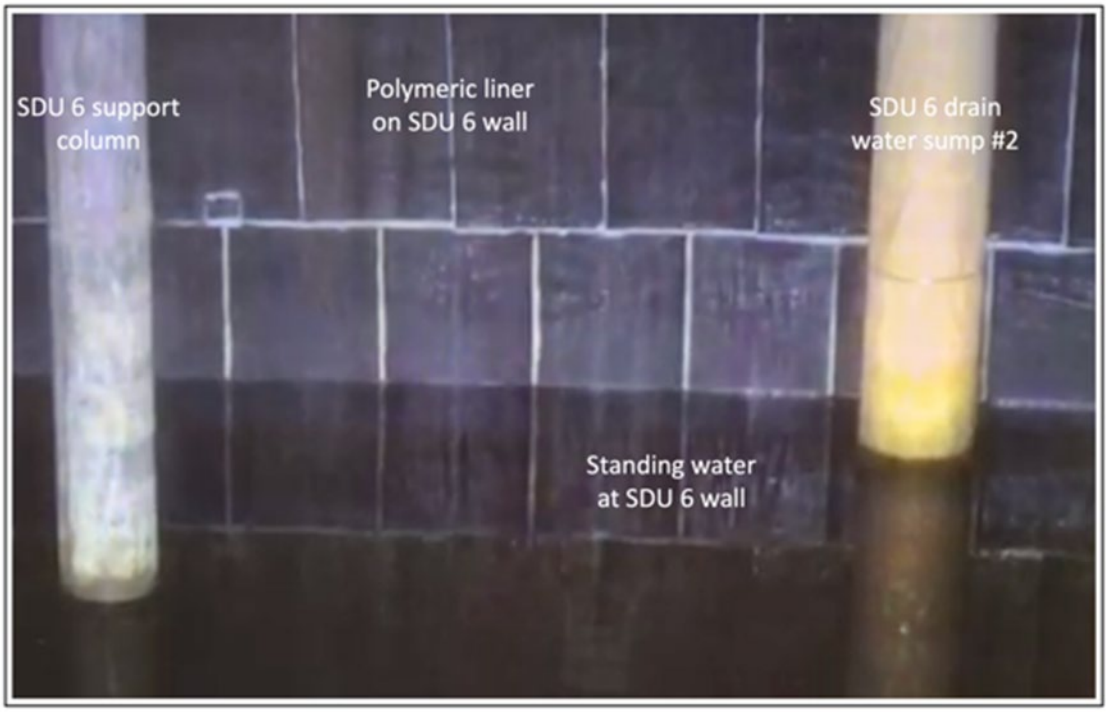

[SRMC-CWDA-2024-00045]

Figure 3-5: Humidity measurements in SDU 2A from 2013.

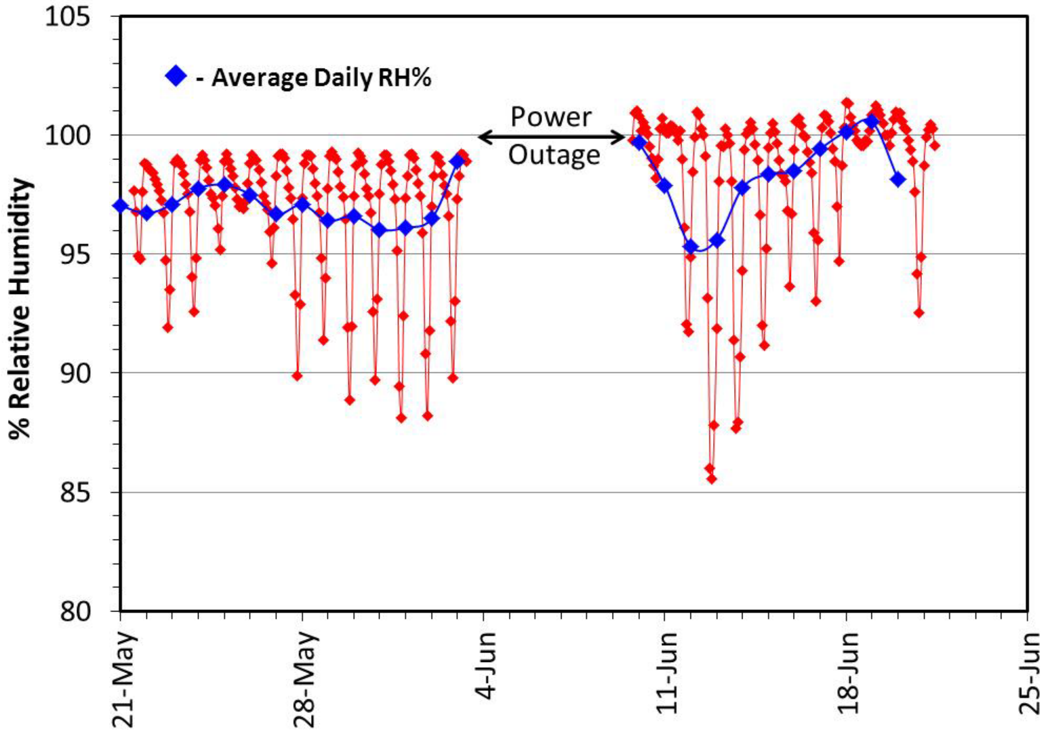

[SRR-SPT-2013-00044]

Table 3-6: Saltstone pore solution chemistry.

Ion	MW (g/mol)	Conc. (mol/L)	Conc. (g/L)	Charge	cz^2‡
OH-	17	0.0905	1.539	-1	0.0905
Na+	23	4.7847	110.048	1	4.7847
K+	39	0.2123	8.28	1	0.2123
SO4--	96	0.1355	13.008	-2	0.5420
Ca++	40	0.0024	0.096	2	0.0096
Cl-	35	0.0047	0.165	-1	0.0047
N*	60.4†	4.5692	275.94	-1	4.5692
CO3--	60	0.0015	0.09	-2	0.0060
	Total:	**9.8008**		**Ionic strength:**	**5.1095**

* NO3 and NO2 as N

† calculated from NO2 and NO3 molar ratios in mixing liquid used to batch the waste form

Source: SRR-CWDA-2018-00004 Rev. 1

‡ concentration (c) times the square of charge (z)

Table 3-7: Total, osmotic, and capillary suctions for salt solution and water.

Parameter	Salt Solution	Water	Units	Comments
Molar gas constant, R	8.314	8.314	J/K-mol	
Gravitational acceleration, g	9.81	9.81	m/s^2	
Fluid properties:				
Molar mass of water, M_w	18 0.018	18 0.018	g/mol kg/mol	Approximate for
Density of water, ρ	998	998	kg/m^3	salt
Specific weight of water, ρg	9790.38	9790.38	N/m^3	solution
Exposure environment:				
Absolute temperature, T	293.15	293.15	K	20 C
Relative humidity, RH	97%	97%		SRR-SPT-2013-00044
Total suction:				
Total suction head, ψ	420	420	m	Kelvin relationship, Eq. (22)
Osmotic suction:				
van't Hoff factor, i	1	1	-	Assumption
Pore solution ion concentration, M	9.8 9800	0 0	mol/L mol/m^3	Salt solution from Table 3-6
Osmotic suction head, π	2440	0	m	Morse relationship, Eq. (21)
Capillary suction:				
Capillary suction head, ψ_c	-2019	420	m	Equation (14)
Effective ψ_c	0	420	m	Applying $\psi_c \geq 0$ limit
Saturation:				
van Genuchten-Mualem θ_s	0.58	0.58	-	Table 3-1
van Genuchten-Mualem θ_r	0	0	-	Table 3-1
van Genuchten-Mualem α	2.25E-05 2.25E-03	2.25E-05 2.25E-03	1/cm 1/m	Table 3-1
van Genuchten-Mualem n	1.67131	1.67131	-	Table 3-1
van Genuchten-Mualem m	0.4017	0.4017	-	Table 3-1
Effective saturation, S_e	1	0.77	-	Equation (16)
Residual saturation, S_r	0	0	-	
Saturation, S	100%	77%	-	Equation (16)

4.0 SDU 6 Drain Well Observations

This study focuses on the period November 15, 2022 through April 15, 2023 when SDU 6 drainwell water levels were clearly below the top of the grout everywhere and no grout placements occurred to complicate data interpretation. The grout elevation during this period was reported to be 13.25 ft (4.0 m) in monthly status report “Saltstone Combined PI 5-1-23.pdf”. SRMC-CWDA-2024-00045 states the uniform grout thickness to be 10.5 ft. Considering the floor slope and measurement uncertainties, these values are consistent.

Figure 4-1 shows drainwell (“DW”) water levels as reported by the facility, which is the water height above the sump in each well. Drawdowns during pumping (“Drainwater removal” days) are excluded to avoid clutter at this stage. Due to the 1.5% floor slope and slightly different sump construction, sump elevations differ by 2.2 ft between the inner and outer radius wells. Thus, the offset shown in Figure 4-1 is an artifact of different sump elevations. Rather, all wells exhibit nearly the same water level referenced to a fixed elevation. Going forward water levels will be referenced to the sump elevation of the outer drainwells, such that any differences reflect hydraulic disequilibrium.

Two distinct drawdowns are observed in Figure 4-1. The rapid drawdown during the first week of December is a result of pumping from Drainwell 1. The otherwise gradual drawdown is hypothesized to potentially be a result of leakage to the SDU 6 East Sump (SRMC-CWDA-2023-00032). This hypothesis is supported by SDU 7 drainwell observations, which do not show a similar drop in water levels (SRMC-CWDA-2024-00045 Figure 43). Near constant water levels in SDU 7 during periods of processing inactivity suggest leakage specific to SDU 6 instead of evaporation and/or sorption by saltstone (“replenishment” in the parlance of SRMC-CWDA-2024-00045). However, evaporation, sorption, or other unidentified phenomena cannot be ruled out. The East Sump is located on the east side of SDU 6 at the interface between the Lower and Upper Mud Mats. SRMC-CWDA-2023-00032 discusses ten potential flow paths that could lead to water accumulation in the East Sump. A definitive conclusion on the East Sump leak path could not be reached. However, drainage to the sump does not imply a subsequent release to the environment.

Figure 4-1: SDU 6 drainwell water levels.

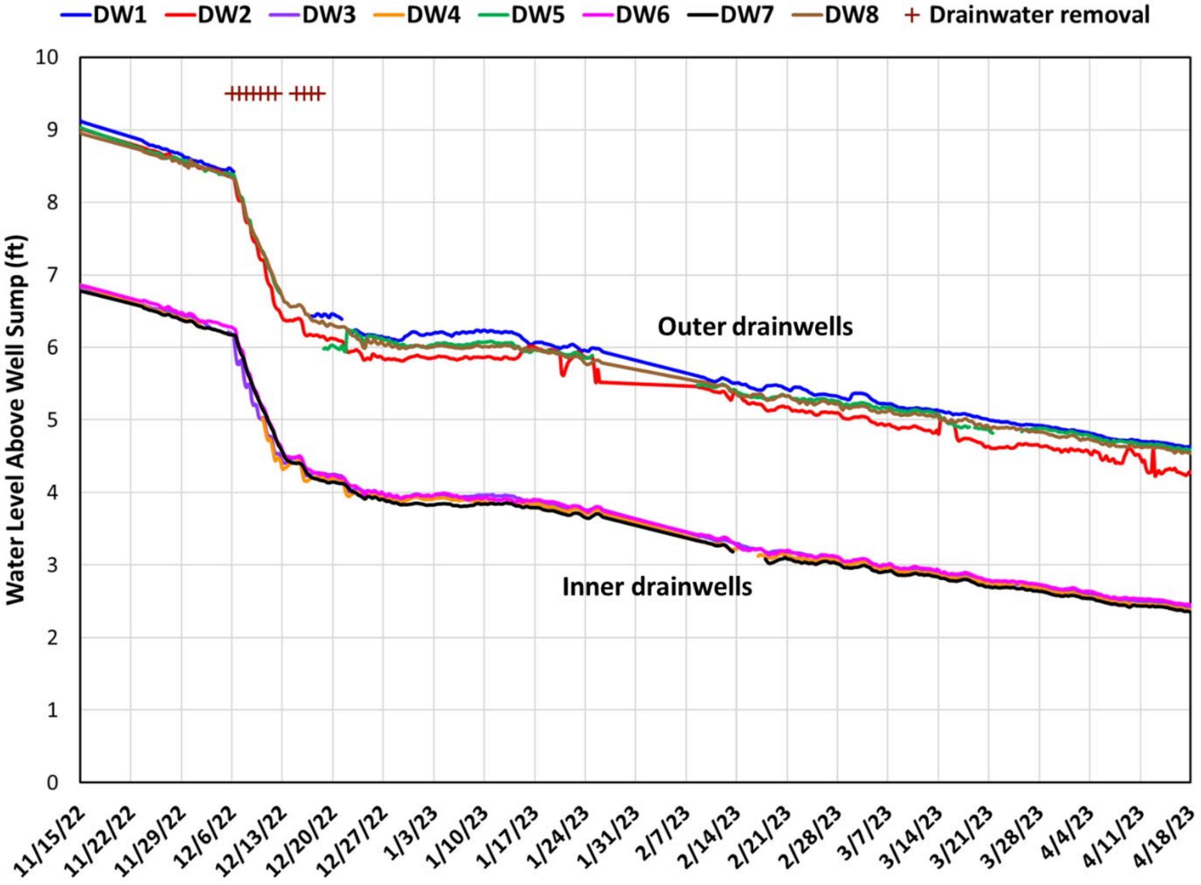

4.1 Drainwell pumping

Drainwell 1 was pumped on 9 days during the period December 6-25, 2022 as shown in Figure 4-2. For this study drain volumes were estimated as cumulative drawdown multiplied by the cross-sectional area of Drainwell 1. Calculated drain volumes agree reasonably well with other estimation methods, such as flow totalizer instrumentation and integration of pump flowrate reading. The total volume drained in December 2022 is 5188 gallons. Figure 4-3 shows the period December 6-15 in greater detail. The drawdown for this period is 8.44 ft (257 cm) to 6.6 ft (201 cm). The water level on 12/25 is 6.2 ft (190 cm). An empirical specific storage coefficient can be calculated from these data as

$$S_s = \frac{\Delta V_w}{V}\frac{1}{\Delta h} \tag{60}$$

where ΔV_w = drain volume, V = grout volume, and Δh = drawdown. The calculation is shown in Table 4-1. The drainwells furthest from Drainwell 1 appear to respond to pumping from Drainwell 1 within a day. Assuming a specific timescale of 18 hours implies an effective (Section 2.15) horizontal hydraulic conductivity of 3.E-03 cm/s per Equations (41) and (48), as shown in Table 4-1.

Table 4-1: Hydraulic conductivity inferred from SDU 6 drawdown observations.

Parameter	Value	Units	Comments
SDU 6 diameter	375 114.3	ft m	
Area	10261	m^2	
Grout level, Δz	4.0	m	December 2022
Grout volume, V	4.10E+04	m^3	
Estimated drain volume, ΔV_w	5188 1.96E+01	gal m^3	December 6-25, 2022 *Assumes all water drained from grout*
Drawdown, Δh	0.67	m	
Specific storage coefficient, S_s	7.1E-04	1/m	Equation (60)
Characteristic length, L	332 101	ft m	332 ft = square equivalent to 375 ft circle
Timescale for hydraulic diffusion, τ	18 6.5E+04	h s	12/6-13/2022 drainwell observations
Hydraulic diffusion coefficient, D	4.0E-02	m^2/s	Equation (48)
Hydraulic conductivity, K_{sat}	2.8E-05 2.8E-03	m/s cm/s	Equation (41)

Figure 4-4 shows the recovery of Drainwell 1 after the first pumping event on December 6, 2022. Because SDU 6 was in quasi-equilibrium beforehand, the first recovery can be analyzed as a slug test. Figure 4-5 and Figure 4-6 show Bouwer-Rice and Cooper-Greene slug test analyses, respectively, for first recovery using spreadsheet tools from the United States Geological Survey (Open-File Report 02–197). Each figure provides two candidate interpretations for each method. The slug test interpretations indicate a saturated hydraulic conductivity around 3.0E-3 cm/s, consistent with K_{sat} inferred from hydraulic diffusion timescale (2.8E-03 cm/s).

Figure 4-2: SDU 6 drainwell pumping, December 6-25, 2022.

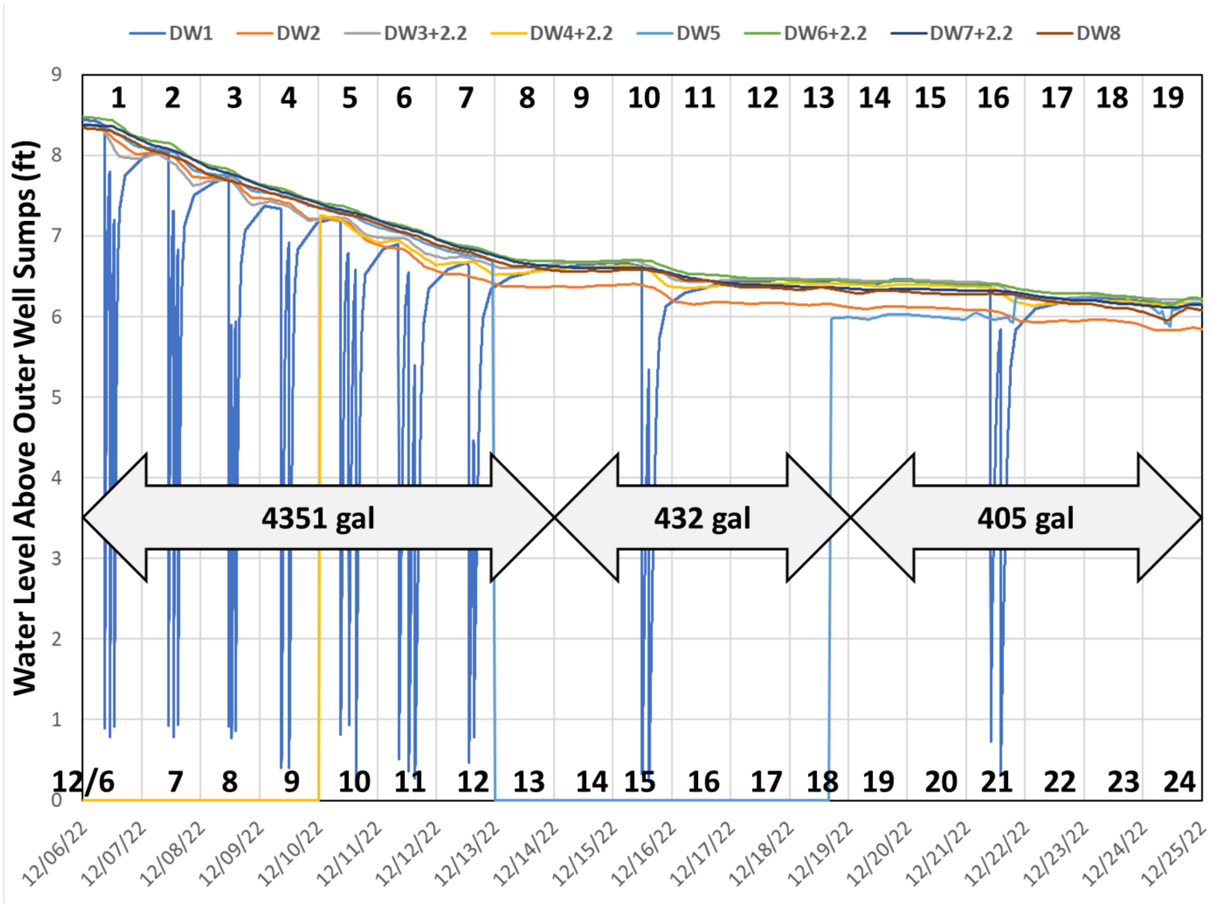

Figure 4-3: SDU 6 drawdowns, December 6-15, 2022.

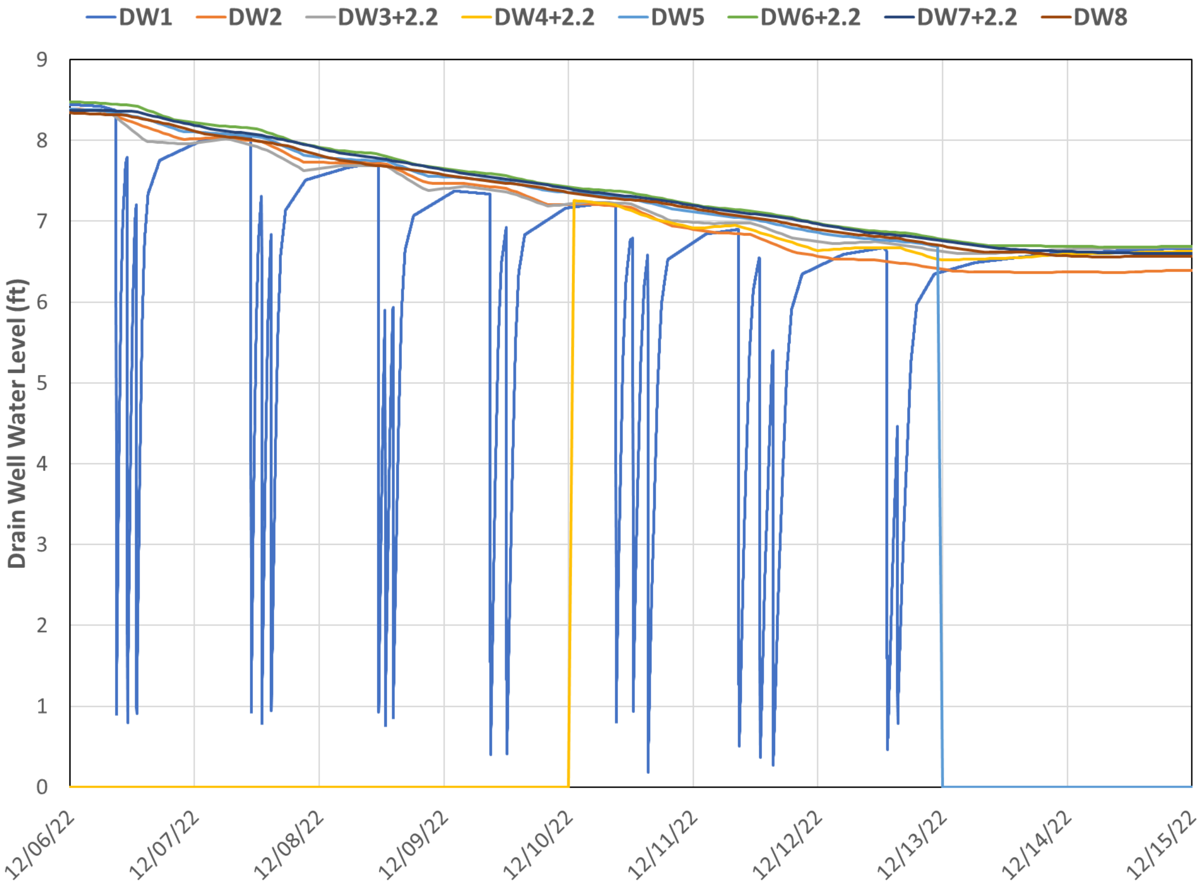

Figure 4-4: First recovery of Drainwell 1 on December 6, 2022.

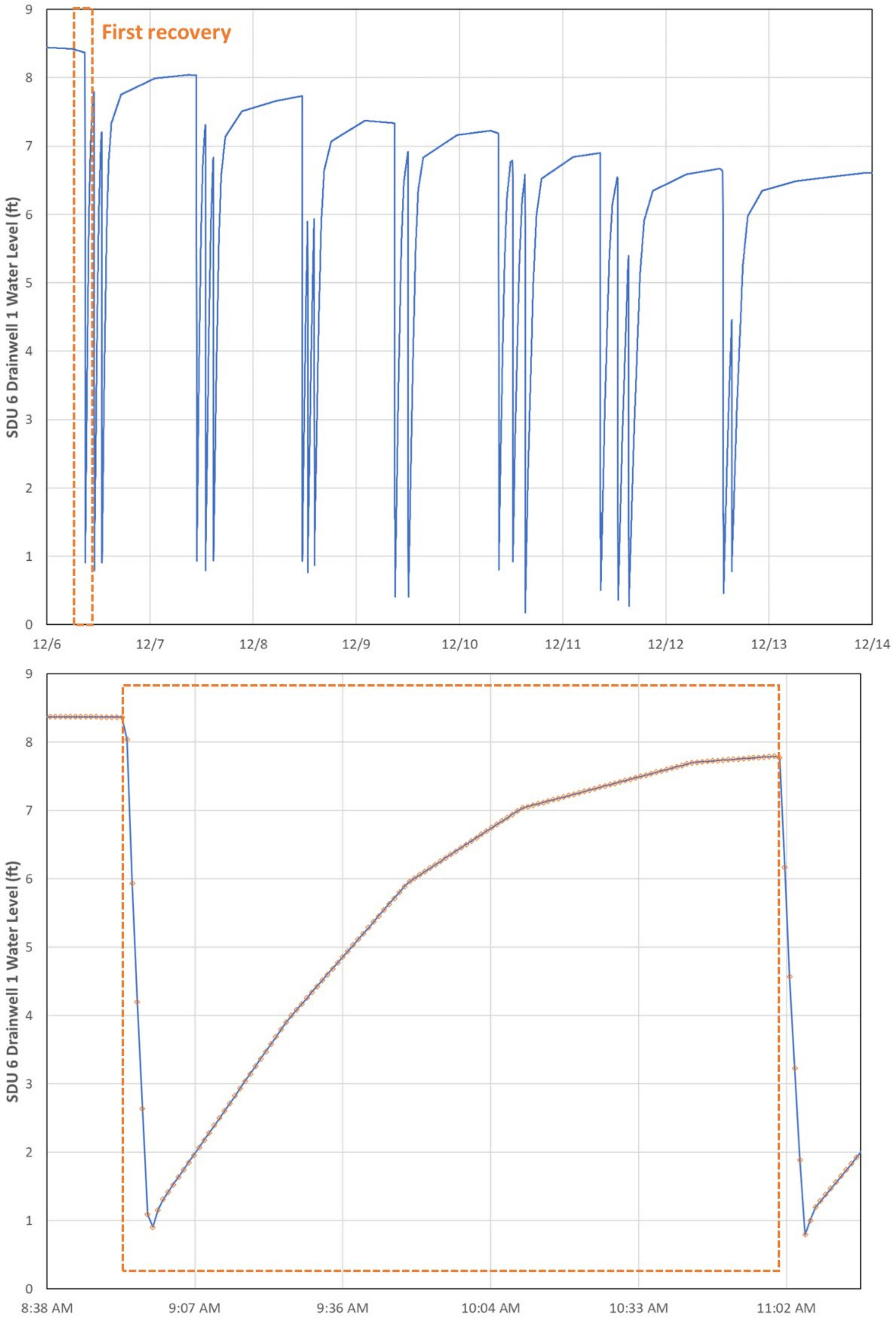

Figure 4-5: Bouwer-Rice Slug Test Interpretation.

Bouwer-Rice Slug Test Result: 1.5E-3 cm/s

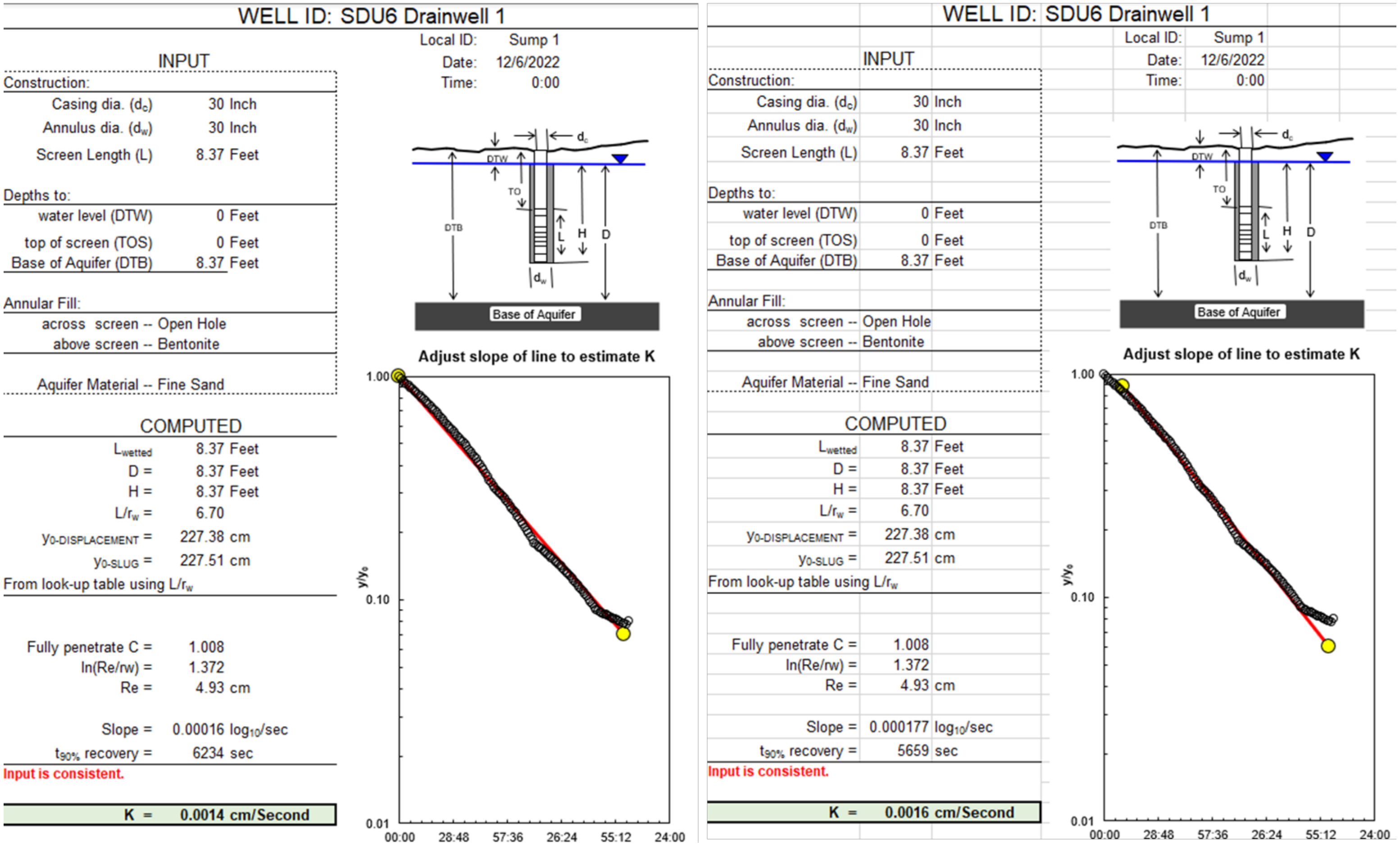

WELL ID: SDU6 Drainwell 1

Local ID: Sump 1
Date: 12/6/2022
Time: 0:00

INPUT

Construction:
Casing dia. (d_c) 30 Inch
Annulus dia. (d_w) 30 Inch
Screen Length (L) 8.37 Feet

Depths to:
water level (DTW) 0 Feet
top of screen (TOS) 0 Feet
Base of Aquifer (DTB) 8.37 Feet

Annular Fill:
across screen -- Open Hole
above screen -- Bentonite

Aquifer Material -- Fine Sand

COMPUTED
L_{wetted} 8.37 Feet
D = 8.37 Feet
H = 8.37 Feet
L/r_w = 6.70
$y_{0\text{-DISPLACEMENT}}$ = 227.38 cm
$y_{0\text{-SLUG}}$ = 227.51 cm
From look-up table using L/r_w

Fully penetrate C = 1.008
ln(Re/rw) = 1.372
Re = 4.93 cm

Slope = 0.00016 $\log_{10}$/sec
$t_{90\%}$ recovery = 6234 sec

Input is consistent.

K = 0.0014 cm/Second

Adjust slope of line to estimate K

WELL ID: SDU6 Drainwell 1

Local ID: Sump 1
Date: 12/6/2022
Time: 0:00

INPUT

Construction:
Casing dia. (d_c) 30 Inch
Annulus dia. (d_w) 30 Inch
Screen Length (L) 8.37 Feet

Depths to:
water level (DTW) 0 Feet
top of screen (TOS) 0 Feet
Base of Aquifer (DTB) 8.37 Feet

Annular Fill:
across screen -- Open Hole
above screen -- Bentonite

Aquifer Material -- Fine Sand

COMPUTED
L_{wetted} 8.37 Feet
D = 8.37 Feet
H = 8.37 Feet
L/r_w = 6.70
$y_{0\text{-DISPLACEMENT}}$ = 227.38 cm
$y_{0\text{-SLUG}}$ = 227.51 cm
From look-up table using L/r_w

Fully penetrate C = 1.008
ln(Re/rw) = 1.372
Re = 4.93 cm

Slope = 0.000177 $\log_{10}$/sec
$t_{90\%}$ recovery = 5659 sec

Input is consistent.

K = 0.0016 cm/Second

Adjust slope of line to estimate K

Figure 4-6: Cooper-Greene Slug Test Interpretation.

Cooper-Greene Slug Test Result: 5.6E-3 cm/s

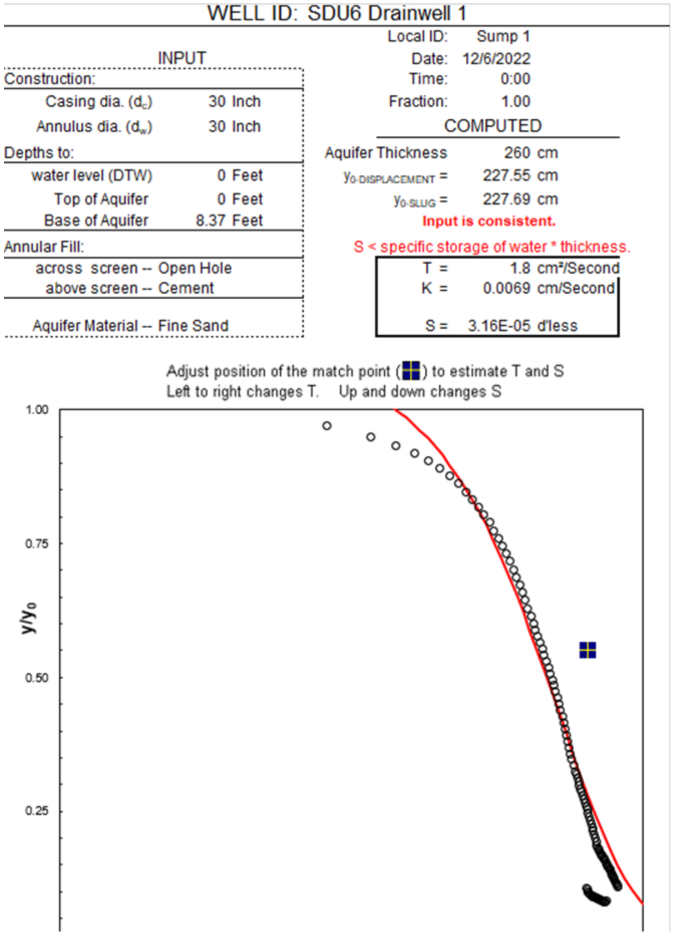

WELL ID: SDU6 Drainwell 1

Local ID: Sump 1
Date: 12/6/2022
Time: 0:00
Fraction: 1.00

INPUT

Construction:
Casing dia. (d_c) 30 Inch
Annulus dia. (d_w) 30 Inch

Depths to:
water level (DTW) 0 Feet
Top of Aquifer 0 Feet
Base of Aquifer 8.37 Feet

Annular Fill:
across screen -- Open Hole
above screen -- Cement

Aquifer Material -- Fine Sand

COMPUTED

Aquifer Thickness 260 cm
$y_{0\text{-DISPLACEMENT}}$ = 227.55 cm
$y_{0\text{-SLUG}}$ = 227.69 cm
Input is consistent.

S < specific storage of water * thickness.

T = 1.8 cm²/Second
K = 0.0069 cm/Second
S = 3.16E-05 d'less

Adjust position of the match point (▦) to estimate T and S
Left to right changes T. Up and down changes S

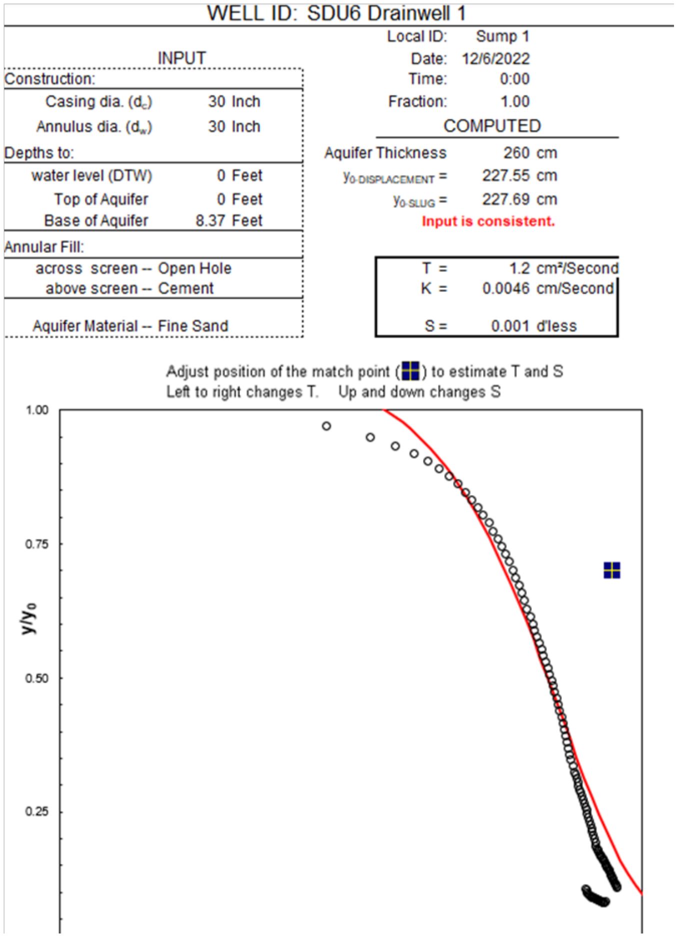

WELL ID: SDU6 Drainwell 1

Local ID: Sump 1
Date: 12/6/2022
Time: 0:00
Fraction: 1.00

INPUT

Construction:
Casing dia. (d_c) 30 Inch
Annulus dia. (d_w) 30 Inch

Depths to:
water level (DTW) 0 Feet
Top of Aquifer 0 Feet
Base of Aquifer 8.37 Feet

Annular Fill:
across screen -- Open Hole
above screen -- Cement

Aquifer Material -- Fine Sand

COMPUTED

Aquifer Thickness 260 cm
$y_{0\text{-DISPLACEMENT}}$ = 227.55 cm
$y_{0\text{-SLUG}}$ = 227.69 cm
Input is consistent.

T = 1.2 cm²/Second
K = 0.0046 cm/Second
S = 0.001 d'less

Adjust position of the match point (▦) to estimate T and S
Left to right changes T. Up and down changes S

4.2 East Sump leakage

As stated earlier, leakage to the SDU 6 East Sump is hypothesized to be the cause of gradual well drawdown before and after Drainwell 1 pumping in early December 2022. However, imbibition due to a non-equilibrium saturation state and/or ongoing (albeit slow) hydration reactions cannot be completely discounted.

Proceeding with a presumption of sump leakage, the leak rate is postulated to be proportional to the water level in SDU 6. Then leakage is a first-order process such that

$$h = h_0 exp(-\kappa t) \tag{61}$$

and

$$V = V_0 exp(-\kappa t) \tag{62}$$

where κ = first-order rate constant [1/T] (not to be confused in this context with intrinsic permeability), h = water level [L], V = remaining drain volume [L^3], and the subscript "0" denotes initial conditions. If leakage is not the physical cause underlying long-term drawdown, then an exponential decay process may nonetheless approximately capture the SDU 6 observations. Figure 4-7 and Figure 4-8 provide estimates of the first-order rate constant κ before and after Drainwell 1 pumping, respectively, using Equation (61). The rates are similar and the average giving more weight to the longer second period is approximately κ = 3.0E-03 day^{-1}.

Figure 4-9 shows an upper bound for the volume pumped from the East Sump based on monthly facility status report "Saltstone Combined PI 6-1-23.pdf". See Section 3.2 of SRR-CWDA-2023-00032 for further discussion. A maximum 9411 gallons leaked between 11/15/2022 and 4/15/2023, which far exceeds the volume within the 8 drainwells for the subject drawdown. Minimal pumping of the East Sump occurred over the last 6 weeks (per Figure 4-9) due to facility inactivity, yet the water levels in the 8 drainwells continued to decline. Whether leakage beyond the East Sump into the HDPE containment apron occurred during this period, as implied by Equation (61), is unclear. Another source of uncertainty is that water captured by the East Sump was returned to the disposal unit. The returned water is assumed to have pooled on the grout surface near the wall and, therefore is not immediately available to replenish the reservoir of water V in Equation (62) leaking from SDU 6. Despite uncertainties Equation (61) is carried forward for lack of a better alternative.

From Equation (62), the leak rate is

$$Q = \frac{dV}{dt} = -\kappa V_0 exp(-\kappa t) \tag{63}$$

V_0 = 25,700 gallons produces a leakage volume of 9411 gallons over 152 days (11/15/2022 to 4/15/2023).

Figure 4-7: Drawdown before Drainwell 1 pumping.

κ = 3.4e-3 day^{-1}

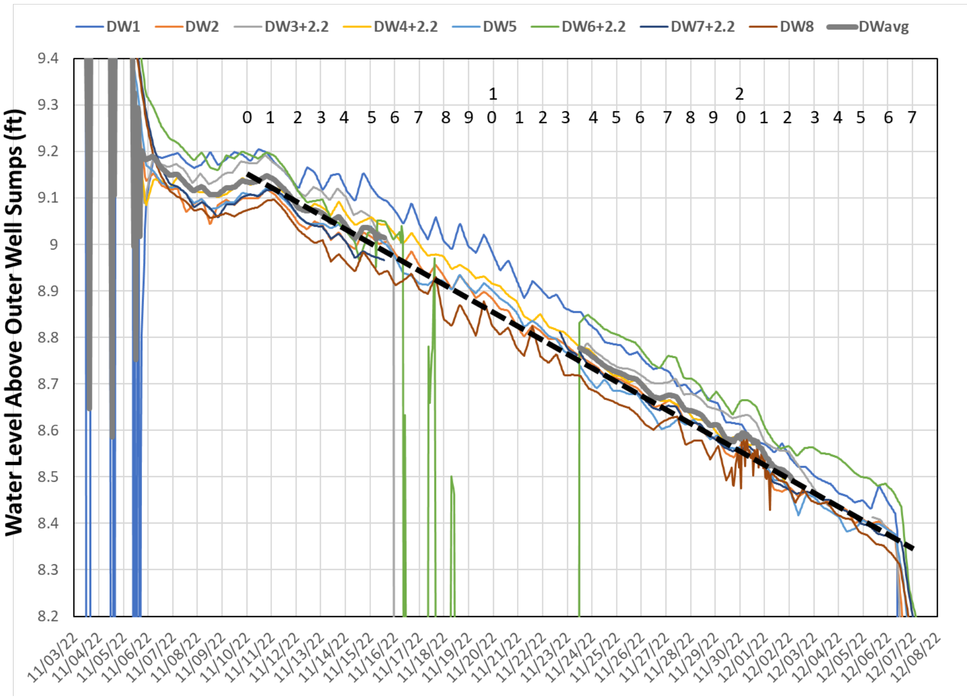

Figure 4-8: Drawdown after Drainwell 1 pumping.

κ = 2.9e-3 day^{-1}

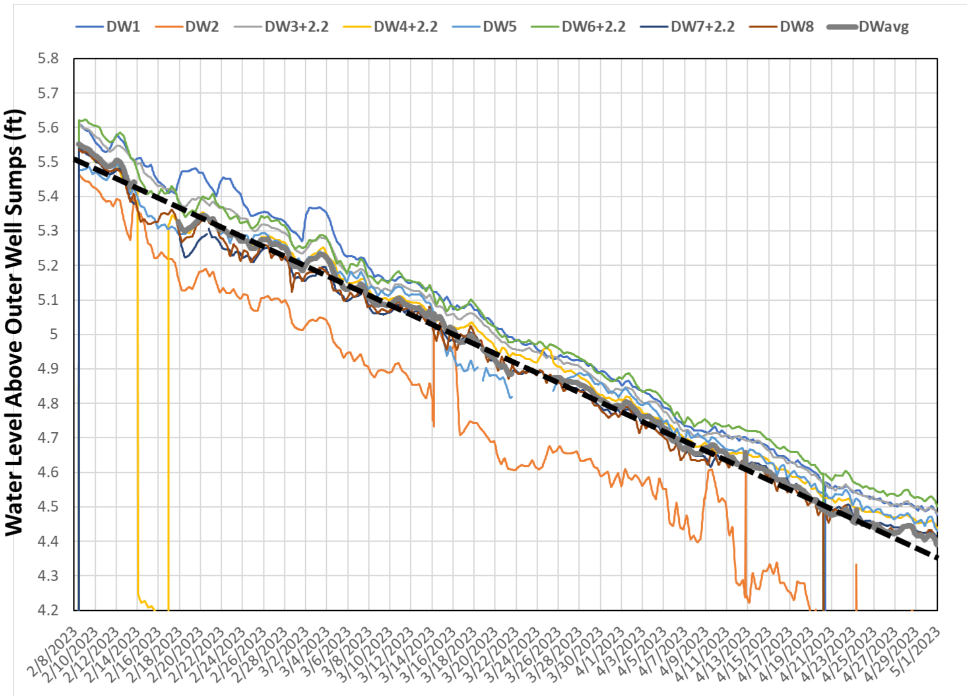

Figure 4-9: Upper bound estimate for volume pumped from the East Sump.

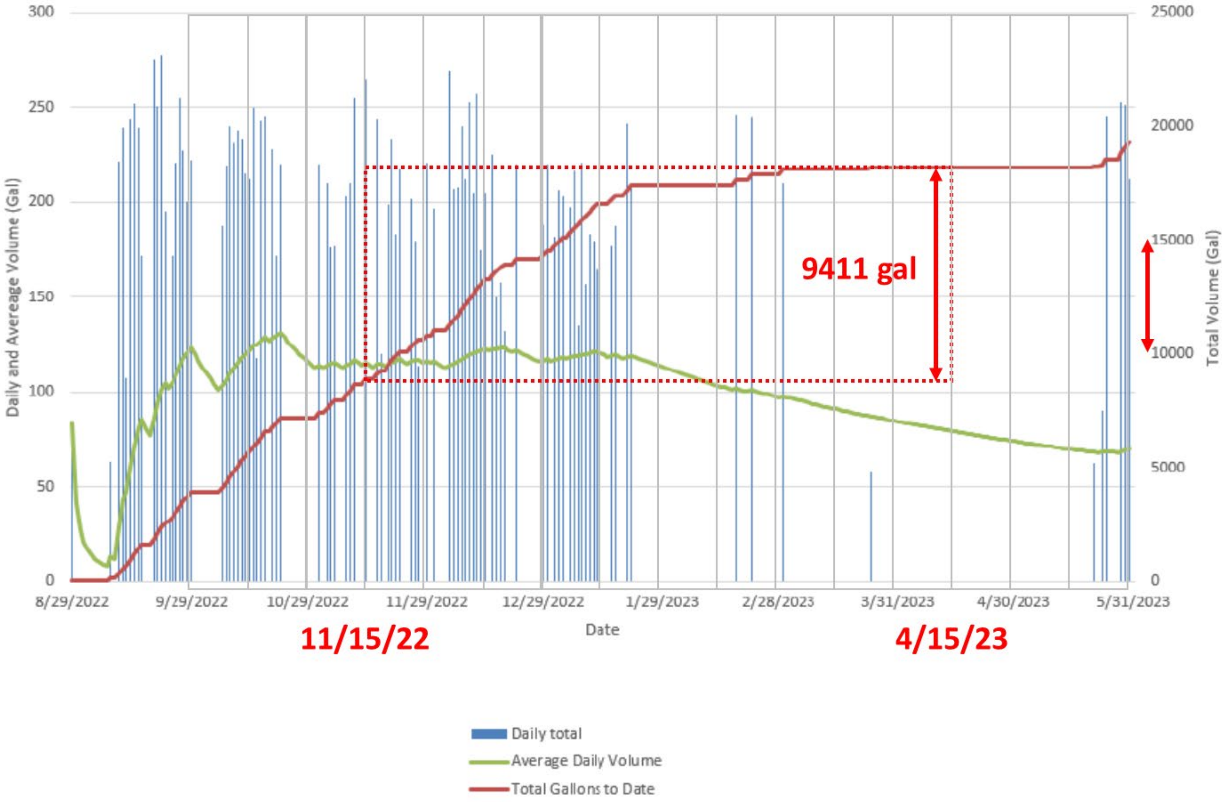

[base image from facility report “Saltstone Combined PI 6-1-23.pdf”]

5.0 2020 SDF PA Conceptual Model

The 2020 Saltstone Disposal Facility Performance Assessment (SRR-CWDA-2019-00001) assumes saltstone grout within SDU 6 to be a uniform material in intimate contact with the concrete containment structure. SDF PA Compliance Case modeling assumes a saltstone saturated hydraulic conductivity of 5.0E-12 m/s (5.0E-10 cm/s) per Table 3-1. Based on an estimated specific storage coefficient of 3.34E-03 m^{-1}, saltstone under this conceptual model has a hydraulic diffusivity on the order of 1.0E-09 m^2/s. As shown in Table 3-2, this results in timescales that are far too long to explain the hydraulic behavior observed in SDU 6. Instead Table 4-1 indicates an effective horizontal hydraulic conductivity (Section 2.15) of 3.E-03 cm/s is required to have hydraulic communication between drainwells within a day as observed. Similarly, slug test interpretations of the first Drainwell 1 recovery on December 6, 2022 also indicate a saturated hydraulic conductivity around 3.E-03 cm/s is required to achieve single-well recovery within hours (Figure 4-5, Figure 4-6).

The volume of water within the eight 30-in diameter drainwells for the 67 cm (26 in) drawdown between 12/6/2022 and 12/25/2022 is 646 gallons (Table 5-1) compared to a pumped volume of 5188 gallons (Figure 4-2). Therefore, approximately 90% of the drainwater came from outside the well casings, presumably from saltstone grout, unless fractures and/or macro-voids within the grout are identified. Table 3-7 indicates saltstone will be fully saturated or else moving toward that equilibrium state under SDU 6 exposure conditions. Therefore, desaturation of saltstone is not likely to be the source of drainwater. Instead, compression of saltstone is a likely source of drainwater, as shown in Table 5-2. Using the specific storage coefficient of 3.34E-03 m^{-1} from Table 3-1 estimated from measurements of Young's modulus, the estimated drain volume is 24,263 gallons. Working in the other direction, a specific storage coefficient of 6.3E-04 m^{-1} matches the observed drain volume. Note that the similar calculation in Table 4-1 does not consider that some drainwater originated from inside drainwell casings.

In summary, while saltstone compressibility could easily explain the volume of water drained from saltstone in December 2022, Drainwell 1 recovery within hours and hydraulic communication between drainwells within a day is inconsistent with the 2020 SDF PA conceptual model, specifically low K_{sat} in Table 3-1. In the next section various alternative material properties and conceptual models are tested against SDU 6 data using a PFLOTRAN numerical model.

Table 5-1: Water volume within drainwell casings for a 67 cm drawdown.

Parameter	Value	Units	Comments
Drainwell diameter	30	in	
	76.2	cm	
Area	4560	cm^2	
Drawdown	67	cm	12/6-25/2022
Drain volume per well	3.06E+05	cm3	
	80.7	gal	
Number of wells	8		Drainwell 1-8
Total volume	646	gal	

Table 5-2: Estimated drainwater from saltstone compression for a 67 cm drawdown.

	Specific storage coefficient			
Parameter	**Table 3-1**	**Calibrated**	**Units**	**Comments**
SDU 6 diameter	375	375	ft	
	114.3	114.3	m	
Area	10261	10261	m^2	
Grout level, Δz	4.0	4.0	m	December 2022
Grout volume	4.10E+04	4.10E+04	m^3	
Specific storage coefficient, S_s	3.34E-03 1.02E-03	6.25E-04 1.91E-04	1/m 1/ft	Table 3-1 or calibrated
Storativity, $S_s\Delta z$	1.34E-02	2.50E-03	-	
Gravitational acceleration, g	9.81	9.81	m/s^2	
Density of water, ρ	998	998	kg/m^3	
Porosity, n	0.656	0.656	-	
PFLOTRAN compressibility, C_0	5.20E-07	9.74E-08	1/Pa	
Drawdown	67	67	cm	12/6-25/2022
	0.67	0.67	m	
Estimated drain volume	9.18E+01 24263	1.72E+01 4542	m^3 gal	from matrix compression

6.0 Conceptual Model Testing

Several alternatives to the 2020 SDF PA conceptual model are considered in this section and tested against SDU 6 observations using a PFLOTRAN numerical model. The alternative models involve some combination of different material properties and/or different material zone configurations.

Quantitative drawdown targets for numerical testing are shown in Figure 6-1 and Figure 6-2. Figure 6-1 omits drawdowns in Drainwell 1 (DW1) during pumping to avoid clutter, while Figure 6-2 shows these drawdowns in December 2022. Drawdown markers are shown in centimeters for convenient comparison to simulation output in metric units.

Figure 6-1: Target drawdowns for 11/15/2022 to 4/15/2023 (cm).

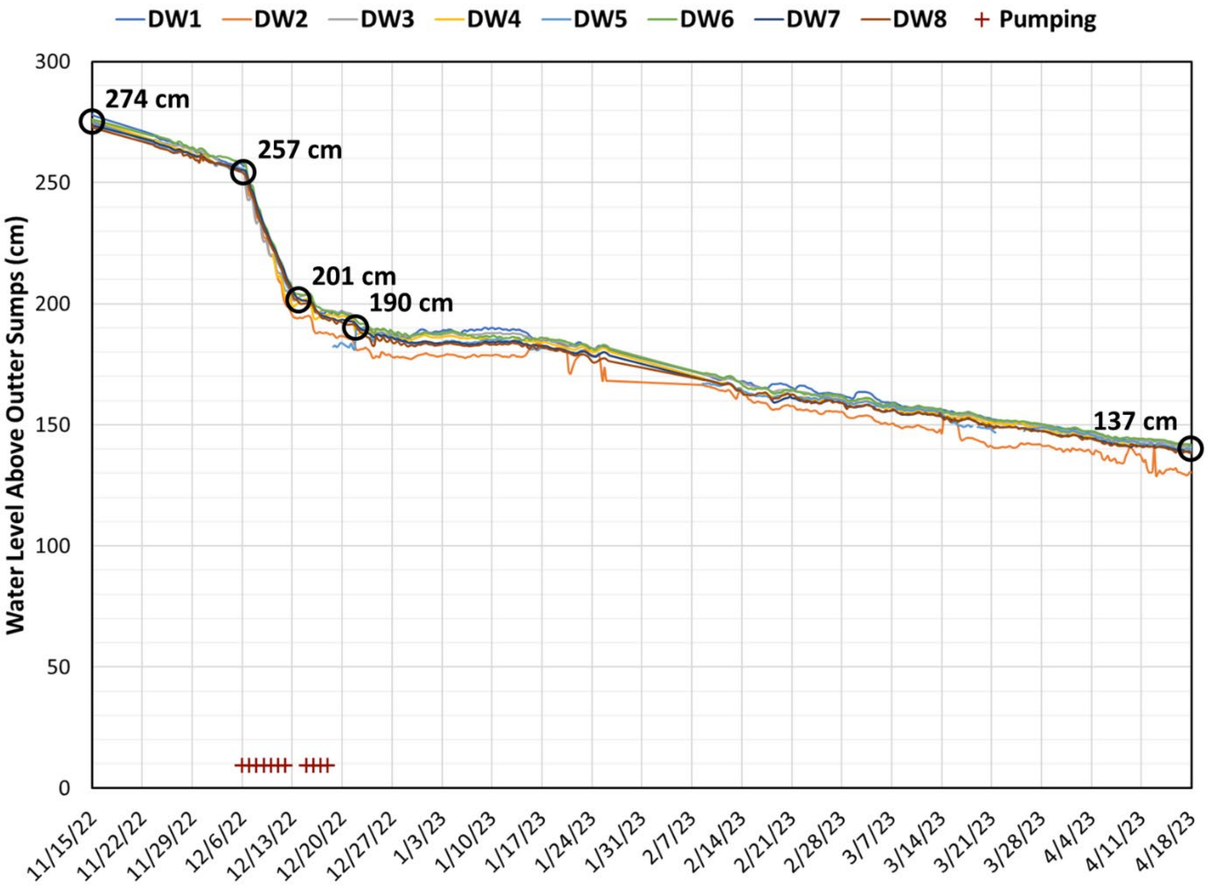

Figure 6-2: Target drawdowns for 12/6/2022 to 12/25/2022 (cm).

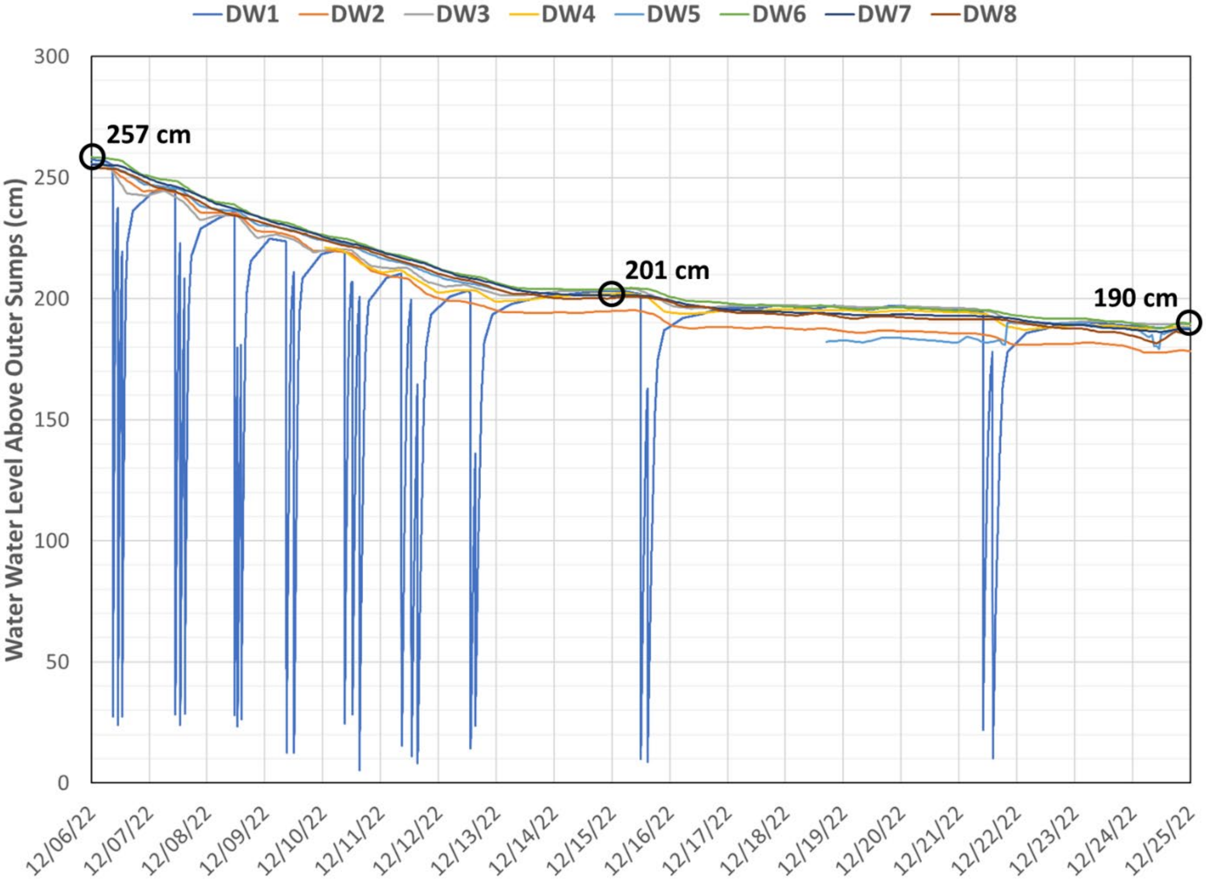

6.1 PFLOTRAN numerical model

PFLOTRAN is an open source, state-of-the-art, subsurface flow and reactive transport code (https://www.pflotran.org/) and a suitable computational tool for conceptual model testing. Geometric abstraction of the SDU 6 disposal unit is used in this study to greatly simplify grid construction without compromising insights gained from numerical modeling. Specifically, the cylindrical SDU 6 footprint is approximated by a square of the same area, and the 1.5% floor slope is ignored.

Table 6-1 defines the selected grid dimensions and resolution, and Figure 6-3 through Figure 6-6 provide illustrations. Three vertical layers are defined and may be assigned different material properties depending on the modeling case. Their thicknesses from bottom up are 0.1, 0.6, and 3.3 meters for a total grout thickness of 4.0 meters. The grid size is 64 by 64 by 30 grid cells for a total of 122,880 cells. PFLOTRAN is capable of massively parallel computations, but 2 CPUs per simulation were found optimal for the selected grid.

The eight drainwells are represented by a column of grid cells with the same cross-sectional area (Figure 6-6). Wells occupy 8 of 9 locations associated with a 3x3 grid (one corner location is unused). Drainwell 1 is represented by the left-middle location. Drawdowns at the center (middle-middle) and right-middle locations are plotted alongside Drainwell 1 results. The former represents drainwell behavior near the tank center and the latter the well at the wall opposite from Drainwell 1. Wells are assigned a porosity of 1.0, a low air-entry pressure, and high conductivity.

Although the pore solution of saltstone has a considerable concentration of dissolved salts (5.1 mol/L; about 7.3 times saltier than seawater), the properties of pure water are assumed in numerical modeling nonetheless. This assumption does not affect the K_{sat} values inferred from modeling, but K_{sat} in plain water would differ per Equation (11).

Table 6-2 summarizes the drainage volume, leakage volume, and drawdown information used in numerical modeling. The drainage and leakage volumes were imposed on each PFLOTRAN numerical model as boundary conditions and material properties (K_{sat}, C_0, and/or α) were manually calibrated to the drawdown data (drainwell water-level transients). Table 6-3 summarizes the conceptual model test cases considered herein.

Table 6-1: Grid geometry and resolution.

Parameter	**Value**	**Units**	**Comments**	**Grid resolution**			
Horizontal grid				**n**	**dxy**	**n**	**dz**
Tank diameter	375	ft		1	24.194	1	0.1
Equivalent square side	332.34	ft		2	26.977	2	0.1
	101.3	m		3	30.081	3	0.1
	100	m	as modeled	4	33.542	4	0.1
Well diameter	30	in		5	37.401	5	0.1
Equivalent square side	26.587	in		6	41.704	6	0.1
	67.53	cm		7	46.502	7	0.1
	0.6753	m		8	51.852	8	0.1
	0.6753	m	as modeled	9	57.818	9	0.1031
Number of wells	3		in x and y	10	64.47	10	0.1064
Wall gap	60	cm		11	71.887	11	0.1097
	0.6	m		12	80.158	12	0.1132
Number of wall gaps	2			13	89.38	13	0.1167
Cumulative length	3.2259	m		14	99.664	14	0.1204
Remaining length	96.774	m		15	111.13	15	0.1242
Number of grid subsections	4			16	. . .	16	0.1281
Subsection length	24.194	m				17	0.1321
Initial cell size	0.6753	m				18	0.1362
Growth factor	1.1151					19	0.1405
Vertical grid						20	0.1449
Overall						21	0.1495
Thickness	13.1	ft				22	0.1542
	3.9929	m				23	0.159
	4	m	as modeled			24	0.164
Number of cells	30					25	0.1691
Layer 1						26	0.1745
Thickness	0.1	m				27	0.1799
Number of cells	1					28	0.1856
Cell size	0.1	m				29	0.1914
Layer 2						30	0.1974
Thickness	0.6	m		**Grid cells/elements**			
Number of cells	6				iElements	nex	64
Cell size	0.1	m				ney	64
Layer 3						nez	30
Thickness	3.3	m				ne	122880
Number of cells	23						
Initial cell size	0.1	m					

Figure 6-3: PFLOTRAN grid: top perspective.

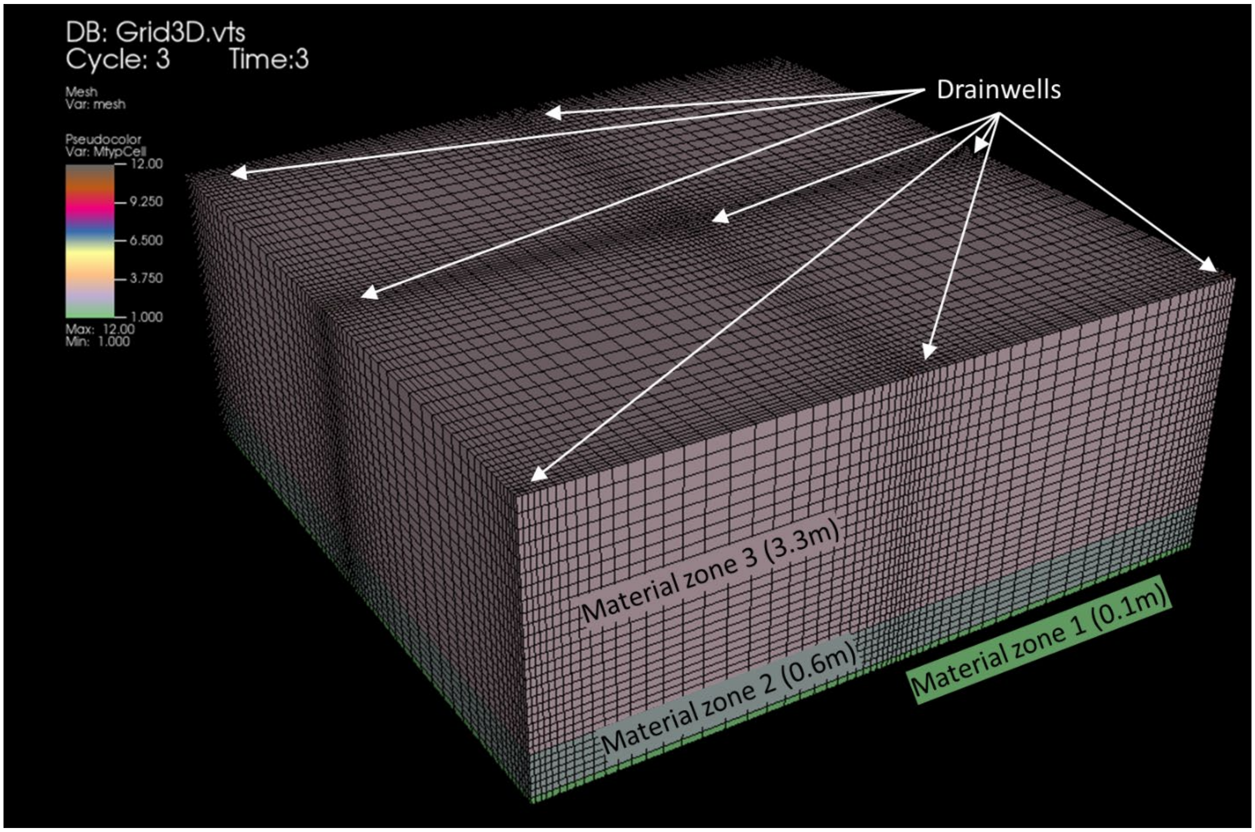

Figure 6-4: PFLOTRAN grid: bottom perspective.

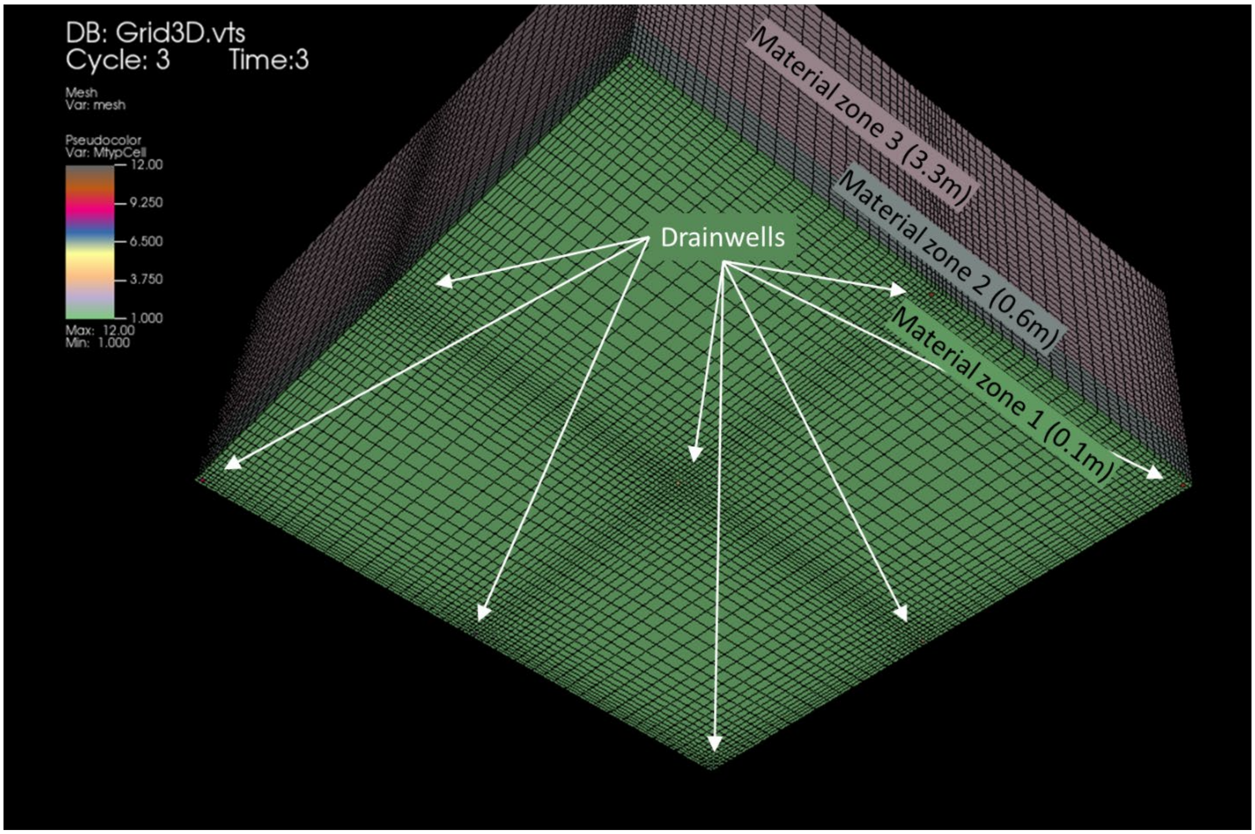

Figure 6-5: PFLOTRAN grid: material layers detail.

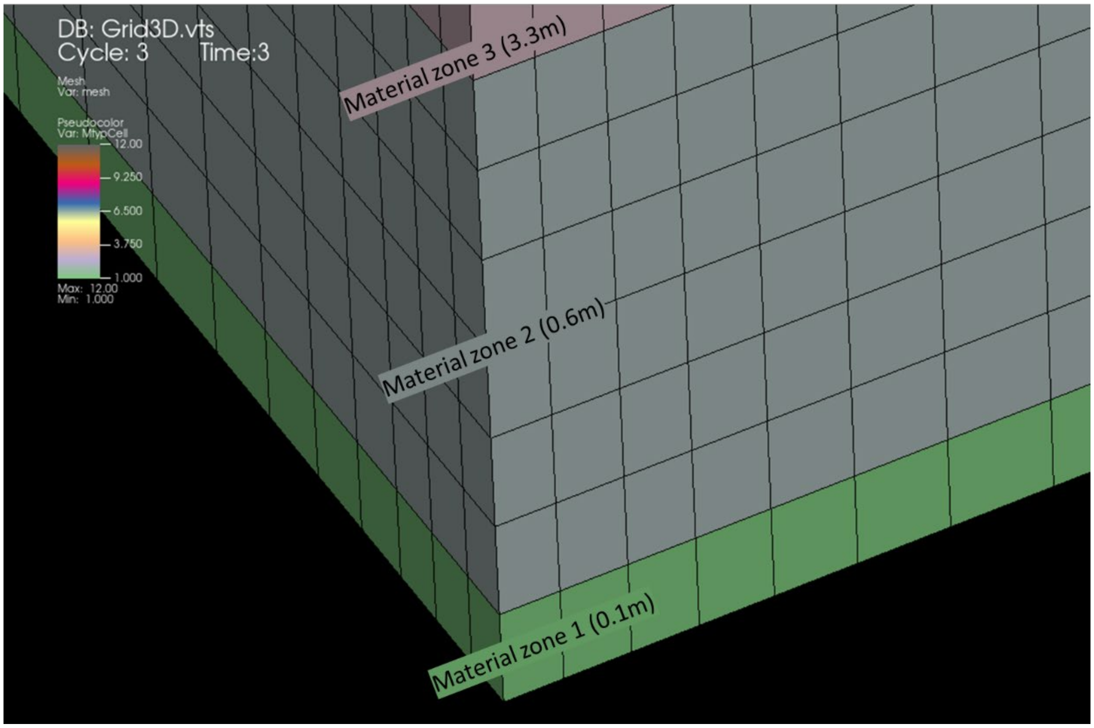

Figure 6-6: PFLOTRAN grid: drainwell locations.

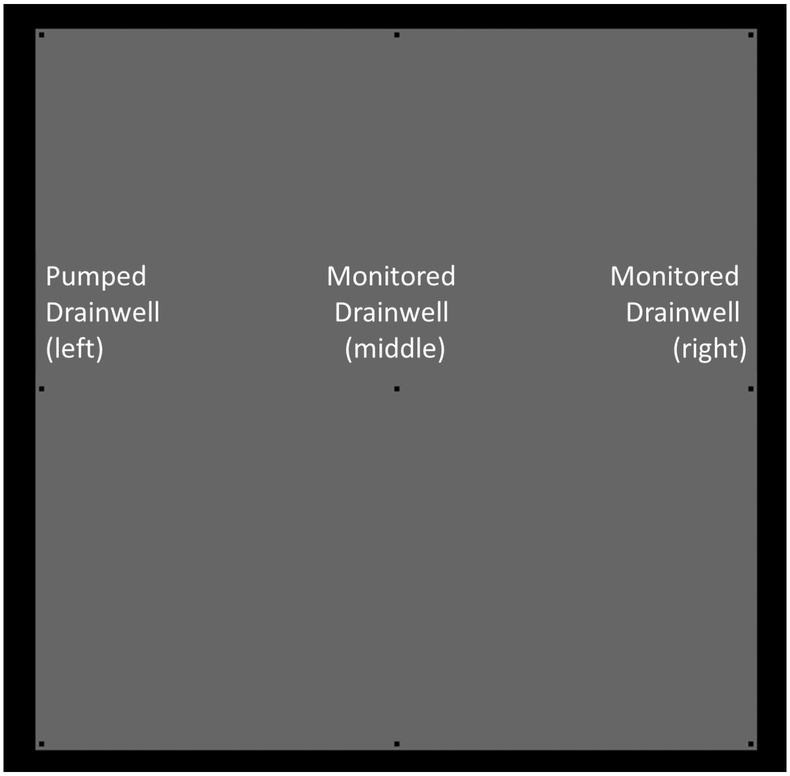

Table 6-2: Drainage and leakage volumes and drainwell drawdowns from SDU 6 data.

Parameter	Nov22-May23	12/6-13/22	Units	Comments
Initial water level	9.0 274	8.44 257	ft cm	11/15/2022
Final water level	4.5 137	6.6 201	ft cm	5/15/2023
Water level change, Δh	137	56	cm	
Pumping, Day 1-7	4351	4351	gal	Early Dec 2022
Pumping, Day 10-13	432	N/A	gal	Early Dec 2022
Pumping, Day 16	405	N/A	gal	Early Dec 2022
Drainwell pumping, total	5188	4351	gal	11/15/2022 thru 5/15/2023
East Sump leakage	9411	neglected	gal	11/15/2022 thru 5/15/2023
Total water loss	14599	4351	gal	11/15/2022 thru 5/15/2023
Number of drainwells	8	8		
Drainwell diameter	30	30	in	
Water loss from drainwell casings	5.00E+06 1322	2.05E+06 541	cm3 gal	
Water loss from grout	13277	3810	gal	Target for model calibration
First-order rate constant, κ	3.0E-03		1/day	Figure 4-7, Figure 4-8
Duration	152		day	11/15 /22 to 4/15/23
Initial volume, V_0	25700		gal	Calibrated to East Sump leakage

Table 6-3: Summary of conceptual model test cases.

Case	**0.5mm Floor Gap?**	K_{sat} **Lower 0.7m** (cm/s)	K_{sat} **Upper 3.3m** (cm/s)	C_0 **Lower 0.7m** (Pa^{-1})	C_0 **Upper 3.3m** (Pa^{-1})	**Comments**
A	No	3.0E-03	3.0E-03	α = 3.96E-04 cm^{-1}	α = 3.96E-04 cm^{-1}	Rejected because the very high K_{sat} is (1) inconsistent with measurements on cores drilled from SDU 2A and (2) would imply negligible cementation of the dry mix.
B	No	3.0E-03	3.0E-03	1.43E-07	1.43E-07	Rejected because the very high K_{sat} is inconsistent with measurements.
C	Yes	5.0E-06	5.0E-06	α = 3.96E-04 cm^{-1}	α = 3.96E-04 cm^{-1}	Rejected because the high K_{sat} is inconsistent with measurements and because saltstone is not saturated.
D	Yes	5.0E-06	5.0E-06	1.43E-07	1.43E-07	Rejected because the high K_{sat} is inconsistent with measurements.
E	Yes	1.0E-07	1.0E-07	5.2E-07	0.11E-07	Rejected because drawdown is significantly overpredicted and notable rebound is inconsistent with field data.
F	Yes	1.0E-07	1.0E-07	5.2E-07	0.63E-07	Rejected because notable rebound is inconsistent with field data.
G	Yes	5.0E-07	2.0E-09	7.0E-07	2.0E-07	Plausible.
H	Yes	5.0E-07	5.0E-10	7.0E-07	7.0E-07	Likely because data is most consistent with measurements and field observations.
I	Yes	5.0E-07	1.0E-08	6.6E-07	0.8E-07	Less plausible because C_0 differs more between layers and because the K_{sat} is based on the upper bound of measured values whereas most samples are measured with significantly lower values.

6.2 Uniform saltstone and intimate contact with floor

The 2020 SDF PA conceptual model assumes *uniform grout* that is in *intimate contact* with the SDU 6 floor. The latter means no separation gap exists between the floor and overlying saltstone. This conceptual model is retained in this subsection but alternative material properties are assigned to saltstone to better match SDU 6 observations as noted below. Two end-member cases are considered (Table 6-3).

Case A ignores matrix compression and assumes drainwater beyond that inside well casings (Table 6-2) comes from *desaturation* of saltstone. To achieve this result, the vGM α parameter is empirically increased to 3.96E-04 cm^{-1} to match the observed drainage and leakage volume for the November 2022 to April 2023 period (see Table 6-4 calculations). A slightly lower value is calculated for the December 2022 pumping period. As a point of reference, Leverett scaling using this empirical α suggests a corresponding K_{sat} around 10^{-7} cm/s.

Case B assumes full saturation such that drainwater comes only from *compression* of saltstone. The PFLOTRAN porosity compressibility coefficient C_0 is empirically defined to match the observed drain volume. The result based on the November 2022 to April 2023 period is C_0 = 1.43E-07 Pa^{-1} (Table 6-4). The value calculated for the December 2022 period is slightly lower.

Table 6-4 calculates empirical values for S_s accounting only for the water volume drained from grout. Hydraulic diffusion calculations, like those presented previously, indicate a required hydraulic conductivity value of 3.0E-03 cm/s and this value is assigned to grout for Case A and B.

Simulated drawdowns are shown in Figure 6-7 and Figure 6-8. The upper plots show the measured water levels in drainwells other than the pumped well, DW1, using thinner colored lines. Simulation results for the right well (Figure 6-6) are represented by the thick black line denoted with the modeling case ID. The lower plots show simulated results for the left, middle, and right drainwells (Figure 6-6). Field observations are omitted to avoid excessive clutter, but Figure 6-2 can be consulted for visual comparison to the model simulations.

Table 6-4: PFLOTRAN model input calculations.

	Desaturation only		**Compression only**						
Parameter	**Nov22-Apr23**	**Dec6-13**	**Nov22-Apr23**			**Dec6-13**			**Units**
Calculated α_{vG} and C_0	*Total*	*Total*	*Total*	*Lower*	*Upper*	*Total*	*Lower*	*Upper*	
Initial water level	274	257	274			257			cm
Final water level	137	201	137			201			cm
Water level change, Δh	137	56	137			56			cm
	1.37	0.56	1.37			0.56			m
	13428	5491	13428			5491			Pa
Water loss from grout	13277	3810	13277			3810			gal
Porosity, φ	0.656	0.656	0.656			0.656			
Compressibility, C_0	1.0E-20	1.0E-20	**1.43E-07**	**5.2E-07**	**6.3E-08**	**1.00E-07**	**5.2E-07**	**1.1E-08**	1/Pa
van Genuchten α_{vG}	**3.96E-04**	**3.67E-04**	1.0E-20			1.0E-20			1/cm
	4.042E-06	3.752E-06	1.021E-22			1.021E-22			1/Pa
van Genuchten n_{vG}	1.67131	1.67131	1.67131			1.67131			
van Genuchten m_{vG}	0.401667	0.401667	0.401667			0.401667			
Sat. water content, θ_s	0.58	0.58	0.58			0.58			
Residual water content, θ_r	0	0	0			0			
Residual saturation, S_r	0	0	0			0			
Side length	100	100	100			100			m
Saltstone height	4	4	4	0.7	3.3	4	0.7	3.3	m
	400	400	400			400			cm
	13.1	13.1	13.1			13.1			ft
Grout volume	40000	40000	40000			40000			m^3
	1.06E+07	1.06E+07	1.06E+07			1.06E+07			gal
Water loss due to compression	0	0	13276			3810			gal
Water loss due to desaturation	13277	3810	0			0			gal

Table 6-4 continued

Leverett scaling reference	*Total*	*Total*	*Total*	*Lower*	*Upper*	*Total*	*Lower*	*Upper*	
Reference K_{sat}	5.0E-10	5.0E-10	5.0E-10			5.0E-10			cm/s
Reference α_{vG}	2.254E-05	2.254E-05	2.254E-05			2.254E-05			1/cm
Assumed α_{vG}	3.957E-04	3.673E-04	1.000E-20			1.000E-20			1/cm
Estimated K_{sat}	**1.5E-07**	**1.3E-07**							cm/s
Hydraulic diffusion reference	*Total*	*Total*	*Total*	*Lower*	*Upper*	*Total*	*Lower*	*Upper*	
Volume drained from grout	50.26	14.42	50.26			14.42			m^3
Specific storage coefficient, S_s	9.16E-04	6.43E-04	9.16E-04			6.43E-04			1/m
	9.16E-06	6.43E-06	9.16E-06			6.43E-06			1/cm
Required timescale	18	18	18			18			hr
	64800	64800	64800			64800			s
Grout width	10130	10130	10130			10130			cm
Required K_{sat}	**3.6E-03**	**2.5E-03**	**3.6E-03**			**2.5E-03**			cm/s
Grout thickness	400	400	400			400			cm
Required K_{sat}	**5.7E-06**	**4.0E-06**	**5.7E-06**			**4.0E-06**			cm/s
Grout thickness	60	60	60			60			cm
Required K_{sat}	**1.3E-07**	**8.9E-08**	**1.3E-07**			**8.9E-08**			cm/s

Figure 6-7: Simulated drawdown for Case A.

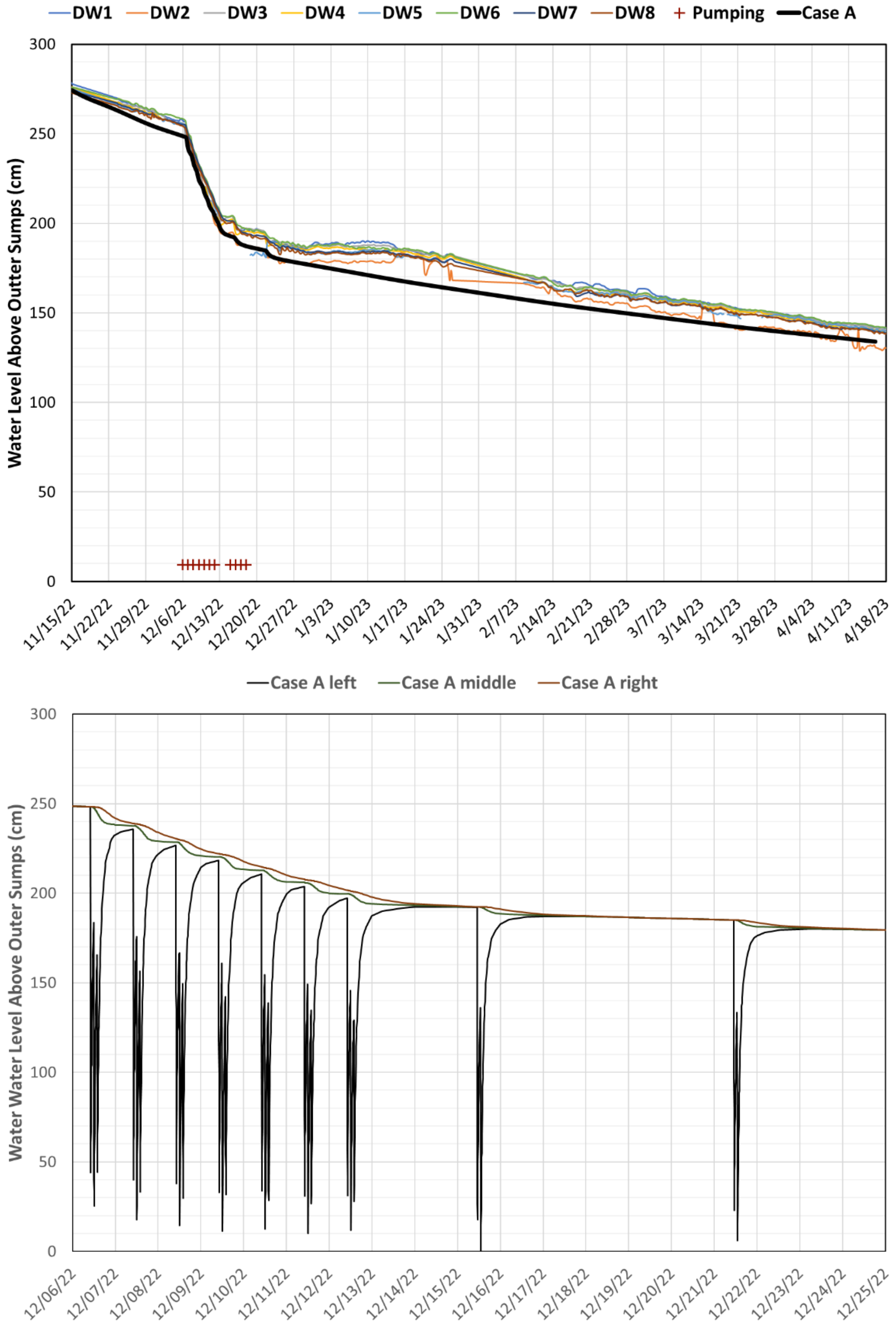

Figure 6-8: Simulated drawdown for Case B.

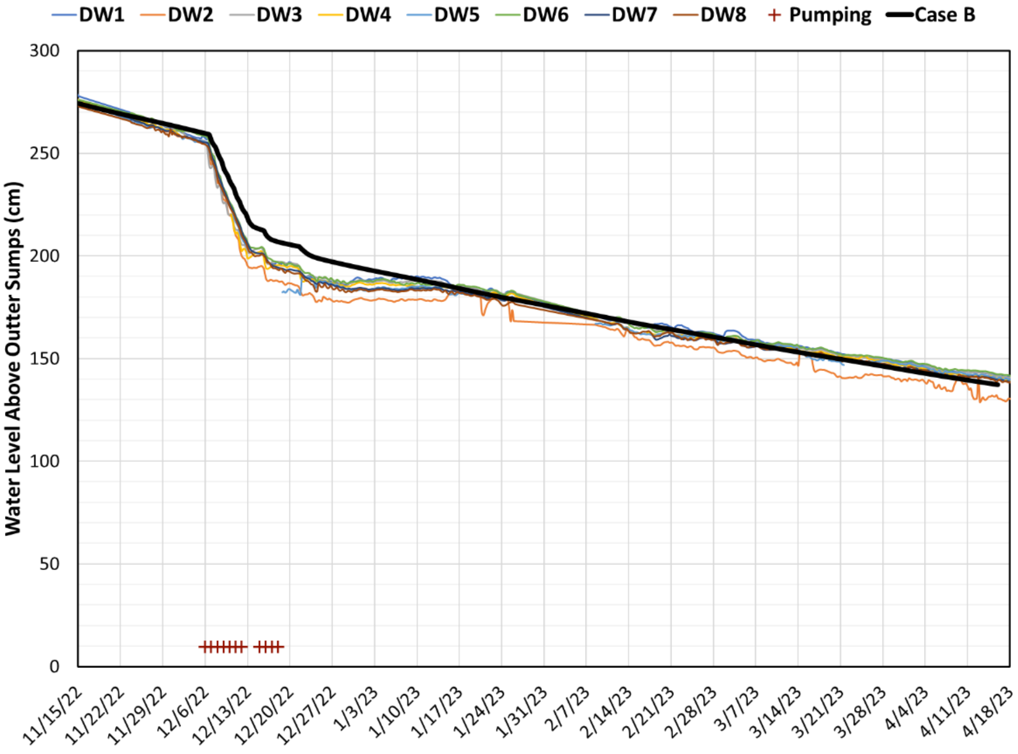

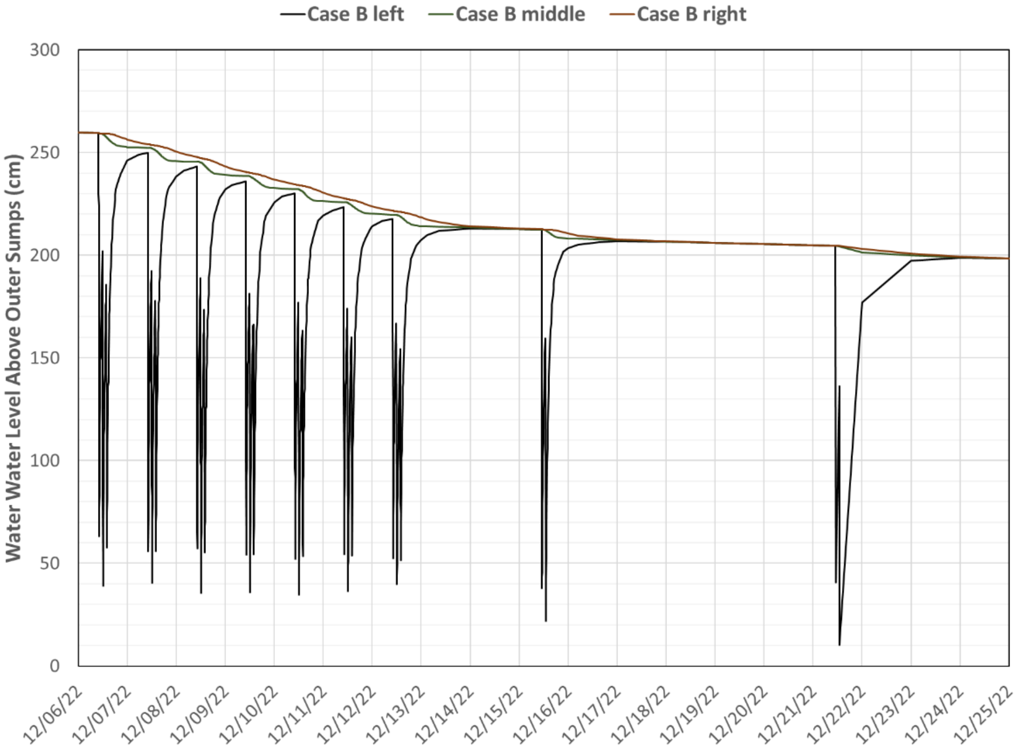

Case A slightly overpredicts drawdown on 4/15/2023 and could be refined by adjusting the vGM α parameter. However, overall drawdown would still exhibit other biases apparent in Figure 6-7. Early drawdown is overpredicted because less water is produced per unit drop in head due to the shape of the water retention curve (see Section 2.4 discussion). Conversely, Case B underpredicts early drawdown and could be refined by considering spatial heterogeneity.

Regardless, both cases are rejected because they rely on a horizontal hydraulic conductivity of 3.0E-03 cm/s for saltstone. This value is orders of magnitude higher than any measurement, including an SRNL study that considered the effects of thin pours and cold joints. That study indicates an upper bound of roughly 1.0E-7 cm/s (SRNL-STI-2012-00522). Table 6-5 estimates the hydraulic conductivity of the saltstone dry feed assuming no hydration reactions occur, such that saltstone is an uncemented granular material. The Hazen and Kozemy-Carman methods indicate K_{sat} around 1.0E-5 cm/s. Thus, K_{sat} = 3.0E-03 cm/s seems implausibly high.

A horizontal conductivity of 3.0E-03 cm/s is plausible for a fractured medium. However, this conceptual model is rejected because visual surveillance of SDU 6 does not indicate significant cracks in the saltstone that would result in higher hydraulic conductivity.

Table 6-5: Hydraulic conductivity estimate for saltstone dry feed.

Parameter	Slag	Fly Ash	Portland Cement	Weighted Average	Units	Comments
Proportion	45%	45%	10%			
Volume diameter, mean	8.95	42.65	23.45	25.6	µm	Ref. 1 Table 3-1
Volume diameter, median	7.29	29.85	19.75	18.7	µm	Ref. 1 Table 3-1
Number diameter, mean	0.68	0.68	0.54	0.66	µm	Ref. 1 Table 3-1
Number diameter, median	0.55	0.54	0.47	0.53	µm	Ref. 1 Table 3-1
Effective grain size, d_{10}	1.02	5.09	3.79		µm	Ref. 1 Figure 3-5, 7, 9 Batch 1
	1.28	4.78	4.89		µm	Ref. 1 Figure 3-5, 7, 9 Batch 2
	1.15	4.93	4.34	3.2	µm	Average
Hazen estimate						
Effective grain size, d_{10}				3.2E-03	mm	
Hydraulic conductivity, K				**1.0E-05**	**cm/s**	Ref. 2 Equation (8.47)
Kozeny-Carman estimate						
Density, ρ				998	kg/m^3	
Gravitational acceleration, g				9.81	m/s^2	
Viscosity, μ				0.001	Pa-s	
Porosity, n				0.4		Typical of sediments
d_m for Kozeny-Carman				3.2E-06	m	Chose d10
Hydraulic conductivity, K				9.7E-08	m/s	Ref. 2 Equation (8.50)
				9.7E-06	**cm/s**	~Same as Hazen estimate

Note: Ref. 1 = WSRC-TR-2006-00067; Ref. 2 = Freeze and Cherry (1979)

6.3 Uniform saltstone and floor gap

Because the SDU 6 drainwells are fully penetrating, the vertical distribution of K_{sat} is unknown and only *effective* (vertical average) hydraulic conductivity can be inferred (Section 2.15). SRMC-CWDA-2024-00045 hypothesizes a separation gap between saltstone grout and the floor liner, such that a fracture may participate in horizontal flow to drainwells; see Section 10 in SRMC-CWDA-2024-00045 for a full discussion. Such a feature would dramatically increase K_{eff} for the system.

Table 6-6 shows that an effective hydraulic conductivity of 3.0E-03 cm/s can be achieved with a 0.50 mm aperture between the floor liner and overlying grout. In PFLOTRAN modeling, the 0.1-meter-thick bottom grid layer can be repurposed to represent a 0.5-mm physical floor gap by assigning it a hydraulic conductivity of 0.1 cm/s.

Cases C and D resemble Cases A and B, respectively, but with a floor gap considered. With the horizontal fast-flow path, water need only flow downward through the 4.0-meter grout thickness before moving laterally to drainwells. As shown by the hydraulic diffusion calculation in Table 6-4, a grout conductivity of 5.0E-6 cm/s should provide adequate response time. Thus, Cases C and D assume uniform grout with this K_{sat} value.

Simulation results are shown in Figure 6-9 and Figure 6-10 and summarized in Table 6-3.

Case C and D drawdowns are similar to Cases A and B, respectively, despite the assigned K_{sat} value being three orders of magnitude lower. Both simulations could be refined with model calibration but still exhibit the inherent biases identified for Case A and Case B. Case C and D are rejected because K_{sat} = 5.0E-6 cm/s is still 50 times higher than the upper range of measurements reported in SRNL-STI-2012-00522. Case C (along with Case A) is also inconsistent with the expectation that saltstone will be 100% saturated (Section 3.2). Furthermore, adding vertical heterogeneity would not appreciably change drawdown behavior because water is draining from the top of saltstone in Case C. Therefore, desaturation is rejected as a source of drainwater in subsequent modeling cases.

Table 6-6: Fracture aperture calculation.

Parameter	Value	Units	Comments
Gravitational acceleration	9.81	m/s2	
Density of water	998	kg/m3	
Viscosity	0.0010	Pa-s	
Uniform grout			
Total thickness, B	4	m	
Effective K_{sat}	3.0E-05 3.0E-03	m/s cm/s	
Transmissivity, T	1.2E-04	m^2/s	$T = K_{sat}\ B$
Model fracture			
As modeled seam thickness, B	0.1	m	PFLOTRAN
As modeled seam K_{sat}	1.0E-03 0.1	m/s cm/s	PFLOTRAN
Transmissivity, T	1.0E-04	m^2/s	$T = K_{sat}\ B$
Physical fracture			
Equivalent fracture aperture b	4.97E-04 0.50 497.0 19.6	m mm µm mil	
Fracture K_{sat}	0.201 20.1	m/s cm/s	Equation (57)
Fracture transmissivity	1.00E-04	m2/s	$T = K_{sat}\ b$

Figure 6-9: Simulated drawdown for Case C.

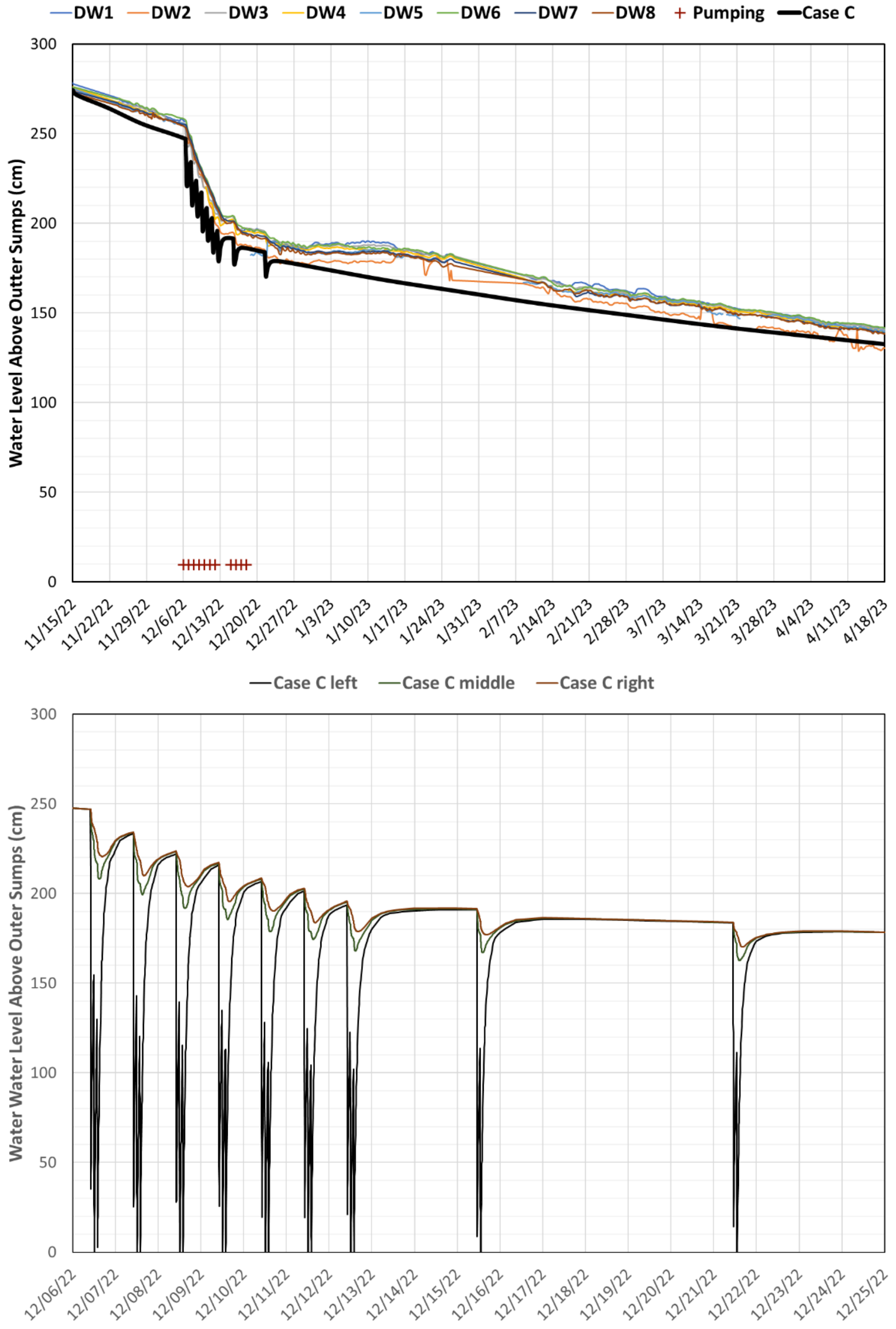

Figure 6-10: Simulated drawdown for Case D.

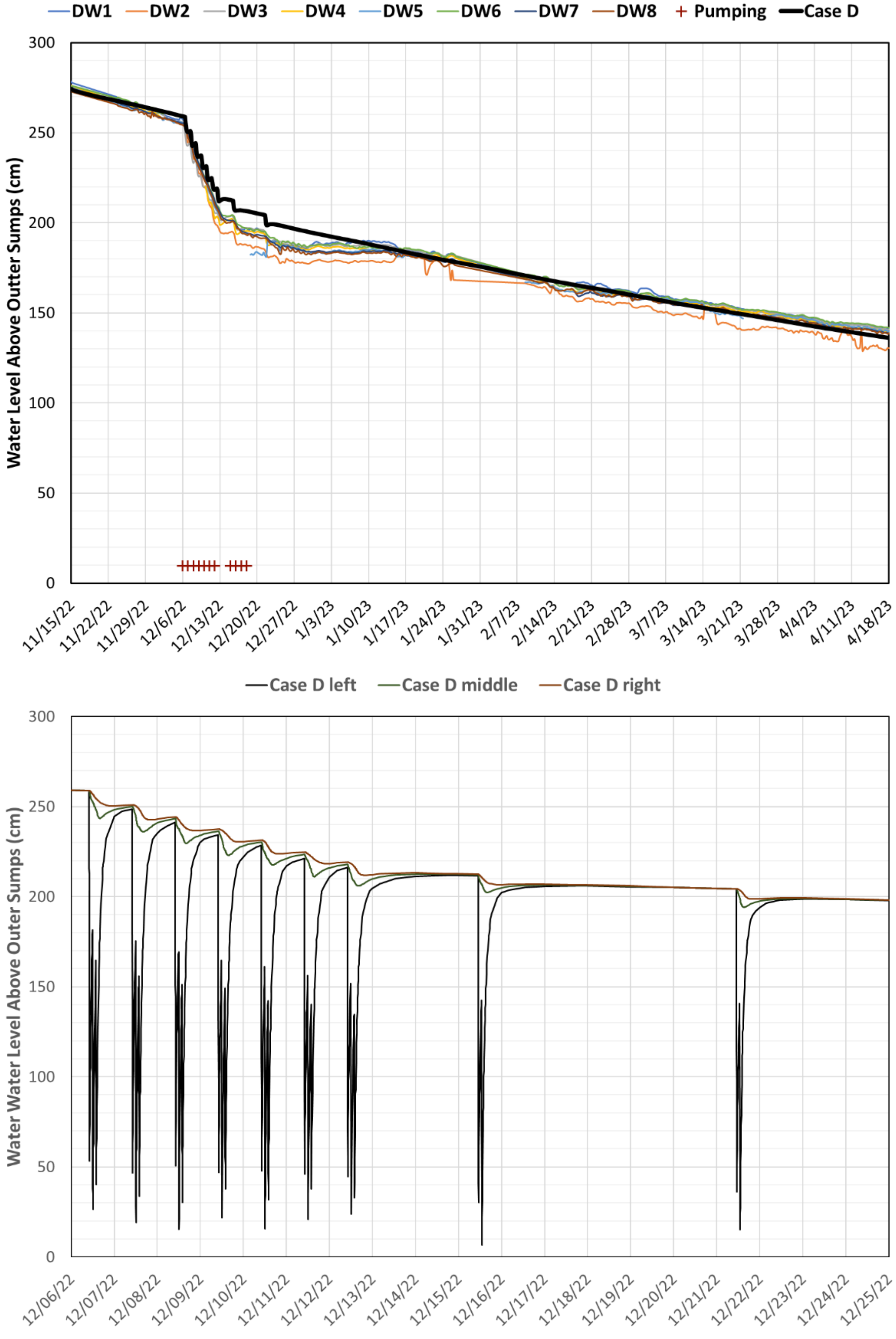

6.4 Two-layer specific storage coefficient + floor gap

The drawdowns shown in Figure 6-10 suggest a two-layer conceptual model where the faster responding lower grout layer has a higher compressibility C_0 than the upper layer further from the floor gap. A higher compressibility than assumed in Case D can be supported by the 5.2E-07 Pa^{-1} value in Table 3-1 computed from Young's modulus measurements, and/or a higher conductivity grout at the bottom of SDU 6 as hypothesized in SRMC-CWDA-2024-00045.

As shown by the hydraulic diffusion timescale calculation in Table 6-4, the 0.6-meter lower grout layer adjoining the floor gap will have an adequate response time with a K_{sat} around 1.0E-07 cm/s, 50x lower than assumed in Case D and aligning with the upper range of measurements from SRNL-STI-2012-00522.

Cases E and F assume a uniform grout conductivity of 1.0E-07 cm/s, and both cases assume C_0 = 5.2E-07 Pa^{-1} (Table 3-1) in the lower 0.7 meters (2.3 ft) of grout, as a starting point for subsequent calibration. Case E assumes C_0 = 1.1E-08 Pa^{-1} in the upper 3.3 m (11 ft), while Case F assumes 6.3E-08 Pa^{-1} (Table 6-4). Coupled with 5.2E-07 Pa^{-1} in the lower grout layer, these values are projected to match the drain volumes associated with December 6-13 and the overall period, respectively, for the observed drawdowns (calculation shown in Table 6-4).

Simulation results are shown in Figure 6-11 and Figure 6-12.

Case E significantly overpredicts overall drawdown while Case F produces much better agreement. Better agreement could be achieved with models by calibrating the C_0 parameter. However, both models exhibit a notable rebound in drawdown between December 14 and 25, 2022, that is not seen in the field data. This observation suggests a lower K_{sat} is needed in the upper layer.

Figure 6-11: Simulated drawdown for Case E.

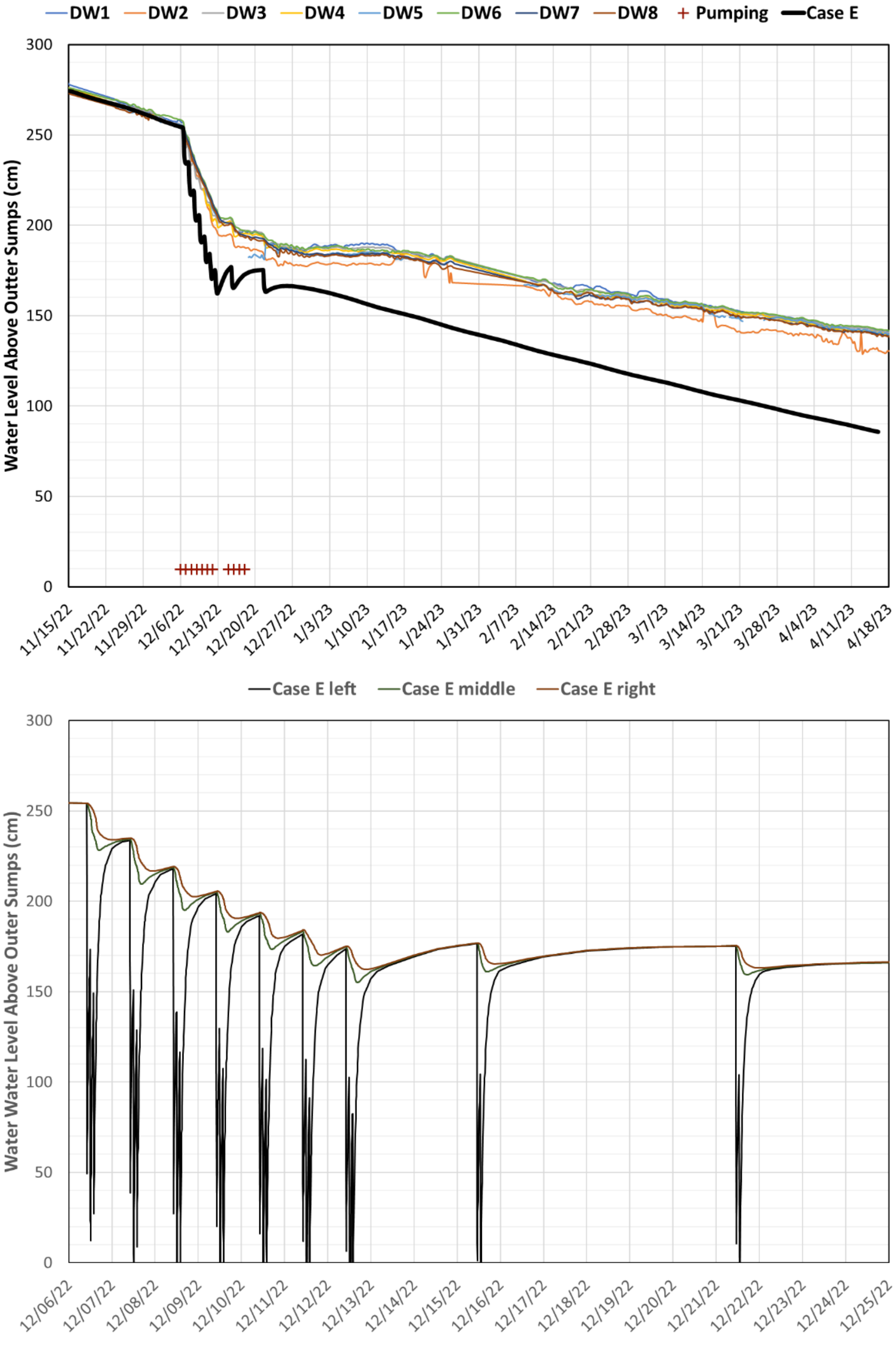

Figure 6-12: Simulated drawdown for Case F.

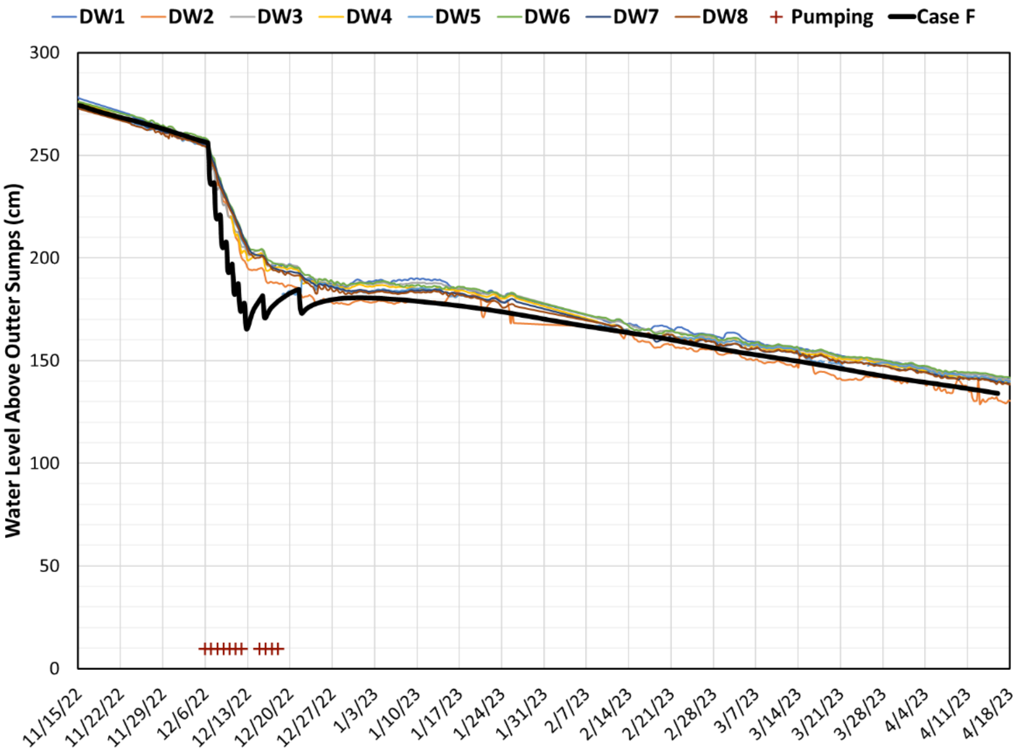

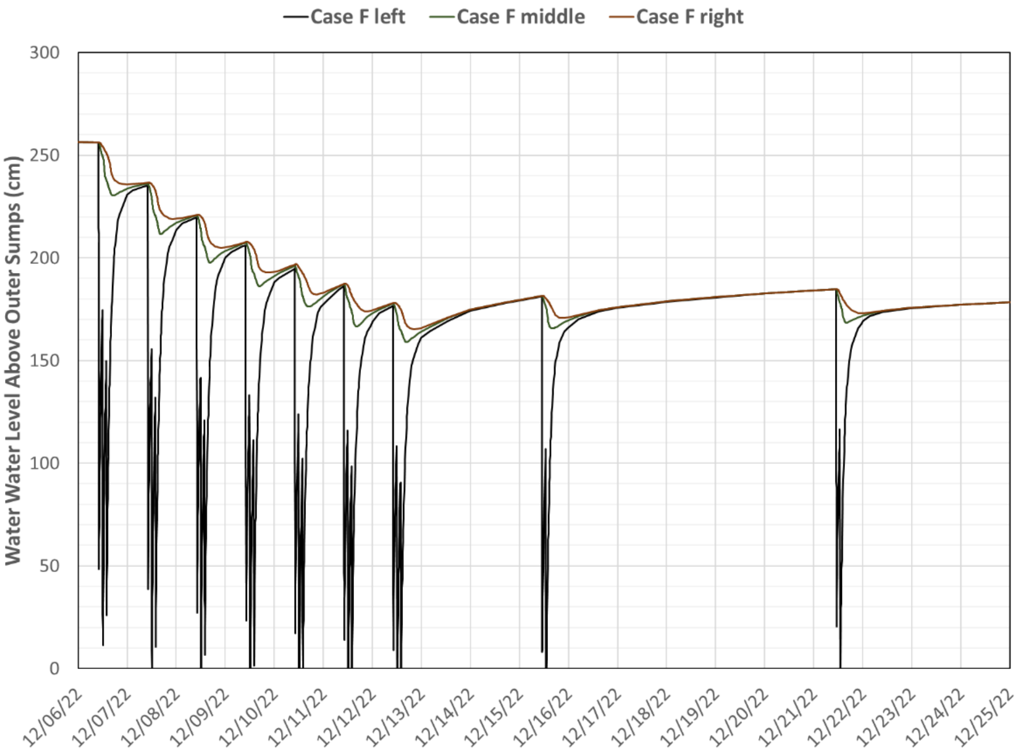

6.5 Two-layer saltstone + floor gap

For a Case G simulation, both C_0 and K_{sat} are allowed to differ between the two grout layers. Limited manual calibration produced a good fit to observations with K_{sat} = 5.0E-07 cm/s in the bottom layer and 2.0E-09 cm/s in the top layer, and C_0 = 7.0E-07 Pa^{-1} in the bottom layer and 2.0E-07 Pa^{-1} in the top layer.

Simulation results are shown in Figure 6-13. The PFLOTRAN model generally mimics the observed drawdown throughout the December 2022 to April 2023 period. One minor exception is early January 2023 where the observed drawdown is flat at around 190 cm whereas the model shows a steady decline. A potential explanation is condensation of water vapor within SDU 6 in late December 2022. Figure 6-14 illustrates vapor space temperature from mid-December through January. Vapor space temperature was around 15 °C initially and dropped to a low of 2.5 °C in late December. Assuming the relative humidity was near 100% initially, the drop in temperature would condense a significant amount of water vapor, around 175 gallons as shown in Table 6-7. If the condensate migrated to the drainwells along the interface between the wall and saltstone and across the floor-grout interface, then 18 cm would be added to the drainwells water level. Once the water is inside well casings evaporation would be limited compared to a surface pool. The additional source of liquid water may have stalled well drawdown due to ongoing leaks. Recent surveillance video suggests saltstone is not bonded to the SDU 6 wall such that flow between the grout and wall is plausible. Thermal contraction is another potential mechanism affecting water levels, but not quantitatively analyzed here.

Case G has a relatively low K_{sat} in the upper grout layer. Case H explores whether a good fit can be achieved with K_{sat} = 5.0E-10 cm/s in the upper layer, same as the 2020 SDF PA, by adjusting C_0. A parametric study was conducted with C_0 in the upper layer ranging between 2.0E-07 Pa^{-1} (Case G) and 7.0E-07 Pa^{-1} (lower layer compressibility). The best result was achieved with the latter value. Thus Case H assumes the grout is uniform at C_0 = 7.0E-07 Pa^{-1}, but K_{sat} = 5.0E-07 cm/s in the lower 0.7 meters and K_{sat} = 5.0E-10 cm/s in the upper 3.3 meters. Simulation results for Case H are shown in Figure 6-15. Goodness-of-fit for Cases G and H is about the same.

Case H seems more likely than Case G from two perspectives. First, agreement with SDU 6 data is achieved with a single, uniform, value of C_0 that lies well within the uncertainty range for C_0 based on Young's modulus measurements. Second, the hydraulic conductivity assigned to most of the grout (upper 3.3 meters) matches the 2020 SDF PA assumption, which is based on extensive data analysis. Case H is consistent with the hypotheses of SRMC-CWDA-2024-00045 in that a fast-flow path exists at the floor-grout interface and the initial grout lifts exhibit higher hydraulic conductivity due to some combination of cold joints and fissures due to drying shrinkage. For these reasons, Case H is considered the most likely configuration among the other conceptual models and/or parameter assignments considered herein.

While Case H is the strongest candidate to explain SDU 6 behavior, a firm conclusion cannot be drawn considering uncertain inputs and model biases, which include:

- Drainage (pumping) volumes
- Leakage volumes
- Leak rates

- Initial saturation state of saltstone
- Disposition of East Sump water returned to SDU 6
- Condensation/evaporation effects
- Compressibility of saltstone
- Simplifications for modeling poroelasticity
- Somewhat higher correlation between the left pumped well and the middle and right monitoring wells in model simulations (e.g. Figure 6-15) compared to field observations (Figure 6-2).

Therefore, possibilities other than Case H cannot be ruled out. Nonetheless, the conceptual modeling conducted herein supports the hypothesis of a fast-flow path at or adjoining the floor-grout interface. This study also supports the hypothesis of a higher conductivity grout layer, roughly 2 feet thickness, adjoining the fast-flow path.

Case H deviates from the PA conceptual model in two ways: a horizontal fast-flow path at the floor-grout interface equivalent to a 0.5 mm crack, and 0.7 meters of bottom grout with K_{sat} = 5.0E-07 cm/s. Case H could form the basis for a future dose sensitivity case to better understand dose consequences. Appendix A presents a Quality Assurance (QA) check on this key modeling case via a benchmarking comparison to an equivalent PORFLOW simulation.

Case I is another potential dose sensitivity case of interest. For Case I the hydraulic conductivity of the upper grout is set to 1.0E-08 cm/s, which is essentially the upper range of K_{sat} data considered in SRR-CWDA-2018-00004. Compressibility in the upper grout is treated as a calibration parameter. A good fit is achieved with C_0 = 0.8E-07 Pa^{-1} (Table 6-3). Case I is a plausible configuration but less so than Case G because of the greater disparity C_0 between the upper and lower grout layers.

Figure 6-13: Simulated drawdown for Case G.

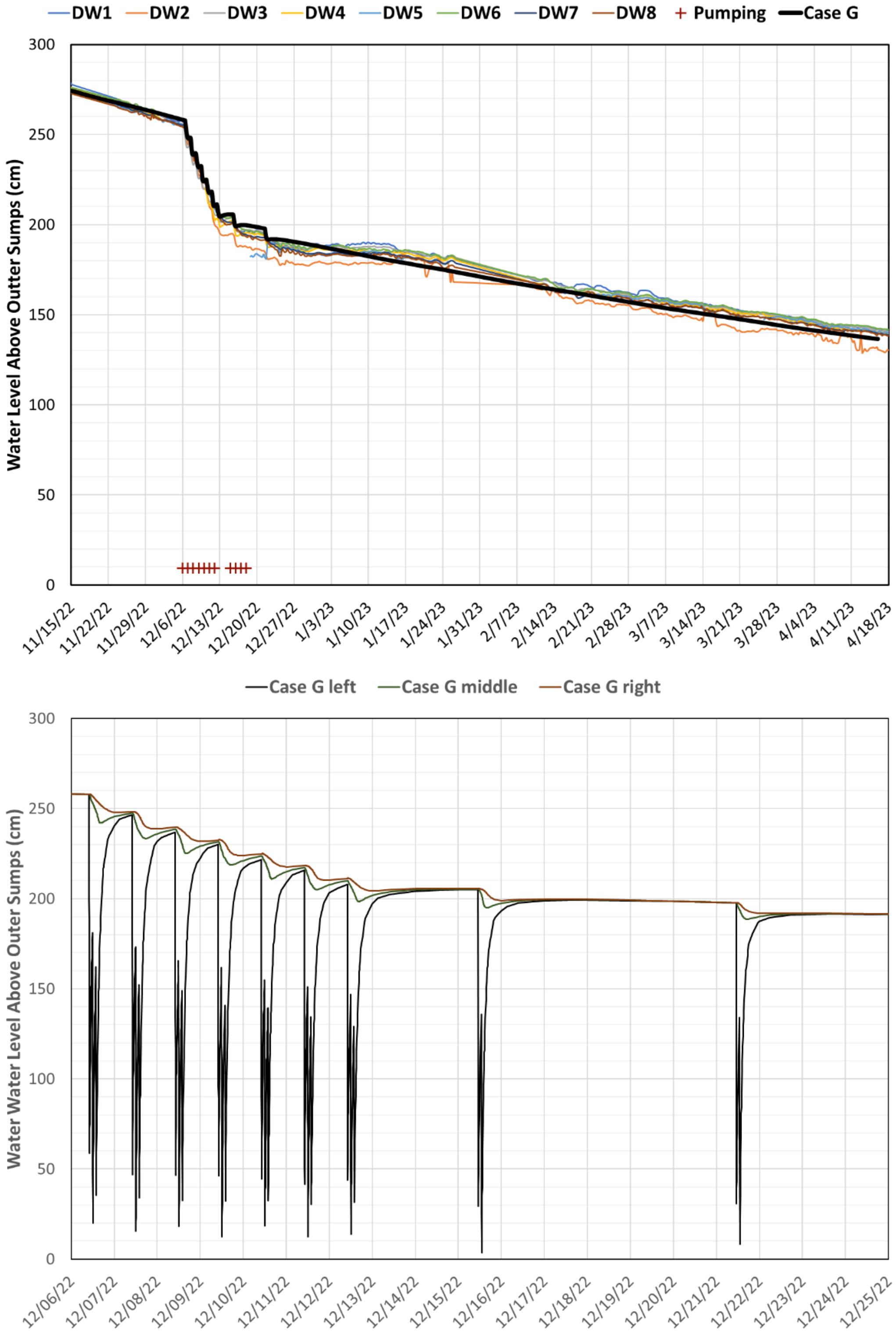

Figure 6-14: SDU 6 vapor space temperatures, 12/15/2022 to 1/31/2023.

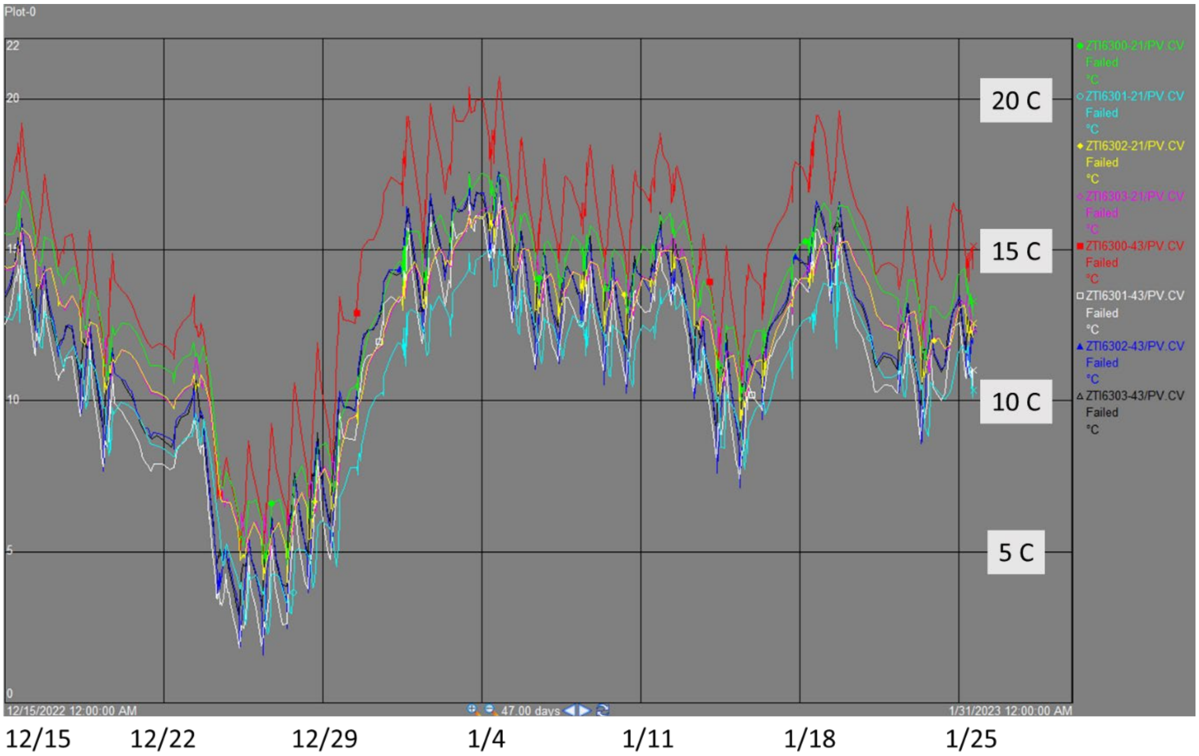

Table 6-7: Condensate potential between 12/15/2022 and 12/26/2022.

Parameter	Initial	Final	Units	Comments
Molar density of water vapor				
Date	12/15/2022	12/26/2022		
Gas constant, R	8.314		J/mol-K	
Temperature, T	15	2.5	C	
	288.15	275.65	K	
Water vapor pressure, P_v	1702.0	731.0	Pa	August-Roche-Magnus
Molar density, n/V	0.710	0.319	mol/m^3	$P_vV = nRT$
SDU 6 vapor space				
Diameter	375		ft	
	114.3		m	
Area	10261		m^2	
Roof height	43.5		ft	
Grout height	13.5		ft	
Thickness	30		ft	
	9.144		m	
Volume	9.38E+04		m^3	
Condensation potential				
Water vapor moles, n	6.67E+04	2.99E+04	mol	
Molecular weight, M_w	18		g/mol	
	0.018		kg/mol	
Water vapor mass, m	1.20E+03	5.39E+02	kg	
Density of water, ρ	998		kg/m^3	
Liquid water volume, V_w	1.202	0.540	m^3	
	318	143	gal	
Condensed water volume, ΔV_w	175		gal	
Drainwells				
Number of wells	8			
Diameter	30		in	
Total area	5655		in^2	
	24.5		gal/in	
Condensate thickness if in drainwells	7.1		in	
	18		cm	

Figure 6-15: Simulated drawdown for Case H.

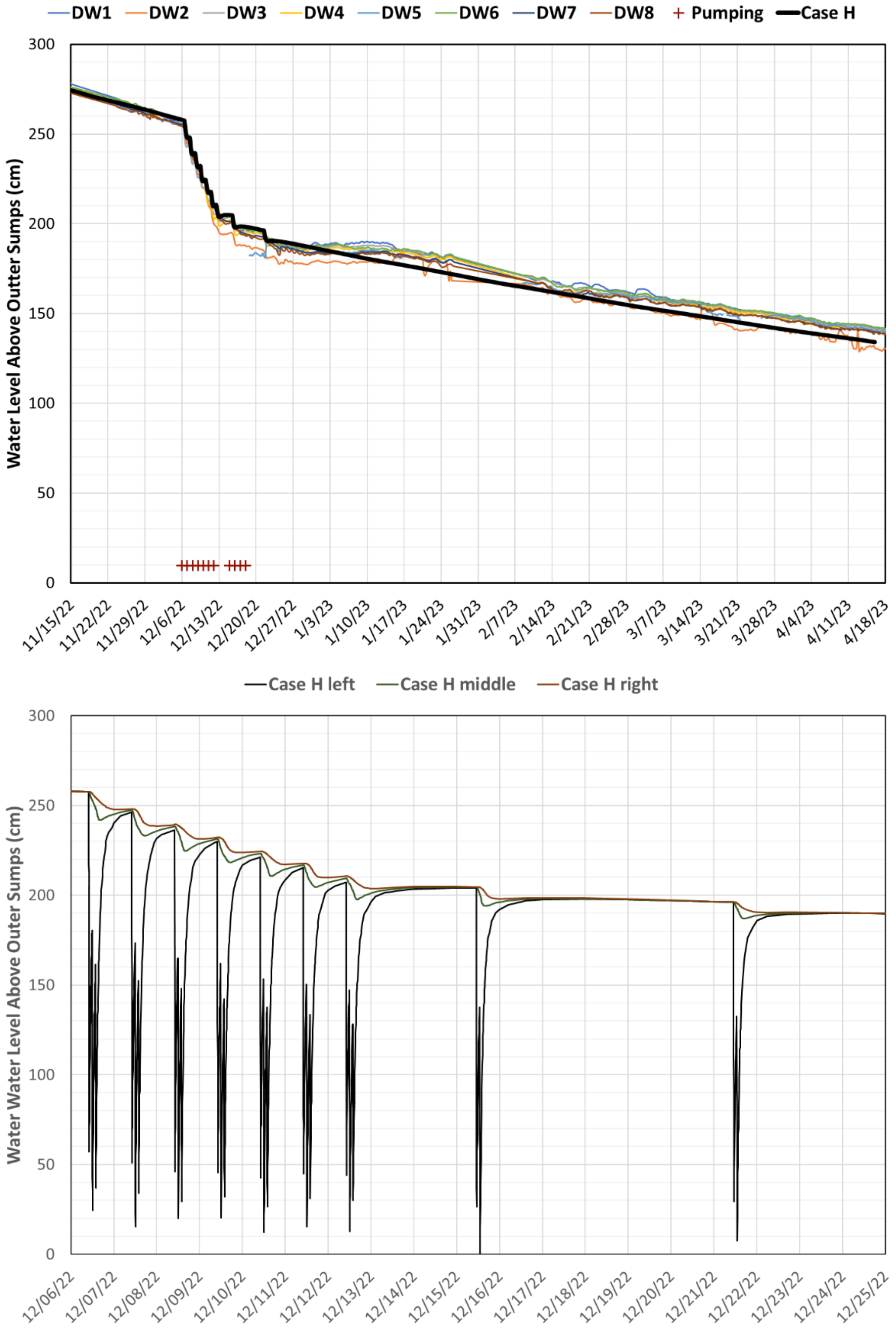

Figure 6-16: Simulated drawdown for Case I.

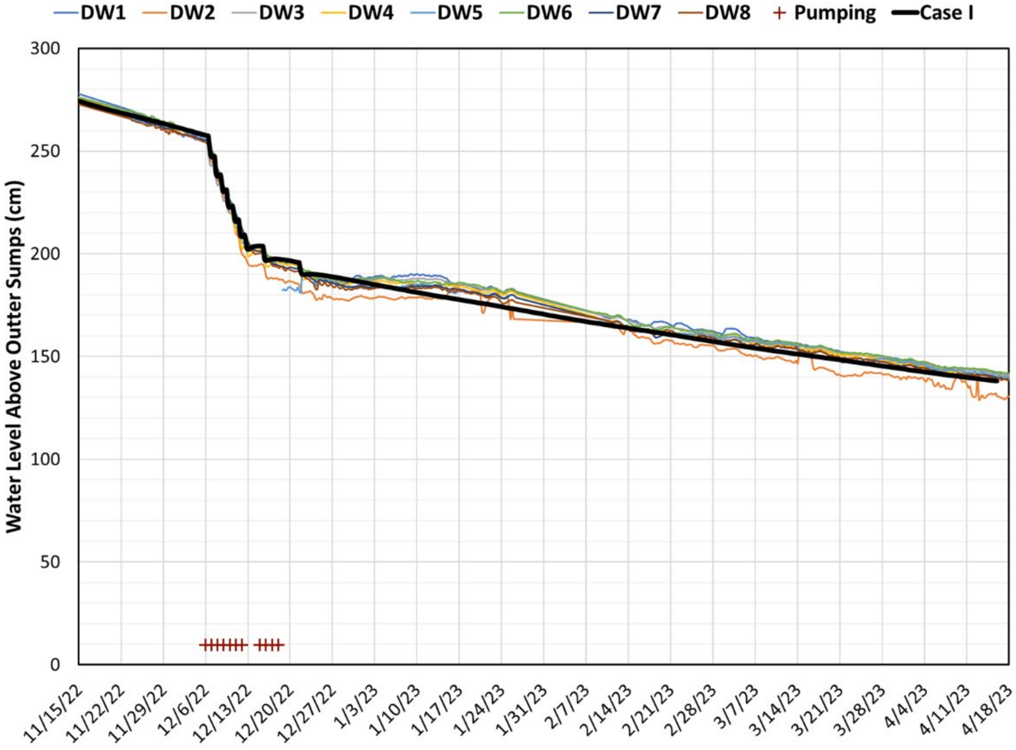

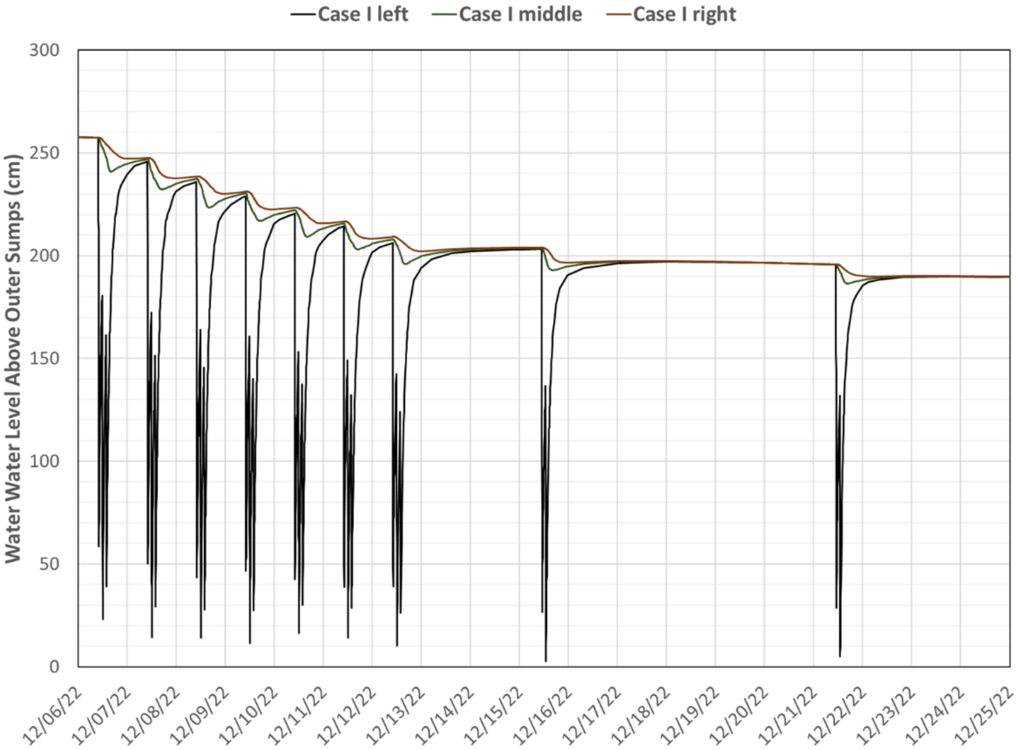

7.0 Conclusions

Conceptual model testing using analytical tools and numerical models supports the hypothesis of a fast-flow path at or adjoining the SDU 6 floor-grout interface, and an adjoining or coincident higher conductivity grout layer roughly 0.7 meters thick. The fast-flow path is inferred to be equivalent to a 0.5 mm physical gap between the floor and grout. Conductivity in the lower grout layer (bottom 0.7 m) is estimated to average 5.0E-07 cm/s, compared to 5.0E-10 cm/s assumed in the 2020 SDF PA. Hydraulic conductivity in the upper grout (3.3 m) is estimated to be consistent with SDF PA assumption of 5.0E-10 cm/s. The drainwater produced during water level drawdown likely comes from matrix compression, which squeezes water from the saltstone pores. The hypothesis of uniformly higher conductivity grout and no fast-flow path at the floor-grout interface is rejected because K_{sat} = 3.E-03 cm/s, an unreasonably high hydraulic conductivity value for saltstone given laboratory characterization data, is required to match SDU 6 drawdown data. These conclusions are tentative because of various modeling uncertainties and biases. Further study of SDU 6 and other 375-ft diameter disposal units is recommended to reduce conceptual model uncertainties.

8.0 References

de Marily, G., Quantitative Hydrogeology: Groundwater Hydrology for Engineers, Academic Press, 440 p., https://gw-project.org/books/quantitative-hydrogeology-groundwater-hydrology-for-engineers/, 1986.

Fredlund, D. G., and H. Rahardjo, Soils Mechanics for Unsaturated Soils, John Wiley, New York, 1993.

Freeze, A. and J. Cherry, Groundwater, Prentice-Hall, 604 p., https://gw-project.org/books/groundwater/, 1979.

Guarracino, L., *Estimation of saturated hydraulic conductivity* K_S *from the van Genuchten shape parameter* α, Water Resources Research, Vol. 43, (11), W11502, 2007. DOI: 10.1029/2006WR005766.

Guerriero, V., *1923–2023: One Century since Formulation of the Effective Stress Principle, the Consolidation Theory and Fluid–Porous-Solid Interaction Models*, Geotechnics 2, 961–988. 2022. https://doi.org/10.3390/geotechnics2040045

Guerriero, V. and S. Mazzoli, *Theory of Effective Stress in Soil and Rock and Implications for Fracturing Processes: A Review*. Geosciences 11, 119, 2021. https://doi.org/10.3390/geosciences11030119

Leverett, M.C., *Capillary Behavior in Porous Solids*, Transactions of the AIME, Vol. 142, No. 1, pp. 159-172, 1941.

Mualem, Y., *New Model for Predicting Hydraulic Conductivity of Unsaturated Porous-Media*, Water Resources Research, 12, 513-522, 1976.

Or, D. and M. Tuller, *Flow in unsaturated fractured porous media: Hydraulic conductivity of rough surfaces*, Water Resources Research 36, 1165-1177, 2000.

Richards, B. G., *Measurement of free energy of soil moisture by the psychrometric technique using thermistors*, in Moisture Equilibria and Moisture Changes in Soils Beneath Covered Areas: A Symposium, p. 39-46, Butterworths, Australia, 1965.

SIMCO_08-31-2012, *Final Report Comparison of Wasteform Mixtures*, SIMCO Technologies, Inc., Quebec, QC, Canada, August 2012.

SREL DOC No. R-16-0003, Seaman, J. C., F. M. Coutelot, J. Cochran, R. J. Thomas and M. R. Baker, *Contaminant Leaching from Saltstone*, Savannah River Ecology Laboratory, Aiken, SC, Rev. 0, September 2016.

SRMC-CWDA-2023-00032, Hommel, S. P., *Conceptualization of Potential Leak Paths Associated with Saltstone Disposal Unit 6 (SDU 6)*, Savannah River Site, Aiken, SC, Rev. 0, April 2023.

SRMC-CWDA-2024-00045, Simner, S. P., *Observations Related to the Inter-Connectivity of SDU 6 Drainwells*, Savannah River Site, Aiken, SC, Rev. 0, July 2024.

SRMC-CWDA-2024-00049, *Development of van Genuchten Parameters for Saltstone with Differing Initial Saturated Hydraulic Conductivities*, Savannah River Site, Aiken, SC, Rev. 0, July 2024.

SRMC-LWP-2022-00001, *Savannah River Site — Waste Tank Levels* and *Tanks By System / Function*, Savannah River Site, Aiken, SC, Rev. 83, June 2024.

SRMC-LWP-2023-00001, *Liquid Waste System Plan*, Savannah River Site, Aiken, SC, Rev. 23-P, March 2023.

SRMC-STI-2022-00601, Hunter, H., *Cement Free Grout Processing Improvements – 23516*, WM2023 Conference, February 26 – March 2, 2023, Phoenix, Arizona, USA.

SRNL-STI-2011-00665, Reigel, M. M., T. B. Edwards, and B. R. Pickenheim, *Operational and Compositional Factors that Affect the Performance Properties of ARP/MCU Saltstone Grout*, Savannah River Site, Aiken, SC, Rev. 0, February 2012.

SRNL-STI-2012-00522, Cozzi, A. D., C. A. Langton and K. M. Fox, *Evaluation of the Impact of Thin Pours on Saltstone Properties*, Savannah River National Laboratory, Aiken, SC, Rev. 0, September 2012.

SRNL-STI-2018-00077, Flach, G. P., *Degradation of Saltstone Disposal Unit Cementitious Materials*, Savannah River National Laboratory, Aiken, SC, Rev. 1, August 2018.

SRNL-STI-2019-00355, Nichols, R. L., and B. T. Butcher, *Hydraulic Properties Data Package for the E-Area Soils, Cementitious Materials, and Waste Zones – Update*, Savannah River Site, Aiken, SC, Rev. 1, May 2020.

SRR-CWDA-2018-00004, Hommel, S. P., *Recommended Values for Cementitious Degradation Modeling to Support Future SDF Modeling*, Savannah River Site, Aiken, SC, Rev. 1, August 2018.

SRR-CWDA-2019-00001, *Performance Assessment for the Saltstone Disposal Facility at the Savannah River Site*, Savannah River Site, Aiken, SC, Rev. 0, March 2020.

SRR-CWDA-2019-00003, Simner, S. P., *Cement-Free Formulation Down-Select Report*, Savannah River Site, Aiken, SC, Rev. 0, February 2019.

SRR-CWDA-2020-00008, Simner, S. P., *Cement-Free Saltstone Down-Selection Report Follow-u*, Savannah River Site, Aiken, SC, Rev. 0, February 2020.

SRR-CWDA-2020-00040, Hommel, S. P., *Recommended Modeling Inputs for Evaluating Cement Free Saltstone, Based on Down Selection Report and Other Literature*, Savannah River Site, Aiken, SC, Rev. 0, June 2020.

SRR-CWDA-2021-00034, Flach, G. P., *Chemical and Physical Evolution of Tank Closure Cementitious Materials*, Savannah River Site, Aiken, SC, Rev. 0, April 2021.

SRR-CWDA-2021-00052, Flach, G. P., *Supplemental Information and Proposed Probabilistic Inputs Related to NRC RSI-4: Saltstone Degradation*, Savannah River Site, Aiken, SC, Rev. 0, July 2021.

SRR-CWDA-2020-00066, Flach, G. P., *Normative Mineral Compositions of Saltstone Disposal Facility Cementitious Materials*, Savannah River Site, Aiken, SC, Rev. 0, September 2020.

SRR-SPT-2013-00044, Simner, S. P., *Update of Fiscal Year 2013 Activities Related to SDU Sampling and Analysis*, Savannah River Site, Aiken, SC, Rev. 0, September 2013.

USGS Open File Report 02-197, Halford K. J. and E. L. Kuniansky, *Documentation of Spreadsheets for the Analysis of Aquifer-Test and Slug-Test Data*, U. S. Geological Survey, Carson City, Nevada, 2002. https://pubs.usgs.gov/of/2002/ofr02197/

van Genuchten, M.T., *A Closed-Form Equation for Predicting the Hydraulic Conductivity of Unsaturated Soils*, Soil Science America Journal, Vol. 44, No. 5, pp. 892-898, 1980. DOI: 10.2136/sssaj1980.03615995004400050002x.

Wang, J. S. Y., and T. N. Narasimhan, *Hydrologic Mechanisms Governing Fluid Flow in a Partially Saturated, Fractured, Porous Medium*, Water Resour. Res., 21(12), 1861–1874, doi:10.1029/WR021i012p01861, 1985.

WSRC-TR-2006-00067, Harbour, J. R., E. K. Hansen, T. B. Edwards, V. J. Williams, R. E. Eibling, D. R. Best and D. M. Missimer, *Characterization of Slag, Fly Ash and Portland Cement for Saltstone*, Savannah River Site, Aiken, SC, Rev. 0, February 2006.

WSRC-TR-2007-00437, Harbour, J. R., T. B. Edwards, V. J. Williams, G. W. Scherer, and D. M. Feliciano, *Permeability of Saltstone – Measurement By Beam Bending*, Savannah River Site, Aiken, SC, Rev. 0, October 2007.

Appendix A - Independent Verification of PFLOTRAN Simulation Case H via PORFLOW Benchmark

Figure A-1 reproduces the SDU 6 drawdown behavior shown in Figure 6-2, which is investigated in the main body of this report using PFLOTRAN model simulations and analytic tools. The key PFLOTRAN simulation is "Case H" shown in Figure A-2 (Figure 6-15).

Figure A-1. SDU 6 drainwell observations for December 6-25, 2022.

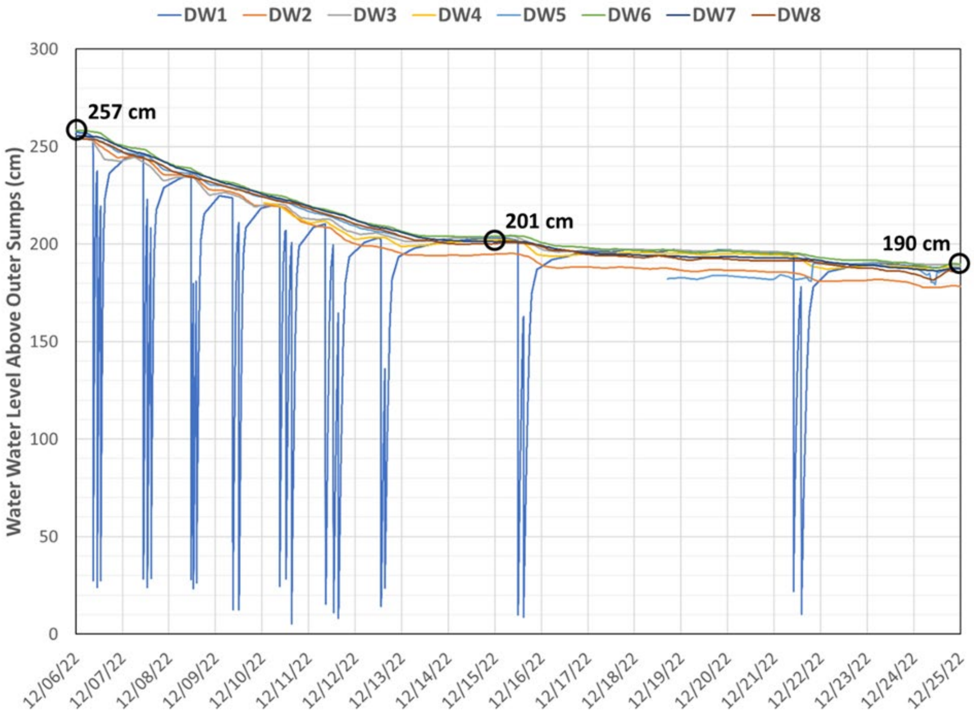

Figure A-2. PFLOTRAN Case H simulation for December 6-25, 2022.

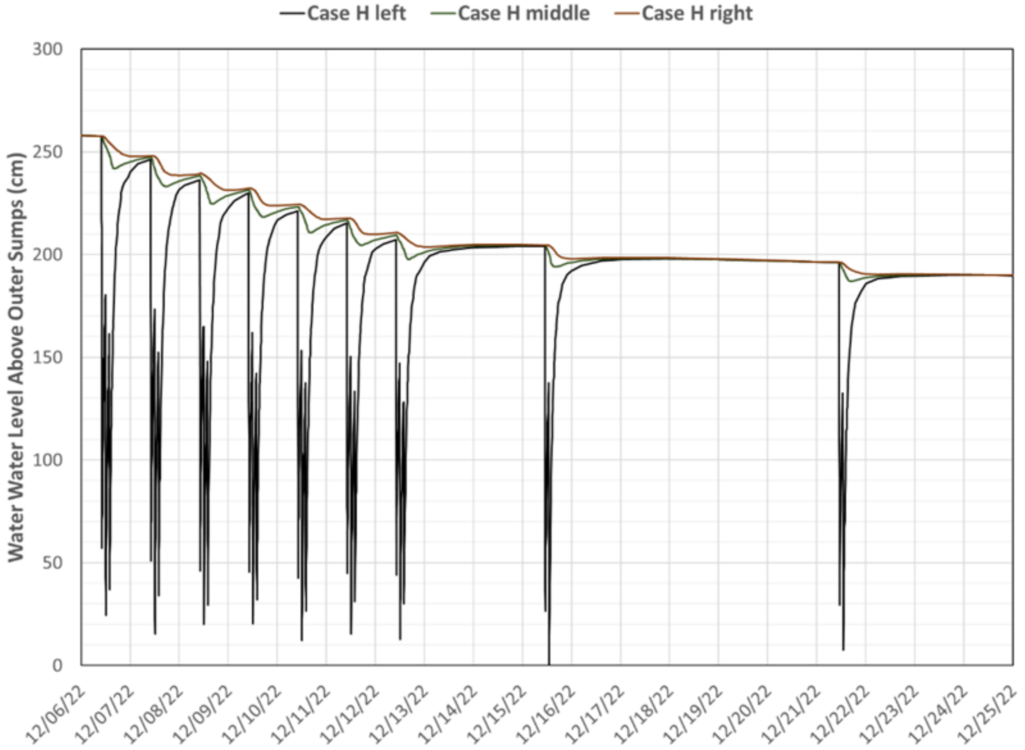

To verify the PFLOTRAN model underlying these results, an equivalent PORFLOW model of Case H was developed for a benchmarking comparison. For computational efficiency and more robust convergence behavior, a coarser grid was selected for PORFLOW simulations: 27 x 27 x 15 elements (Figure A-3). The dimensions of the material zones and wells are the same as those in the PFLOTRAN grid.

Figure A-3. PORFLOW grid.

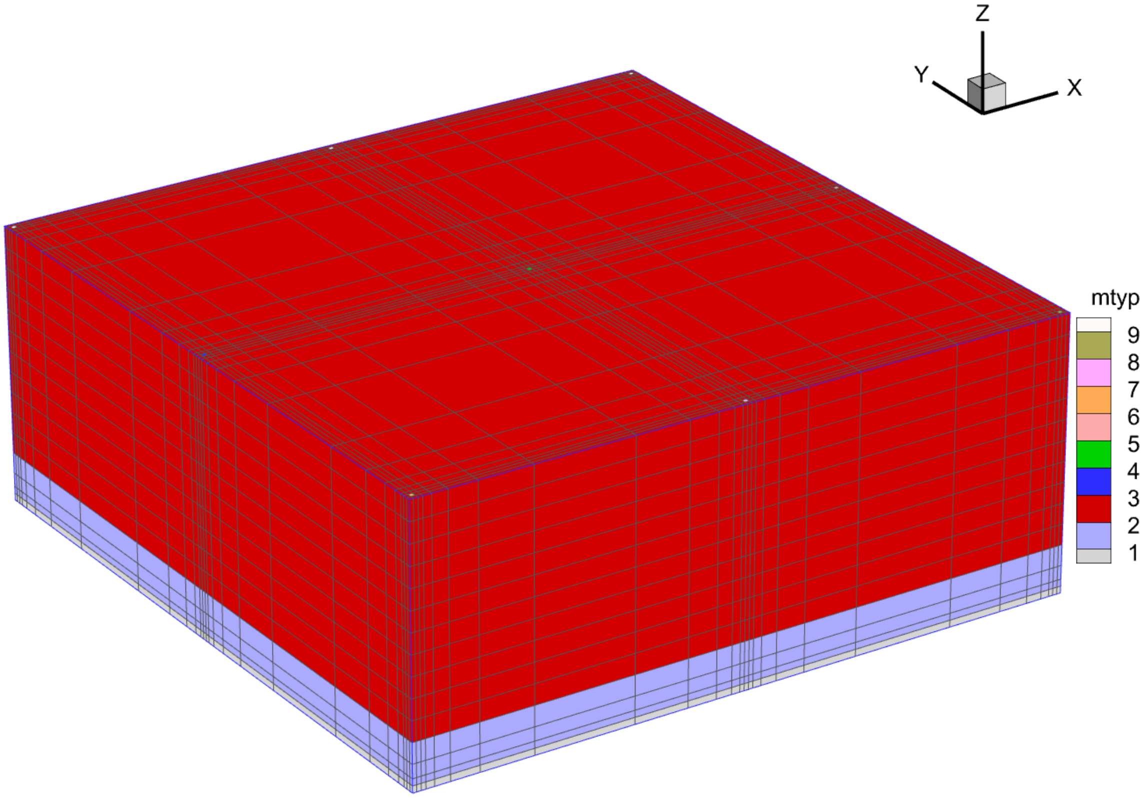

PORFLOW expresses porous-medium compressibility in terms of a *specific storage coefficient*, S_s, whereas PFLOTRAN uses a *porosity compressibility constant*, C_0. From Equation (55), these input parameters are related through the expression

$$S_s = \rho g n C_0$$

The PFLOTRAN Case H simulation assumes C_0 = 7.0E-07 Pa^{-1} for grout, which is equivalent to S_s = 4.5E-05 cm^{-1}. An initial PORFLOW simulation with the same grout inputs as PFLOTRAN Case H under-predicted drawdown in the December 6-25, 2022 period. Specific storage coefficient was subsequently reduced 22% to S_s = 3.5E-05 cm^{-1} to better match the observations depicted in Figure 6-1. The calibrated PORFLOW results are shown in Figure A-4 and resemble the PFLOTRAN drawdowns in Figure A-2, albeit with a lower assumed grout compressibility.

Considering differences in grid resolution and numerical algorithms, this level of agreement is considered acceptable verification of the PFLOTRAN Case H results.

Figure A-4. PORFLOW simulation of December 6-25, 2022 period.